



## AI-based monitoring of retinal fluid in disease activity and under therapy



Ursula Schmidt-Erfurth<sup>a,\*</sup>, Gregor S. Reiter<sup>a,1</sup>, Sophie Riedl<sup>a,1</sup>, Philipp Seeböck<sup>a,1</sup>, Wolf-Dieter Vogl<sup>a,1</sup>, Barbara A. Blodi<sup>b,1</sup>, Amitha Domalpally<sup>b,1</sup>, Amani Fawzi<sup>c,1</sup>, Yali Jia<sup>d,1</sup>, David Sarraf<sup>e,1</sup>, Hrvoje Bogunovic<sup>a,1</sup>

<sup>a</sup> Department of Ophthalmology Medical University of Vienna, Spitalgasse 23, 1090, Vienna, Austria

<sup>b</sup> Fundus Photograph Reading Center, Department of Ophthalmology and Visual Sciences, University of Wisconsin, Madison, WI, USA

<sup>c</sup> Feinberg School of Medicine, Northwestern University, Chicago, IL, USA

<sup>d</sup> Ophthalmology, Casey Eye Institute, Oregon Health & Science University, Portland, OR, USA

<sup>e</sup> Stein Eye Institute, University of California Los Angeles, Los Angeles, CA, USA

### ARTICLE INFO

#### Keywords:

Optical coherence tomography (OCT)  
Deep learning (DL)  
Intraretinal fluid (IRF)  
Subretinal fluid (SRF)  
Fluid/function correlation  
Automated algorithms

### ABSTRACT

Retinal fluid as the major biomarker in exudative macular disease is accurately visualized by high-resolution three-dimensional optical coherence tomography (OCT), which is used world-wide as a diagnostic gold standard largely replacing clinical examination. Artificial intelligence (AI) with its capability to objectively identify, localize and quantify fluid introduces fully automated tools into OCT imaging for personalized disease management. Deep learning performance has already proven superior to human experts, including physicians and certified readers, in terms of accuracy and speed. Reproducible measurement of retinal fluid relies on precise AI-based segmentation methods that assign a label to each OCT voxel denoting its fluid type such as intraretinal fluid (IRF) and subretinal fluid (SRF) or pigment epithelial detachment (PED) and its location within the central 1-, 3- and 6-mm macular area. Such reliable analysis is most relevant to reflect differences in pathophysiological mechanisms and impacts on retinal function, and the dynamics of fluid resolution during therapy with different regimens and substances. Yet, an in-depth understanding of the mode of action of supervised and unsupervised learning, the functionality of a convolutional neural net (CNN) and various network architectures is needed. Greater insight regarding adequate methods for performance, validation assessment, and device- and scanning-pattern-dependent variations is necessary to empower ophthalmologists to become qualified AI users. Fluid/function correlation can lead to a better definition of valid fluid variables relevant for optimal outcomes on an individual and a population level. AI-based fluid analysis opens the way for precision medicine in real-world practice of the leading retinal diseases of modern times.

Macular disease with its detrimental consequence of severe and irreversible visual loss dominates clinical care and medical research to the same extent as life-threatening diseases such as cancer and cardiovascular disease. Its medical and socioeconomic impact is immense. This becomes evident when one considers people older than 65 years of age are at a high risk for developing age-related macular degeneration (AMD) (He et al., 2016): More than 600 million were in this age group in 2015 and the elderly population is expected to grow by 236 million over

the next 10 years. This trend coincides with a global pandemic in diabetes mellitus, which currently affects about 420 million adults. The World Health Organisation predicts an increase to more than 800 million by 2030, of whom a third will experience vision-threatening disease (Lee et al., 2015; World Health Organisation, 2016). In addition, ophthalmologists and eye care professionals have been alarmed by the world-wide increase of 23% for blindness and 24% for severe vision loss between 2005 and 2015, in total affecting 900 million individuals

\* Corresponding author.

E-mail addresses: [ursula.schmidt-erfurth@meduniwien.ac.at](mailto:ursula.schmidt-erfurth@meduniwien.ac.at) (U. Schmidt-Erfurth), [gregor.reiter@meduniwien.ac.at](mailto:gregor.reiter@meduniwien.ac.at) (G.S. Reiter), [sophie.riedl@meduniwien.ac.at](mailto:sophie.riedl@meduniwien.ac.at) (S. Riedl), [philipp.seeboeck@meduniwien.ac.at](mailto:philipp.seeboeck@meduniwien.ac.at) (P. Seeböck), [wolf-dieter.vogl@meduniwien.ac.at](mailto:wolf-dieter.vogl@meduniwien.ac.at) (W.-D. Vogl), [bablodi@wisc.edu](mailto:bablodi@wisc.edu) (B.A. Blodi), [adomalpally@rc.ophth.wisc.edu](mailto:adomalpally@rc.ophth.wisc.edu) (A. Domalpally), [amani.fawzi@northwestern.edu](mailto:amani.fawzi@northwestern.edu) (A. Fawzi), [jiaya@ohsu.edu](mailto:jiaya@ohsu.edu) (Y. Jia), [dsarraf@ucla.edu](mailto:dsarraf@ucla.edu) (D. Sarraf), [hrvoje.bogunovic@meduniwien.ac.at](mailto:hrvoje.bogunovic@meduniwien.ac.at) (H. Bogunovic).

<sup>1</sup> Percentage of work contributed by each author in the production of the manuscript is as follows: Ursula Schmidt-Erfurth 20%, Gregor S. Reiter 10%, Sophie Riedl 10%, Philipp Seeböck 7,5%, Wolf-Dieter Vogl 7,5%, Barbara Blodi 5%, Amitha Domalpally 5%, Amani Fawzi 5%, Yali Jia 5%, David Sarraf 5%, Hrvoje Bogunovic 20%.

<https://doi.org/10.1016/j.preteyeres.2021.100972>

Received 22 February 2021; Received in revised form 11 May 2021; Accepted 13 May 2021

Available online 22 June 2021

1350-9462/© 2021 The Authors.

Published by Elsevier Ltd.

This is an open access article under the CC BY-NC-ND license

(<http://creativecommons.org/licenses/by-nd/4.0/>).

| <b>Abbreviations</b> |  |
|----------------------|--|
| AAO                  | American Academy of Ophthalmology            |
| AI                   | artificial intelligence                      |
| AMD                  | age-related macular degeneration             |
| ANOVA                | analysis of variance                         |
| AO                   | adaptive optics                              |
| ASRS                 | The American Society of Retina Specialists   |
| AUC                  | area under the curve                         |
| AUPR                 | area under the precision-recall curve        |
| AUROC                | area under receiver operating characteristic |
| BCVA                 | best-corrected visual acuity                 |
| BM                   | Bruch's membrane                             |
| BRB                  | blood retinal barrier                        |
| BRVO                 | branch retinal vein occlusion                |
| CNN                  | convolutional neural network                 |
| CNV                  | choroidal neovascularization                 |
| CP                   | center point                                 |
| CPT                  | center point thickness                       |
| CRT                  | central retinal thickness                    |
| CSC                  | central serous chorioretinopathy             |
| CST                  | central subfield thickness                   |
| DFE                  | dilated fundus examination                   |
| DME                  | diabetic macular edema                       |
| dPED                 | drusenoid pigment epithelial detachment      |
| DR                   | diabetic retinopathy                         |
| DRCR                 | Diabetic Retinopathy Clinical Research       |
| DRIL                 | disorganization of retinal inner layers      |
| DSC                  | Dice similarity coefficient                  |
| EMR                  | electronic medical record                    |
| ETDRS                | Early Treatment Diabetic Retinopathy Study   |
| FA                   | fluorescein                                  |
| FCNN                 | entirely convolutional neural networks       |
| FCPT                 | foveal center point thickness                |
| FN                   | false negatives                              |
| FP                   | false positive                               |
| FPRC                 | Fundus Photograph Reading Center             |
| fPED                 | fibrovascular pigment epithelial detachment  |
| GA                   | geographic atrophy                           |
| GAN                  | generative adversarial networks              |
| HRF                  | hyperreflective foci                         |
| ILM                  | internal limiting membrane                   |
| INL                  | inner nuclear layer                          |
| IRC                  | intraretinal cyst                            |
| IRF                  | intraretinal fluid                           |
| LMM                  | linear mixed models                          |
| LoA                  | limits of agreement                          |
| MMP                  | matrix metalloproteinase                     |
| MNV                  | macular neovascularization                   |
| MP                   | microperimetry                               |
| nAMD                 | neovascular AMD                              |
| NPA                  | non-perfusion areas                          |
| NSR                  | neurosensory retina                          |
| OCT                  | optical coherence tomography                 |
| OCTA                 | OCT angiography                              |
| ONL                  | outer nuclear layer                          |
| OPL                  | outer plexiform layer                        |
| PCV                  | polypoidal choroidal vasculopathy            |
| PED                  | pigment epithelial detachment                |
| PRN                  | pro-re-nata                                  |
| RCT                  | randomized clinical trial                    |
| ROC                  | receiver operating characteristic            |
| RPE                  | retinal pigment epithelium                   |
| RVO                  | retinal vein occlusion                       |
| SD                   | standard deviation                           |
| SD-OCT               | spectral-domain OCT                          |
| SF                   | subretinal fibrosis                          |
| SHRM                 | subretinal hyperreflective material          |
| sPED                 | serous pigment epithelial detachment         |
| SRF                  | subretinal fluid                             |
| T&E                  | treat-and-extend                             |
| TD                   | time domain                                  |
| TD-OCT               | time-domain OCT                              |
| TP                   | true positive                                |
| VA                   | visual acuity                                |
| VEGF                 | vascular endothelial growth factor           |
| VIBES                | Vienna Imaging Biomarker Eye Study           |

(Vos et al., 2016), in spite of significant advances in diagnostic and therapeutic tools. Medicare payments per beneficiary for the care of patients with AMD in one cohort doubled from \$1504 in 1994 to \$3263 in 2006, mostly due to anti-VEGF injections (Day et al., 2011), a development which has meanwhile led to one of the biggest demands on budgets in medicine.

## 1. Current knowledge on the role of fluid

### 1.1. Learnings about the role of fluid in the pivotal trials

Two unparalleled success stories in medicine have revolutionized the management of macular disorders world-wide. Firstly, non-invasive high-resolution retinal imaging by optical coherence tomography (OCT) became a most efficient diagnostic device. Secondly, intravitreal anti-vascular endothelial growth factor (VEGF) substances have successfully inhibited disease activity in the three leading macular diseases: Neovascular AMD (nAMD), diabetic macular edema (DME) and retinal vein occlusion (RVO). However, while highly successful clinical trial results heralded a paradigm shift, the outcomes in medical practice have been poor (Mehta et al., 2018). The explanation for the mismatch is not failing therapeutic interventions per se: High-dose application of VEGF inhibitors such as ranibizumab and aflibercept, to name the approved

and widely used block-buster agents, has excellent functional and morphological benefits, inducing rapid and sustained resolution of pathological macular fluid in numerous prospective clinical trials.

In the pivotal ANCHOR and MARINA trials, patients gained an average of +7–10 letters and more than a third improved by at least +3 lines following a fixed administration of ranibizumab to reduce macular edema (Brown et al., 2009; Rosenfeld et al., 2006). Consistent use of aflibercept led to visual gains between +7 and +11 letters in patients with active nAMD (Heier et al., 2012). Visual improvement was mirrored by a decrease in pathological retinal thickening, as rapid and maintained as the best-corrected visual acuity (BCVA) course. Sustained monthly applications of VEGF inhibitors at the highest dose led to the best BCVA outcomes, which were also stable. Yet, when intervals were extended to a bimonthly regimen, fluctuations in central retinal thickness (CRT) and a more unstable and less homogenous BCVA curve was noted (Heier et al., 2012). The loss in functional and morphological control became even more obvious when during weeks 52 through 96 in the VIEW studies patients were switched from their original dosing assignment to an as-needed regimen, i.e., extended intervals with defined retreatment criteria and mandatory dosing at least every 12 weeks (Schmidt-Erfurth et al., 2014b). Despite an overall equal efficacy in the mean values, fluctuations in macular fluids during this second year of variable intervention led to “small losses at 96 weeks in the

visual and anatomic gains seen at 52 weeks in all arms in the range of losses commonly observed with variable dosing". Proof-of-principle that an adequate adjustment of fluid control is an essential requirement for optimizing visual benefit was thereby provided in a prospective and standardized setting. Even if average values throughout the entire study cohort appeared unchanged, it became clear that individual gains and losses could not be guided easily with rough criteria used for flexible therapeutic monitoring.

Subsequent prospective trials added further evidence supporting the concept of a maximum therapeutic response with minimum intervention: In CATT, a multicenter, single-blind, non-inferiority trial, 1208 patients with nAMD were randomly assigned to receive intravitreal injections of ranibizumab or bevacizumab on either a monthly schedule or as needed with monthly evaluation. While bevacizumab and ranibizumab administered monthly were equivalent and ranibizumab as needed was equivalent to monthly ranibizumab, the result of the comparison between bevacizumab as needed and monthly bevacizumab was labeled "inconclusive". Accordingly, the mean decrease in CRT was greater in the ranibizumab-monthly group than in the other groups, again highlighting the impact of fluid and function, and the varying efficiencies of different substances (Martin et al., 2011). Rosenfeld, who was one of the investigators in PRONTO, the pioneering trial that introduced the principle of OCT-guided anti-VEGF therapy, amended the retreatment criteria during the second year of the trial to include enhanced retreatment if any qualitative increase in fluid was detected using OCT. At month 24, the mean visual acuity (VA) improved by +11.1 letters and the CRT decreased by 212 µm. VA improved by +15 letters or more in 43% of patients, a convincing argument in favor of a tight fluid-guided therapy (Lalwani et al., 2009). Rosenfeld concluded in his comprehensive review on OCT in anti-angiogenic therapy in 2016, following his extensive experience with OCT monitoring, that OCT imaging was adopted by the community "as a VEGF-meter" that allowed excess VEGF to be detected. Further that OCT had evolved to the gold standard for diagnosing nAMD, assessing treatment response and deciding on retreatment. Nevertheless, the vision that OCT was able to "quantify" macular fluid, and "identify intraretinal fluid (IRF), subretinal fluid (SRF), and fluid under the retinal pigment epithelium (RPE)" has not come to fruition clinically. Yet, the goal of such precision monitoring has been clear: To empower clinicians to be able to compare the efficiency of anti-VEGF drugs and move from fixed-dosing regimens to patient-specific dosing strategies by "observing the qualitative and quantitative changes in macular fluid" (Rosenfeld, 2016). AI methods made their powerful entry into medical diagnosis in the same year as Rosenfeld's review was published and soon expanded into the retinal sphere (Obermeyer and Emanuel, 2016).

The European guidelines for the management of nAMD were based on the pivotal trials mentioned above and similar confirmative studies. Therefore, monitoring fluid by OCT was recommended as the state-of-the-art procedure in disease management early on (Schmidt-Erfurth et al., 2014a). Subsequently, consistent correlations between fluid and function were established for the management of DME, although with less rapid fluctuations in both due to the slower progression and less reactive recurrence pattern (Schmidt-Erfurth et al., 2017a).

Standardized clinical trials with extended follow-ups also importantly revealed that complete fluid removal is not a readily accessible goal. In CATT, less than half of the patients treated monthly over one and two years still had fluid at the last visit (Martin et al., 2012). Complete fluid resolution rates were nevertheless significantly higher for ranibizumab (45.5% of patients) than for bevacizumab (only 13.9%). Similarly, in the IVAN trial, continuous treatment led to more decrease in retinal fluid. Despite the investigators' judgement that the comparison was inconclusive, bevacizumab therapy was associated with more persistent fluid and lower BCVA with -2.0 letters (Chakravarthy et al., 2012). Averaging and qualitative observations did not, however, establish a robust correlation between fluid resolution and BCVA change, as long as a precise individualized quantification was

inaccessible.

As much as undertreatment is an important challenge in real-world practice, overtreatment can be a cause for concern in clinical trials. Further injections seem unreasonable if even the most potent substances and most intensive regimen cannot resolve pathological fluid entirely. At least as long as the persistent amount and type of fluid is properly recognized, which requires an accurate fluid quantification in its entire volume, and not a mere B-scan profile as measured with CRT. It seems fair to say that the community no longer pursues a dry retina, as was the aim of most clinical trial designs in anti-VEGF therapy (Sharma et al., 2020). Regarding a regular fluctuation of fluid, referred to as *fluctuations*, was first neglected in the early aflibercept studies, where they were considered irrelevant for BCVA. However, fluid recurrences are the vital sign of disease activity and promote destructive changes at the neurosensory layers, such as macular atrophy or fibrosis (Evans et al., 2020). Foveal center point thickness (FCPT) measures of 1165 eyes from the CATT and 566 from the IVAN trial data were extracted and grouped in a combined analysis by FCPT standard deviation (SD)-based quartile. Over the 2-year follow-up, the rate of fibrosis increased correlating with an enormous increase in the rate of FCPT fluctuations, from 7.8% to 58.7%. A similar trend was found for the development of geographic atrophy (GA), rising from 9.0% to 30.2% at year 2 (Guymer, 2020). While fluid is mostly reversible, atrophy and fibrosis are the key features of irreversible visual loss (Daniel et al., 2019).

If the severity of fluid fluctuation plays such a crucial role in the development of these end-stage complications, fluid volumes have to be measured with precision, to objectively quantify variations in each individual patient and fine-tune treatment accordingly. A binary fluid determination based solely on presence or absence is not enough for personalized precision medicine in a tissue as unforgiving as the macular retina.

## 1.2. The real-world management of macular disease and its dilemma

Consistent analyses of real-world outcomes have demonstrated substantially inferior benefits for patients treated for nAMD, and to a lesser extent DME and RVO, when therapy was performed in a routine clinical setting. The LUMINOUS registry provided an extensive overview of real-world conditions for ranibizumab therapy for the three major exudative macular pathologies and consistently highlighted the importance of fluid control by an adequate frequency and timing of intervention. When 6241 patients with treatment-naïve nAMD were followed for 5 years of ranibizumab therapy, retreatment frequencies administered by clinicians with qualitative discretion of fluid dynamics were tightly associated with large therapeutic gains. Injection frequencies of <3, 3 to 6, and >6 corresponded to visual acuity gains of +1.6, +3.3, and +3.7 letters (Holz et al., 2020). Intensive fluid extravasation in RVO makes this group of disorders even more prone to fluid-related morphological alteration. Accordingly, in a total of 1366 patients with branch retinal vein occlusion (BRVO), visual gains were substantially higher in patients receiving 6–9 injections (+13.6 letters) than in those receiving only 1 injection (+3.6 letters) (Pearce et al., 2020). Out of 20 real-world studies reviewed by Chong, the mean letter gain was +2.9, and the weighted mean + 1.95, while in 12 studies the mean percentage of patients losing ≤15 letters was as high as 89%, probably due to recurrent fluid (Chong, 2016). British investigators concluded from 26 studies (n = 25,761 eyes) that although UK real-world outcomes had improved with advanced service delivery and the adoption of more proactive treatment regimens over the preceding decade, these improvements were still not as impressive as the outcomes from registration trials (Mehta et al., 2020a). The SIERRA trial was a retrospective, multi-center, real-world evidence study that included a total of 98,821 eyes from 79,885 patients receiving intravitreal anti-VEGF therapy for nAMD during a 4-year follow-up. While the VA declined with a lower injection frequency due to uncontrolled fluid recurrence, the proportion of eyes with improved VA increased in those patients treated more

frequently than the recommended q8w interval. At one year, the therapeutic improvement was +1.1 letters, and at 2 years a mean decrease of -1.3 letters was reported (Khanani et al., 2020).

The largest data base from real-world studies originates from the United States Electronic Health Records database and is comprised of functional and morphological outcomes from 30,106 patients with nAMD (Kiss et al., 2020). Analyses demonstrated that in nAMD it is not only the number of visits and interventions that matters, but also adequate timing of fluid resolution. Over the first 12 months, real-world patients afforded a mean of 8.1 practice visits, received a mean of 6.0 anti-VEGF injections, and underwent 7.2 OCT and 5.3 FA examinations per study eye. Hence, the focus on detecting fluid and leakage activity was strong and visits were tightly scheduled. Yet, during the first year of the most extensive care, mean CRT decreased only by a mean of -48 µm, and mean VA increased by just +0.6 letters BCVA. Patients receiving at least seven treatments gained on average +2 letters, and those receiving less than seven treatments lost -1 letter (Hsu and Regillo, 2020). Weighing function versus fluid, the investigators found that each treatment yielded a +0.37 letter benefit and modest improvements correlated with a modest CRT decrease of -48 µm at 12 months. They compared these results with the performance of physicians in clinical trials, and found physicians achieved a mean gain of +6 to 11 letters and a decrease in CRT of -116 to 179 µm using identical diagnostic and therapeutic hardware tools. To explain the discrepancy, they suggested that "treating physicians may be the root cause" of these real-world suboptimal outcomes due to a "sometimes too relaxed" approach to retreatment protocols. As the mechanism of anti-VEGF therapy is crucially aligned with elimination of macular fluid, failure to achieve optimal outcomes is likely due to inadequate fluid diagnosis and elimination. Obviously, the large series of high-resolution B-scans generated at every OCT visit cannot be exploited efficiently enough by the practitioner in a real-world setting, in the absence of protocols, reading center analysis and sufficient practice time for in-depth image evaluation.

Interestingly, a recent real-world analysis of electronic medical record (EMR) data collected from 1190 patients with nAMD at two sites in the United Kingdom performed as a retrospective, non-randomized cohort study, focused on the association between OCT markers of lesion activity and changes in visual acuity (Chakravarthy et al., 2020). In this analysis, qualitative absence of IRF or SRF at ≥ 2 visits resulted in a gain of +5 letters, compared with only 2 letters gained in eyes with <2 visits with absence of IRF ( $p = 0.006$ ) or SRF ( $p = 0.042$ ). Comparing treatment visits with non-treatment visits, the maximum differences in frequency of OCT markers of fluid activity were found for intraretinal fluid (IRF; 24% versus 5%) and subretinal fluid (SRF; 32% versus 5%), while pigment epithelial detachment (PED) was reported in 58% of treatment visits compared with 36% in non-treatment visits. The authors concluded that retreatment decisions are most strongly influenced by the presence of IRF and SRF and less by the presence of PED or VA loss. The definitions of IRF, SRF and PED were purely based on the practice spectrum of physicians' discretion extracted from the Medisoft EMRs. Accordingly, outcomes were again substantially below those achieved in standardized clinical trials. A more detailed assessment of this analysis revealed that IRF and SRF accounted for an injection decision in only 24% and 32% of eyes, respectively, despite the fact that IRF/SRF was at least four-fold more likely to be noted when the decision was made. Yet, no pattern of clear-cut fluid evaluation was identified. Apart from fluid presence, clinicians relied strongly on patients' loss of vision when deciding on disease management. Between the two, the influence of fluid in the decision was unclear. BCVA loss compared with the best recorded BCVA was also overestimated in real-world practice. On the positive side, in current times of advanced anti-VEGF therapy, modern physicians have become aware of the important role of fluid compartments, i.e., IRF, SRF and PED, through clinical studies and real-world registries, and try to do their best to evaluate OCT image datasets so as to make optimal treatment decisions. The precautions in patient care

during the COVID pandemic in particular have substantially changed practice patterns in anti-VEGF therapy in this direction. According to the 2020 global survey of the American Society of Retina Specialists (ASRS), 46.7% of ophthalmologists prefer to examine their patients clinically together with an OCT examination, while 39.6% make their treatment decision solely based on OCT imaging omitting clinical examination, a potential risk considering the variability in OCT-based decision making practices (American Society of Retina Specialists, 2020). A comparison of human experts and an AI-based method to identify retinal disease and therapeutic need revealed that clinicians not only have a significantly higher failure rate based on OCT evidence alone, but diagnostic precision also benefits greatly from the insight gained from fundus examination and evaluation of the clinical notes (De Fauw et al., 2018). The magnitude of therapeutic controversy is also reflected in the management of SRF. In a treat-and-extend (T&E) regimen, 47.7% of physicians tolerated SRF and maintained the extended retreatment interval, while the other half, i.e., 47.3%, did not tolerate any SRF and shortened the ensuing intervals. The retina community is unmistakably at the point where clear guidance is needed. Direction is particularly importance as the resulting loss in visual potential in real-world practice severely impacts the quality of life of millions of patients. A systematic literature search involving 123 studies, using MEDLINE, EMBASE, CINAHL, PsycINFO, PsychARTICLES and Health and Psychosocial Instruments, showed that impairment of vital tasks such as mobility, face recognition, meal preparation, shopping, cleaning, watching TV, reading, driving and self-care results in high rates of depression (Taylor et al., 2016). Readers in clinical trials may deviate with some discrepancy, while general ophthalmologist are prone to make larger errors that mislead injection decisions.

### 1.3. The origin of fluid in macular disease

In general, fluid in the retinal layers is the result of an imbalance of inflow between outflow mechanisms. Regarding inflow, leakage of fluid can develop as a result of two basic pathways: Transudation or exudation. Transudation refers to leakage of fluid across intact endothelial cell membranes, while exudation involves abnormal fluid movement across impaired cell membranes and a defective permeability barrier. This is well illustrated in the lung in general medicine and in the retina in RVO. Transudative pleural effusions due to congestive heart failure develop as a result of an increase in capillary hydrostatic pressure or increased oncotic pressure, while exudative pleural effusions due to inflammation or infection are the result of disrupted cell membranes and a defective permeability barrier comparable to in DME and nAMD (Broaddus and Light, 1992; Hiley et al., 2021; Paramothayan and Barron, 2002; Porcel, 2010). Regarding outflow, one has to consider the physiological pathways in the retina in which a bulk movement of fluid flows from the vitreous through the inner and outer retina and across the RPE into the choriocapillaris. The Na-K ATPase pump of the RPE and the intraretinal Muller cells are critical elements of this hydrostatic process, actively maintaining the retina in a water-tight state of deturgescence (Adijanto et al., 2009; Gallemore et al., 1997; Marmor, 1999; Reichenbach and Bringmann, 2020; Rizzolo, 2007; Spaide, 2016; Wimmers et al., 2007). Pathological fluid accumulates if the leakage is in excess of the local capability to remove the fluid. A disturbance of the RPE pump function alone may contribute to the build-up of SRF and may not be responsive to VEGF inhibition (Spaide et al., 2020b).

Most commonly, macular fluid is classified based on its relation to the retinal layers. Macular fluid can therefore be found inside the neurosensory retina (IRF), beneath the neurosensory retina (NSR), but above the RPE (SRF) or underneath the RPE, separating Bruch's membrane and the RPE (pigment epithelium detachment (PED)) (Schmidt-Erfurth and Waldstein, 2016) (Fig. 1, Fig. 2, Fig. 3). Macular fluids on OCT and their differentiation between distinct fluid compartments are essential biomarkers of exudative activity in nAMD, DME, RVO or central serous chorioretinopathy (CSC). However, the molecular processes

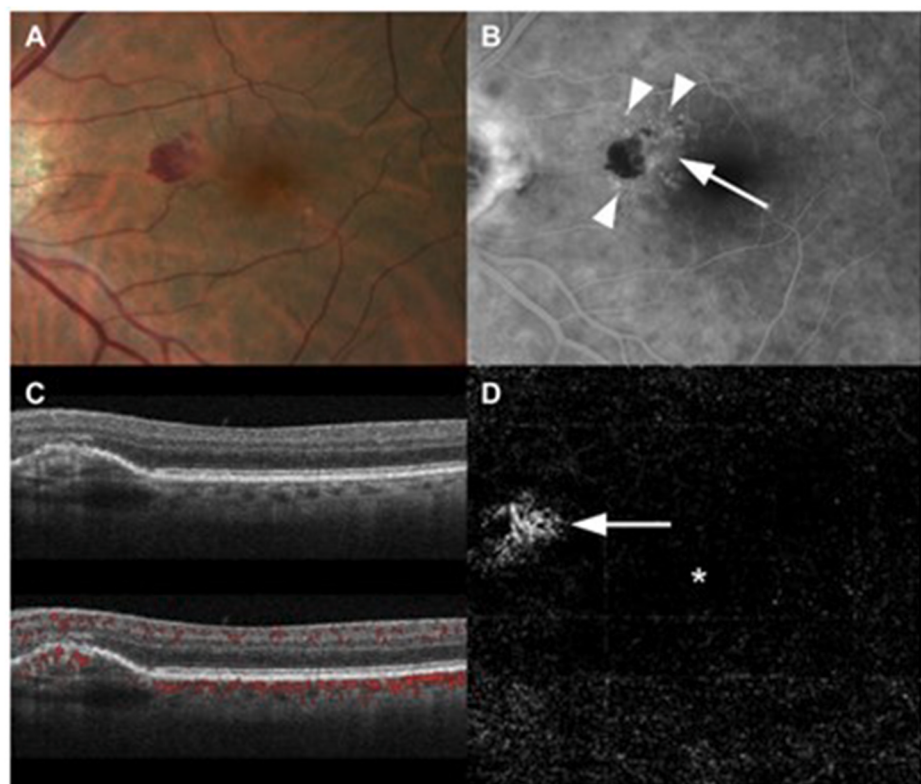


**Fig. 1.** Images showing type 1 macular neovascularization. A, Fundus photograph from a 78-year-old with hemorrhage in the nasal macula. B, Fluorescein angiography image showing blocking defect caused by the hemorrhage, subtle diffuse leakage (arrow), and punctate leakage (arrowheads). C, OCT image (top) demonstrating heterogeneous reflectivity in a fibrovascular pigment epithelial detachment and (bottom) OCT angiographic overlay showing flow within the pigment epithelial elevation. D, En face OCT image showing the neovascular network (arrow) and the center of the fovea (asterisk). Reproduced from (Spaide et al., 2020a).

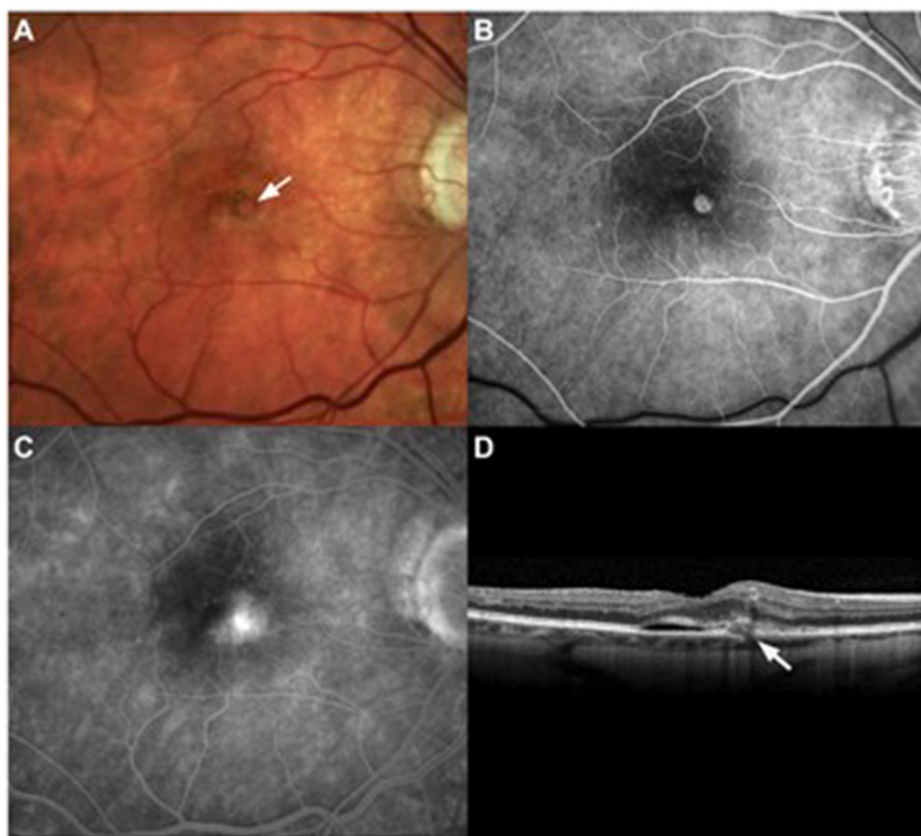


**Fig. 2.** Images showing type 2 neovascularization. A, Fundus photograph from a 74-year-old showing a hyperpigmented ring in the fovea (arrow). B, C, Early-phase fluorescein angiogram showing (B) a well-defined lesion with late leakage and (C) obscuration of the borders of the neovascular lesion. D, B-scan OCT showing the outer retinal lesion with extension of subretinal fluid under the fovea. The ingrowth site through the retinal pigment epithelium is evident (arrow). Reproduced from (Spaide et al., 2020a).

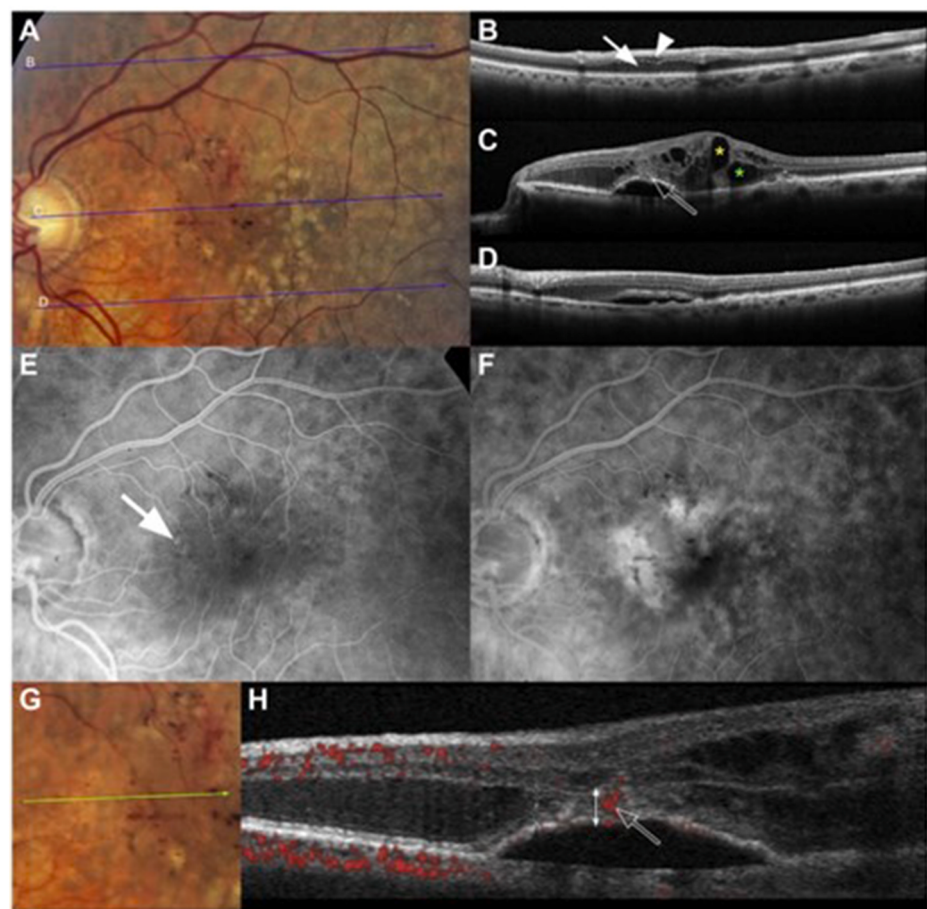


**Fig. 3.** Images showing type 3 neovascularization with prominent edema and hemorrhage. A, Fundus photograph from an 87-year-old showing dozens of small fleck hemorrhages in the superior and nasal macula. The blue arrows show the location of the structural OCT scans. B, OCT scan of the section through the superior arcade showing expansion of the inner nuclear layer (arrowhead) and Henle's fiber layer from edema fluid (arrow). C, OCT scan of the section through the superior parafovea revealing edema of the inner nuclear layer and Henle's fiber layer with cystoid spaces (yellow and green asterisks, respectively). Hyperreflectivity within the retina overlying the apex of the retinal pigment epithelial detachment (arrow) is evident. Note the edema nasal and temporal to the area of neovascularization is greater than that immediately surrounding the new vessels. D, OCT scan of the inferior macula showing edematous thickening of the retina and subretinal fluid. E, Fluorescein angiogram showing a small area of hyperfluorescence corresponding to the hyper-reflective area in (C). F, Later fluorescein angiogram showing pooling of dye in cystoid spaces as well as diffuse staining well away from the area highlighted by the arrow in (E). G, Fundus photograph of magnification of the central portion of the macula involved showing the numerous isolated hemorrhages, many of which were in the inner retina. The green arrow shows the section captured by the OCT angiogram in (H). H, OCT angiogram showing the small focus neovascularization found within the outer retina (open arrow). The vertical double arrow is 150 mm. Note that the hemorrhages do not colocalize with the neovascularization. Reproduced from (Spaide et al., 2020a). (For interpretation of the references to color in this figure legend, the reader is referred to the Web version of this article.)

need to be understood to appreciate the historical triumph of OCT-derived exudative biomarkers in respect to macular fluid and their importance for anti-VEGF therapy.

The discovery of a family of proteins called VEGF introduced a paradigm shift in understanding the pathophysiology of retinal exudative disease. VEGF is inseparably linked to the platelet-derived growth factor family. Two receptor tyrosine kinases with different actions are known for the VEGF ligand: VEGFR-1 and VEGFR-2. VEGFR-2 is the main pathway for the formation of choroidal and retinal neovascularization in retinal diseases, but vascular hyperpermeability is also triggered by the activation of VEGFR-2. VEGFR-1, on the other hand, may indirectly promote angiogenesis via mediating monocyte chemotaxis. In addition, VEGFR-1 induces matrix metalloproteinase (MMP)-9 function and triggers hepatic paracrine factor release. MMPs further amplify VEGF action by segregating matrix-bound VEGF, ultimately resulting in a feed forward loop of VEGF synthesis (Tolentino, 2009).

VEGF segregation can further be induced by hypoxia (Plate et al., 1992). This mode of action is especially relevant for diseases involving ischemic pathways such as diabetic retinopathy (DR), RVO or retinopathy of prematurity. The elevated VEGF concentrations in these diseases, and also in nAMD where choriocapillary flow deficits have been detected (Moult et al., 2020), might lead to an increased fenestration in vascular endothelium cells, together with the disbanding of tight junctions, resulting in exudation (Antonetti et al., 1999; Roberts and Palade, 1995). Following a VEGF increase, intercellular adhesion molecule-1 can also be segregated, which again promotes damage to the endothelium of the vessels with increased permeability and exudation (Miya-moto et al., 2000). This progressive feed forward upregulation of VEGF ultimately results in clinically significant macular edema and

neovascularization. This interactive mechanism of action explains the need to downregulate and minimize excessive VEGF release and why anti-VEGF has been such a success story in treating these diseases. VEGF expression and inhibition is the key feature behind fluid increase and decrease, its compartmentalization and dynamics in volume. It is nevertheless a complex and dynamic pathway.

Fluid in the setting of nAMD probably results from an impairment of exudative pathways related to impaired cell membranes and a defective blood ocular barrier associated with the neovascular membrane. Excess fluid may also develop as a result of non-exudative or transudative pathways in AMD. It became clear in the era of high-resolution spectral domain OCT (SD-OCT) that fluid can as well be encountered in eyes with non-neovascular AMD. Microcysts in the retina, typically located within the middle retina or the inner nuclear layer (INL) and originally referred to as pseudocysts (Cohen et al., 2010), can be identified with SD-OCT. They typically overly areas of RPE and outer retinal atrophy in the absence of neovascularization. These cysts should not be mistaken for exudative activity and may possibly be the result of cellular loss, including loss of Müller cells which are critical for hydrostatic homeostasis. Subretinal fluid can also complicate the non-neovascular form of AMD. In a recent study, Hiley et al. identified three OCT patterns of non-neovascular fluid: A crest of fluid over the apex of a drusenoid pigment epithelial detachment (dPED), a drape of fluid over soft confluent drusen and a pocket of fluid at the angle of a large druse or dPED (Hiley et al., 2020). Development of fluid in this context may be related to RPE disruption and RPE pump impairment. It is interesting that in this study the majority of these cases progressed to advanced forms of atrophy and the fluid was highly associated with other OCT biomarkers of atrophy indicative of a progressively degenerating RPE layer (Hiley et al., 2020; Jaffe et al., 2020). The association of fluid with

macular atrophy requires particular attention. Progression of nAMD, whether treated or not, leads to photoreceptor and RPE loss, and, finally, GA. Areas of GA were already present in 24.3% of eyes newly diagnosed with exudative AMD with a mean size of 1.23 mm<sup>2</sup> (Sikorav et al., 2017). Hence, not all fluid phenomena measured by sensitive AI tools are related to neovascular disease activity.

#### 1.4. OCT-based classification of nAMD and VEGF expression

Historically, macular neovascularization (MNV) in nAMD has been suggested to emerge from the choroid and has been classified based on invasive dye angiography into occult and classic choroidal neovascularization (CNV). However, with OCT technology, more detailed insights revealed the origin of intraretinal neovascularization. A new classification was needed to adapt to the rapid progress in imaging technologies, disease-associated imaging biomarkers and their genetic associations. The primary type of MNV strongly determines the bio-distribution of retinal fluid. SRF is detected in more than 50% of type 1, about 30% of type 2 and less than 5% of type 3 MNV lesions (Freund et al., 2020). Chen et al. showed that SRF was more commonly associated with Type 1 MNV, while IRF was more commonly associated with Type 3 MNV (Chen et al., 2016) (Figs. 1–3). In addition, polypoidal choroidal vasculopathy (PCV) has been closely linked to the same genotype as seen in conventional AMD and has now been integrated into the AMD classification as a form of type 1 MNV (previously occult CNV) (Spaide et al., 2020b). Yet, PCV differs in its pathomechanisms of fluid accumulation, as it is associated with primary disturbances in the choroidal circulation (Cheung et al., 2018). Classic CNV may represent type 2 MNV, according to the new OCT classification, and a mixed type 1 and 2 MNV may represent minimally classic CNV. Most importantly, neovascularization not originating from the choroid, previously referred to as retinal angiomatic proliferation, has been renamed type 3 MNV (Spaide, 2018) (Fig. 3). Moreover, AMD-specific phenotypes have been described according to the thickness of the choroid. Eyes with a thin choroid are more closely linked with type 3 MNV, subretinal drusenoid deposits and macular atrophy (Reiter et al., 2020b), while eyes with a thick choroid (i.e. pachychoroid) are more closely associated with type 1 MNV, including PCV. VEGF diffusing from the choroidal lesion to overlying inner retinal vessels may induce retinal capillary leakage with additional IRF release (Tolentino et al., 1996). Novel well-defined consensus definitions for neovascular nomenclature were therefore urgently needed to evaluate clinical outcomes and treatment response in correct relation to disease phenotyping (Spaide et al., 2020b). The primary phenotype definitions, however, are largely neglected in current routine clinical management and OCT-based fluid absence or presence is often used as the overriding basis for treatment decisions. Precise fluid localization and volumes by AI will further help to characterize and differentiate fluid dynamics in the different MNV entities. Neither type 3 MNV with fast IRF resolution nor type 1 MNV with substantial SRF pooling has so far been differentiated in anti-VEGF trials.

OCT has been adopted particularly in nAMD as a surrogate measurement of VEGF expression. Excessive VEGF release results in clinically relevant macular edema with significant loss of visual function. OCT can especially measure the extent to which macular fluid is present and may indirectly measure the level of VEGF release, a “VEGF-meter,” as termed by Rosenfeld. However, a “fluid-meter” that bridges the gap between vision loss and VEGF needs first to be established. The biological success of anti-VEGF therapy and morphological OCT features have been closely linked from the beginning. Experimental studies correlating the concentration of intraocular cytokines, including VEGF, with OCT-based fluid visualization revealed a solid relation between VEGF levels and disease activity, but not necessarily the absolute amounts of macular fluid with VEGF expression in different diseases such as nAMD, DME and RVO (Funk et al., 2010, 2009). Extrapolations should not therefore be made from AI-determined fluid dynamics to levels of VEGF expression or inhibition. A more realistic approach is the

introduction of AI-based fluid analysis.

Mixed mechanism pathways of fluid leakage should also be considered. Persistent or residual subretinal fluid has been encountered in various pivotal trials of anti-VEGF therapy, e.g., in 25–50% of eyes at various endpoints of the trials (1 year or longer) (Dugel et al., 2020a; Heier et al., 2012; Maguire et al., 2016). While recalcitrant subretinal fluid may indicate persistent exudative neovascular activity warranting close monitoring, and in some cases more aggressive anti-VEGF therapy, other non-exudative pathways should be considered such as an impaired RPE pumping capacity and/or Müller cell disruption. It is interesting that persistent SRF at the end of various prospective trials has been correlated with more favorable visual outcomes (Sharma et al., 2016). Recalcitrant SRF may indicate an impaired RPE pump, while frank RPE loss and atrophy may be associated with an unimpeded passage of fluid into the choroid.

Direct measurement of excessive fluid and its presumed function as a fluid-meter has disrupted conventional procedures in patient management. OCT and fluid measurement alone, without dilated fundus examination (DFE) and often without visual acuity assessment, has been proposed as a fast, safe and cost-efficient way to tackle the great need for timely treatment in busy outpatient clinics (Trivizki et al., 2020). In addition to eliminating BCVA assessments and DFE, time taken for scrolling through OCT volumes of individual patients and between individual visits can be saved when using automated precision measurement of macular fluids. This will result in further time saving, both for patients and clinical staff, and cost per encounter. Patients will be able to visit the clinic more often and efficiency and safety will also improve, allowing clinicians to see more patients during a day. An objective quantification of macular fluid with OCT is therefore becoming more and more critical in guiding the diagnostic and therapeutic evaluation of nAMD (Dugel et al., 2020a; Heier et al., 2012; Maguire et al., 2016). Fluid volumes as personalized OCT biomarkers are developing to become the most important factors in guiding the management of nAMD. Between 55 and 75% of the ophthalmologists questioned in the 2020 Preferences and Trends survey by ASRS hoped that more durable drugs will soon reduce the patient volumes in nAMD, DME and RVO. AI-based automated fluid analyses is the most efficient monitor for all of these substances and strategies.

#### 1.5. Fluid in the diabetic macula

High-precision localization and quantification of IRF/SRF increase and decrease over time shed light on the pathognomonic fluid dynamics in each disease. To establish AI’s potential in DME, a pilot analysis of fully automated retinal layer and fluid segmentation was undertaken in 629 patients receiving anti-VEGF therapy for DME in a randomized clinical trial (RCT). Of the 312 potentially predictive features it attempted to define at three time points (baseline, weeks 12 and 24), intraretinal cysts (IRC) in the outer nuclear layer (ONL) had the greatest predictive value for BCVA at baseline, and IRC and CRT in the 3-mm area at weeks 12 and 24 for BCVA after one year (Gerendas et al., 2017).

However, leakage in diabetic macular disease has an entirely different origin and dynamic to that in nAMD. In general, retinal morphology and function rely heavily on the integrity of the blood retinal barriers (BRB). Current therapeutic practices recommended for DME focus mostly on addressing the endothelial component of the inner BRB, and anti-VEGFs are the most effective anti-permeability agents available to date. Similar therapeutic effects on fluid levels as in AMD could therefore be expected. There are, however, other cellular components to the barrier that collaboratively constitute the inner BRB such as pericytes, astroglia and Müller cells. Loss of pericytes is thought to be an early pathologic feature of diabetes, which weakens the integrity of the barrier, compromises endothelial cells and leaves them primed to respond to pathologically elevated VEGF (Park et al., 2017). These differential structural pathomechanisms can be better recognized and understood by AI-based fluid identification, localization and quantification

under therapy.

IRF is the most obvious fluid type in DME because retinal endothelial cells constitute the first cellular component of the barrier, with inter-cellular adhesions (tight, gap and adherens junctions) controlling paracellular transport to particles less than 3 nm in size. In addition, trans-cellular active transport is tightly regulated via caveolae (transcytosis) or specific receptor transporters and is the predominant entry way for macromolecules (Klaassen et al., 2013). Blood retinal barrier breakdown is associated with dysfunction in both trans- and inter-cellular endothelial barriers. Notably, VEGF has been shown to disrupt the BRB by affecting both the transcellular vesicular pathway and the integrity of intercellular adhesions (Díaz-Coránguez et al., 2017; Klaassen et al., 2013). VEGF inhibition restores the BRB by allowing the physiological transretinal transport mechanisms to pump the IRF out. Extravasation of lipids seen as hyperreflective foci (HRF) in OCT analyses are therefore another relevant leakage variable which should be quantified, e.g., with AI tools (Zur et al., 2018).

Regarding pericytes, their pathophysiological role in supporting and maintaining the BRB has been studied extensively. Experiments with transgenic mice showed pericyte depletion during development to be associated with severe disruption of retinal vasculature and ultimately vision loss (Park et al., 2017). Interestingly, pharmacologically depleting the pericytes in adult mouse retina induced a variety of downstream effects, including sensitizing the endothelial cells to the effects of VEGF-A, activation of macrophages and retinal inflammation and leakage in a dose-dependent fashion, illustrating the importance of these perivascular cells in maintaining retinal integrity and function (Ogura et al., 2017). Depletion of pericytes is not immediately reversible by intravitreal VEGF inhibition, and a much slower fluid resolution in DME compared with nAMD is typically measured by AI-mediated fluid segmentation (Roberts et al., 2020).

Other mediators such as angiopoietins 1 and 2 (Ang 1 and 2), which are tightly balanced ligands of the endothelial Tie-2 receptor, are emerging as having an important role in retinal vascular function and pericyte survival (Díaz-Coránguez et al., 2017). Notably, Ang 2 has recently emerged as a potential therapeutic target (Sahni et al., 2019). It has been shown to be overexpressed in diabetic eyes (Patel et al., 2005) and its overexpression is associated with vascular regression, pericyte detachment and vascular leakage (Pfister et al., 2010). Simultaneous Ang 2 inhibition with faricimab demonstrated a statistically significant gain of +3.6 letters over ranibizumab with extended durability in the BOULEVARD trial (Sahni et al., 2019). AI-based quantification of macular fluid dynamics in ongoing clinical trials using different therapeutic mechanisms will offer a unique method to verify such novel therapeutic target concepts.

In addition to their role in the inner BRB, Muller cells have a critical role in maintaining retinal fluid homeostasis by removing extracellular water through co-transport of potassium and water into the blood, facilitated by aquaporin 4 (Bringmann et al., 2006). Further, in hypoxic environments and when exposed to blood-derived cytokines during BRB breakdown, these cells respond by activating the gliosis mechanism as well as secreting proangiogenic factors, including VEGF with the potential to further exacerbate retinal leakage and BRB disruption (Bringmann et al., 2006). These multiple biological alterations pathognomonic for diabetic macular disease reinforce each other in a complicated interaction, which is likely reflected in disintegration of inner neurosensory layers (Schmidt-Erfurth and Michl, 2019). A precise layer segmentation in DME is therefore typically complicated for both human experts and automated tools.

A recent comparison of fluid behavior using AI demonstrated that in each individual disease, at every timepoint, most IRF was present at the fovea, followed by the paracentral and pericentral ring ( $p < 0.0001$ ). While this was also true for SRF in RVO/DME ( $p < 0.0001$ ), patients with nAMD showed more SRF in the paracentral ring than in the fovea ( $p < 0.0001$ ). Among the early treatment diabetic retinopathy study (ETDRS) sectors, patients with DME presented the highest IRF volumes

temporally ( $p < 0.0001$ ). Under VEGF inhibition, the investigators measured differential reductions of initial fluid volumes per disease and a different dynamic over time at 1 vs 12 months: The IRF resolution between 1 and 12 months was 95.9%/97.7% in RVO and 91.3%/92.8% in nAMD, but only 37.3%/69.9% in DME. That rate was different for SRF with 94.7%/97.5% resolution in RVO, 98.4%/99.8% in nAMD and 86.3%/97.5% in DME (Michl et al., 2020a). The slower IRF resolution in DME is a result of the multiple biological pathways described above.

While less well understood and studied, the RPE as the outer BRB is also thought to be affected in diabetes (Tonade and Kern, 2020), which should be most reflected in the dynamics of SRF volumes. Regarding the correlation of fluid and function, it must be considered that photoreceptors have been implicated in exacerbating the vascular dysfunction in diabetic retinopathy. Rodent experiments showed that retinal vascular leakage was abrogated in diabetic rodents that had a total loss of photoreceptors, implicating photoreceptor-derived cytokines in the process of BRB leakage (Tonade et al., 2017). Interestingly, a recent study of a retinal model of primary photoreceptor degeneration (non-diabetic) revealed that the outer BRB (early) and deep retinal capillaries (later) show evidence of leakage, disruption and loss of integrity (Ivanova et al., 2019). Of note, the deep capillary leakage was tightly associated with RPE migration and cone degeneration, showing the intricate interplay between the inner and outer BRB and suggesting a highly complex interaction between these barriers and the photoreceptors. In RVO, which shares the primary retinal vascular origin of fluid leakage into the retina with DME, significant correlations with BCVA were seen for a 100- $\mu$ m increase in central subfield thickness (CST; -3.1 letters), intraretinal cysts at the center point (CP; +4.1), SRF at CP (+3.0) and HRF at the central B-scan (-2.2) (Michl et al., 2020b). Hyperreflective foci are a common feature in DME-related exudation and were assigned to migrating RPE cells and/or lipid exudates. Automated image segmentation of HRF revealed that higher numbers of HRF were significantly associated with longer diabetes duration and morphological OCT characteristics, including CRT ( $p = 0.004$ ), cysts ( $p < 0.001$ ), subretinal fluid ( $p = 0.001$ ), and disruption of the external limiting membrane ( $p = 0.018$ ), suggesting a role for HRF as a clinically relevant biomarker for disease severity in DME (Schreuer et al., 2020). The OCT pattern of HRF may also represent a sign of inflammation, with important pathophysiological implications (Agarwal, 2019).

### 1.6. Human expert and AI-based automated fluid evaluation

Anti-VEGF intraocular injections are considered the standard care for the treatment of nAMD, DME and macular edema due to RVO, but identifying the optimal monitoring and treatment regimens in clinical trials and routine practice remains elusive (Boyer et al., 2012; Heier et al., 2012; Holz et al., 2013; Nguyen et al., 2012; Rosenfeld et al., 2006; Wells et al., 2015). To optimally avoid fluid occurrence in the macular retina, T&E protocols have been widely adopted for anti-VEGF treatments, tailoring injections on the basis of patient response by proactive intervention before fluid occurs (Silva et al., 2018; Wykoff et al., 2015). Nevertheless, any patient-tailored protocol requires clinicians to determine reinjection intervals based on the presence of fluid on OCT (DeCroos et al., 2012). Retreatment criteria and retinal fluid evaluation are thoroughly defined in clinical trials and the investigators' performance overseen by certified readers, considered as high-performing experts. Most relevant definitions for the delineation of macular fluid were introduced by reading centers performing in trials for approval of anti-VEGF substances. In times of automated AI reading, such human experts' rules and criteria are used as ground truth for the validation of automated algorithms. Moreover, retrospective analyses of clinical trials, with their perfectly phenotyped and monitored populations and datasets, are commonly used to train AI algorithms or obtain reliable information from the application of AI-based tools about disease activity and therapeutic response (Roberts et al., 2020; Schmidt-Erfurth et al., 2020b).

Based on preexisting expert readers' discretion, IRF was defined as exudation visible within the NSR, including all layers between the internal limiting membrane (ILM) and the ellipsoid zone. The biomarker IRF is, however, already difficult for a human to evaluate precisely, and this is magnified by the diversity of real-world judgement. IRF can be measured in three ways: Identification of cysts, measurement of thickening of the individual retinal layers and measurement of total retinal thickness. Cysts are a common feature of IRF and easiest for readers and clinicians to identify. The University of Wisconsin Fundus Photograph Reading Center (FPRC) grading protocol defines cystoid spaces as hypo-reflective, well-delineated and at least 40 µm in height within the NSR (Domalpally et al., 2009). Multiple cysts can coalesce together causing them to lose their individual circular shape and merge into retinal layers (Fig. 4). Although outer retinal tubulations are similar in appearance to cysts, tubulations are considered a sign of neurodegeneration consisting largely of cones lacking outer and/or inner segments and only Müller cells forming an external limiting membrane (Espina et al., 2016). Thickening of individual retinal layers can occur and may be difficult to identify in the absence of cysts. To identify IRF in the absence of cysts, the FPRC grading protocol encourages human graders to recognize asymmetric thickening of the ONL or loss of a normal foveal contour (Fig. 5). Because OCT technology depends on directional reflectance, the Henle's layer can be more obvious with a tilt of the OCT scan, resulting in asymmetric reflectivity of outer retinal layers (Lujan et al., 2011). Human graders take this artifact into consideration before documenting IRF without cysts. Within FPRC, intergrader agreement on cystoid vs non-cystoid IRF is 88% (kappa 0.78, n = 922 eyes). Such inter- and intra-grader comparisons are an essential requirement to assure accuracy of human expert readings. When 1213 pairs of time-domain (TD-) and SD-OCT scans from the CATT study were analyzed by the Duke Reading Center, agreement on IRF was 73%, with artifactual interpretation of dark areas as cystoid edema as a main issue (Folgar et al., 2014). However, substantial disagreement regarding fluid determination has been found, even among expert graders. Within a reader team composed of two independent readers and a senior reader in the CATT study, the percent agreement was 73% for IRF with a kappa of 0.48, 90% for SRF with a kappa of 0.80 and 88% for sub-RPE fluid with a kappa of 0.75 (DeCroos et al., 2012). This disagreement occurred, however, in a purely qualitative analysis of macular fluid, and is far from representative of quantitative three-dimensional volume measurements. As reader performance is highly standardized and based on hundreds and thousands of individual B-scans, it represents an "ideal world," which often clashes with the high variability in the diagnostic discretion of even experienced real-world experts. A standardized comparison of reader performance and clinical investigators revealed reading center

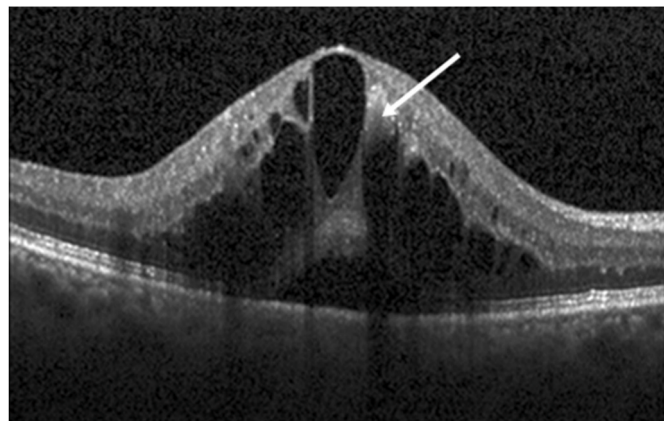


**Fig. 4.** Optical coherence tomography scan in an eye with retinal vein occlusion showing intraretinal fluid with a large central cyst and multiple coalesced cysts along with subretinal fluid. Hemorrhage (arrow) blocks the reflectivity of underlying layers and interferes with delineation.

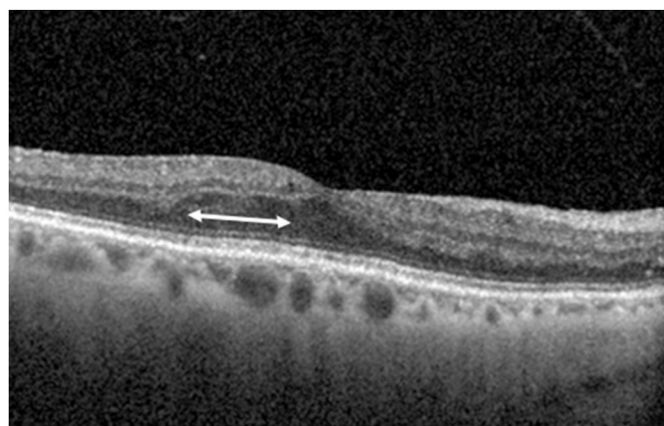


**Fig. 5.** Optical coherence tomography scan of an eye with diabetic macular edema showing thickening of the outer nuclear layer with loss of foveal contour. The arrow displays the lateral extent of the thickening.

fluid determination agreed in only 72.1% and disagreed in 27.9% of visits, with no discrepancies seen only in 20.9% of patients. Deviations occurred more commonly with lower total foveal thickness (mean  $\pm$  SD:  $265 \pm 103$  positive fluid discrepancy,  $366 \pm 151$  µm positive fluid agreement), presence of intraretinal fluid only and smaller fluid areas (Toth et al., 2015). As IRF in particular is considered as the major negative impact on BCVA, such incorrect judgement should clearly be avoided.

Central retinal thickness measurement is the third indicator of IRF. Most OCT segmentation algorithms measure CRT from the ILM to the RPE, presenting a priori a blend of both IRF and SRF. However, in other studies total CRT is measured from the ILM down to Bruch's membrane (BM), even including RPE detachments, which most strongly distorts CRT values. Central subfield thickness is the most commonly used variable in clinical trials and, most disturbingly, retreatment by protocol is based on CRT/CST values. The Diabetic Retinopathy Clinical Research (DRCR) network uses an algorithm based on changes in CST and visual acuity to determine reinjection criteria (Aiello et al., 2011). Despite volumetric scans being available, retinal volume of the entire scan is currently not used as a clinical trial outcome, primarily due to segmentation errors and the associated burden involved in editing the boundary lines across the entire scan (de Azevedo et al., 2020). A simplified system used in clinical trials includes digital caliper measurements at the foveal center point of the individual compartments to distinguish IRF and SRF (DeCroos et al., 2012). A post hoc analysis in both the CATT and IVAN studies showed eyes with IRF had worse visual acuity than those with SRF (Evans et al., 2020). Larger cyst size and the presence of SRF have been shown to have a better prognosis in DME studies (Gerendas et al., 2018a). Fluctuating CST has been shown to be associated with poor prognosis in both DME and nAMD (Ehlers et al., 2020; Evans et al., 2020). These results indicate that quantitative assessment of fluid along with subtyping into IRF/SRF is most relevant for optimal treatment decisions. This is particularly relevant during long-term management of patients receiving anti-VEGF, where fluid volumes are small and progressive BCVA loss is almost the norm in real-world care.

A central pocket of SRF in the setting of retinal vascular diseases such as DR and RVO may be the result of Muller cell traction on the central bouquet (Lenis et al., 2020), but in more severe cases is likely the result of exudative complications. FPRC intergrader agreement on the presence of SRF and involvement of the central subfield is high, at 93% (kappa 0.87, n = 922 eyes). Although identification of SRF is more reproducible than for the various cystoid spaces in IRF, measurement of SRF is nuanced by a few coexisting features. The roof of the dome can present with irregular thickening considered to be photoreceptor debris (Fig. 6, (A)) (Spaide, 2008). Subretinal hyperreflective material (SHRM)

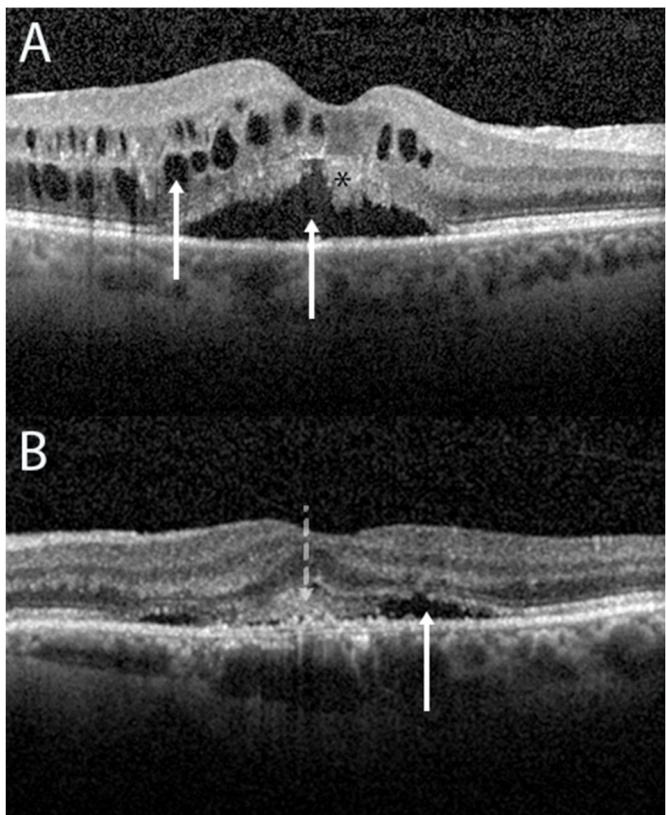


**Fig. 6.** Optical coherence tomography (OCT) scan of an eye with diabetic macular edema (A) showing cysts, subretinal fluid (arrow) and hyperreflective debris at the photoreceptor layer (asterisk). OCT scan of an eye with neovascular age-related macular degeneration (B) showing subretinal fluid (solid arrow) and subretinal hyperreflective material (discontinuous arrow).

is another feature associated with nAMD and can coexist with the hyporeflective SRF component (Fig. 6, (B)) (Willoughby et al., 2015). Caliper measurements of the subretinal space do not distinguish SRF and SHRM, which is a major issue as SRF has a positive prognostic impact, while SHRM is the leading feature for development of vision-disturbing subretinal fibrosis (SF) (Roberts et al., 2019). The border between SHRM and RPE cannot be distinguished in advanced cases, particularly with preexisting fibrosis, and the subretinal and sub-RPE space become a continuum (Willoughby et al., 2015). Fluid detection in reading centers is based on the presence of SRF/IRF, whereas clinician interpretation is geared towards fluid significant enough for a repeat injection. What the clinically relevant threshold should be has yet to be determined in prospective clinical trials.

Considering the complexities involved in human graders measuring SRF, deep learning methods have the potential to provide a better way of fluid quantification (Keenan et al., 2020a; Moraes et al., 2020; Schmidt-Erfurth et al., 2020b). Other studies have shown a substantial disagreement between clinicians' interpretation in the detection of fluid (Keenan et al., 2020b; Toth et al., 2015). Human investigators detecting retinal fluid in the AREDS 2 study had an accuracy of 0.805, a sensitivity of 0.468 and a specificity of 0.970 (Keenan et al., 2020b). Therefore, a comprehensive assessment of fluid in retinal diseases needs to consider the presence, subtype, center-involvement, severity and volume of each fluid component within each B-scan of an entire standard OCT volume. Although automated methods of fluid detection are successfully evolving, a reference standard that could help fine tune the process is lacking (Schlegl et al., 2018). Physicians' interpretation of clinically significant fluid is subjective and therefore prone to weak agreement. Reading center detection of fluid is standardized and reproducible, but does not encompass the severity component. Future research in an era of

telemedicine, large clinical trials, analysis of "real-world" data and AI-guided therapies with automated fluid detection needs to include reference standards that can incorporate clinical significance in a reproducible way. AI-based detection simply of the presence or absence of IRF/SRF alone without any accurate measurement of the amount of fluid was recently proven superior regarding sensitivity and specificity of fluid detection in a retrospective analysis of the AREDS 2 study dataset (Keenan et al., 2020b).

Little effort has been invested in proof-of-principle for the level of performance of AI systems versus clinicians. A systematic review of the design, reporting standards, risk of bias, and claims of studies comparing the performance of diagnostic deep learning algorithms for medical imaging in general with that of expert clinicians found only 10 records for deep learning-based randomized clinical trials, of which two are published and eight are ongoing. Of the 81 non-randomized clinical trials identified, only nine were prospective and just six were tested in a real-world clinical setting (Nagendran et al., 2020). Regarding the accuracy of referral recommendation on a range of sight-threatening retinal diseases, investigators demonstrated AI performance reaching and mostly exceeding that of four ophthalmologists (De Fauw et al., 2018). Future studies are urgently needed to enhance real-world clinical evidence and reliable conclusions, particularly in the most promising field of retinal image analysis (Nagendran et al., 2020).

## 2. The technology of AI-based fluid localization and quantification

Localization of retinal fluid on OCT and its subsequent volume quantification fundamentally relies on having accurate AI-based *image segmentation* methods which assign to the respective OCT voxels a label denoting the fluid-type, see Fig. 7. After localizing the fluid in a volumetric scan, a two-dimensional en face topographic map of fluid distribution in the macula can be computed and displayed (Fig. 8). This furthermore allows quantification of the volume of the fluid identified, not only for an entire OCT scan but also for a specific local region spatially defined by, e.g., a standard ETRDS grid. Fluid volumes are most commonly expressed in *nanoliter* (nl) units to avoid using long decimal numbers as  $1 \text{ nl} = 0.001 \text{ mm}^3$ .

The estimates of fluid volume quantities are tightly coupled with the available spatial resolution of the OCT scan acquired. In particular because the number of OCT B-scans acquired and the physical spacing between them can vary between different imaging settings and different OCT device manufacturers. Fig. 8 illustrates how an OCT scan, when its spatial resolution is reduced, can produce largely different estimates of IRF and SRF volumes compared with the original high-resolution scan. From the figure, we can observe that this is especially problematic with OCT scans with less than 30 B-scans covering a 6-mm range, as such a low spatial resolution hinders obtaining precise volumetric estimates of small fluid pockets.

For AI-based fluid assessment to provide an effective clinical decision support, in addition to an appropriate OCT scanning pattern, several further aspects have to be taken into consideration. Due to the large number of fluid pockets potentially present in a scan, the assessment methods should be fully automated, as even minimally interactive approaches would be too labor-intensive and consequently of very limited clinical use. Furthermore, a fully automated assessment ensures an objective and repeatable fluid quantification. Finally, the runtime of the AI algorithm should be short and clinical workflow integration sufficiently tight to avoid increasing the duration of an eye examination at a standard clinical visit. Ideally, a complete assessment of fluid should be accessible in real-time by a mouse click only.

The importance of localizing and quantifying retinal fluid on OCT scans was recognized early on. The very first work on OCT fluid segmentation was proposed by Fernández (2005), shortly after the first commercial OCT devices appeared on the market. Before the introduction of deep learning segmentation models, traditional machine learning

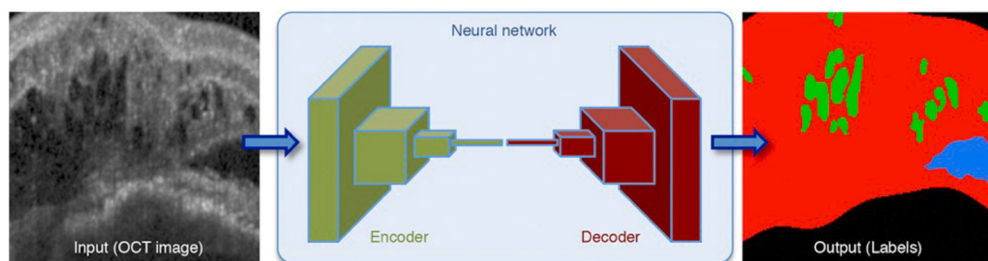


**Fig. 7.** Convolutional neural network with an encoder-decoder architecture to segment intraretinal fluid (green), subretinal fluid (blue), and retinal tissue (red). Reproduced from (Schlegl et al., 2017). (For interpretation of the references to color in this figure legend, the reader is referred to the Web version of this article.)

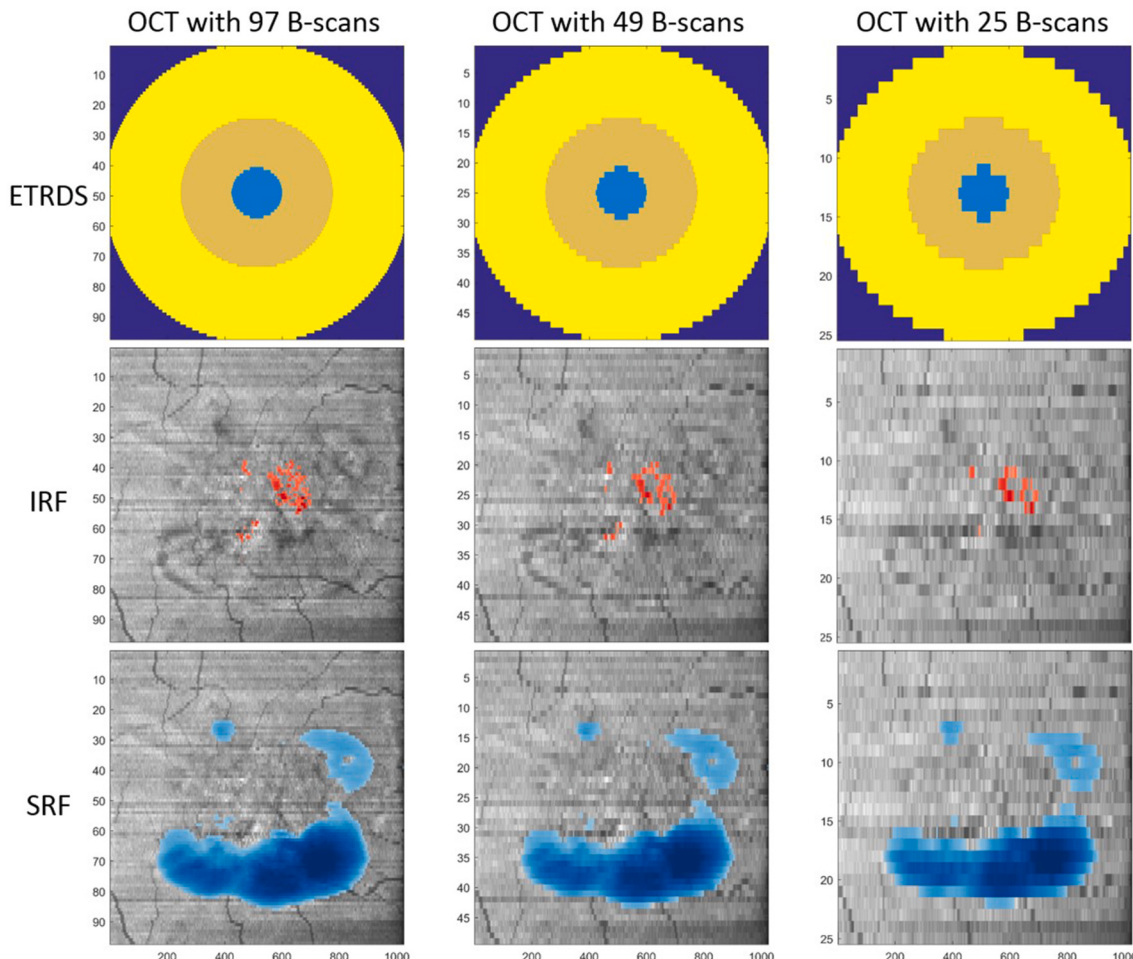


**Fig. 8.** Fluid localization and quantification variability across three different scanning patterns. The optical coherence tomography (OCT) scan was acquired with 97 B-scans (left column), and then the 49 B-scan (middle) and the 25 B-scan (right) versions were artificially obtained by sequentially removing every second B-scan. Intraretinal fluid (IRF) and subretinal fluid (SRF) volumes were computed for the central 1-mm, 3-mm and 6-mm disks of the Early Treatment Diabetic Retinopathy Study (ETDRS) grid (top row). The estimated IRF volume in the central 6 mm varied from 17.3 nl (97 B-scans), 15.7 nl (49 B-scans) to 14.3 nl (25 B-scans), an underestimate of 20%. The SRF volumes were less affected and for the central 6 mm varied from 529.3 nl (97 B-scans), 529.7 nl (49 B-scans) to 534.4 nl (25 B-scans).

approaches were applied, where a *classifier* was trained to label each OCT voxel based on a set of handcrafted features describing its surrounding image appearance.

The output of such voxel-level classifiers was then coupled with the two dominant segmentation frameworks of that time: *Graph-cuts* (Boykov et al., 2001; Boykov and Funka-Lea, 2006) and *level sets* (Caselles et al., 1997; Sethian, 1999). Several prominent studies have applied fluid segmentation methods using such machine learning approaches, including (Chen et al., 2012), (Xu et al., 2015), (Chiu et al., 2015), (Wang et al., 2016), (Chakravarthy et al., 2016), and (Novosel et al.,

2017). Nowadays, deep learning segmentation models based on training convolutional neural networks (CNNs) are state-of-the-art due to their ability to learn from labeled training examples *end-to-end*, i.e., without the need for explicitly engineering features representative of retinal fluid. Thus, in this review we will focus on those approaches exclusively. But before surveying the methods, it is important to define how the fluid segmentation performance can be evaluated.

## 2.1. Performance evaluation

The most common measure for evaluating image segmentation performance is the *Dice similarity coefficient* (DSC), which is a measure of overlap expressed as “intersection over union” between the segmented and reference pixels. The value of DSC varies from a score of 0 (complete lack of overlap) to a score of 1 (perfect overlap) and is defined mathematically as the (harmonic) average between a method’s *precision* and *recall*:

$$\text{DSC} = 2 \frac{\text{precision} \times \text{recall}}{\text{precision} + \text{recall}} = \frac{2\text{TP}}{2\text{TP} + \text{FN} + \text{FP}}, \quad (1)$$

where TP, FP and FN denote the number of pixels that are true positives, false positives, and false negatives. An advantage of the DSC is that it ignores the often-plentiful true negatives of the background, which otherwise would dominate the measure. Downsides of the DSC are that it does not directly represent a clinically relevant parameter and its high sensitivity to errors when tiny amounts of fluid are present, because then even a small amount of FP and FN voxels can be comparable in size to the number of TP voxels. Thus, DSC values are often reported by scan subgroups stratified by the reference fluid volume sizes.

In addition to the DSC, measures with direct clinical interpretation are often considered. These have a specific focus, primarily fluid volumes in the central 1-mm, 3-mm or 6-mm regions. Computing the *Limits of Agreement* (LoA) is statistically preferred over computing a correlation for measuring how the AI-based fluid volumes compare with the reference volumes, typically obtained from manual annotations. Such LoA are represented with a Bland-Altman plot (Bland and Altman, 1986), which in addition to the limits also shows a possible *bias* introduced by the method (Fig. 9).

The performance of a fluid detector (a presence or absence of fluid in a scan) is traditionally evaluated by measuring the receiver operating characteristic (ROC) curve and calculating the associated area under the ROC curve (AUROC), which is a measure of performance irrespective of the actual operating point chosen. Choosing an operating point on the ROC provides the corresponding *sensitivity* and *specificity* of the method. It is important to note that for the sensitivity and specificity performance to be validated, the operating point needs to be selected *before* the final evaluation on the test set. Although an AUROC is the most commonly used detection metric, in the case of highly unbalanced datasets, where only a few scans contain fluid, the area under the precision-recall curve (AUPR) is the more appropriate measure because, similarly to DSC, it focuses on positive predictions, corresponding to the minority but clinically more important set of scans (Yanagihara et al., 2020).

### 2.1.1. Inter-observer variability

Datasets containing scans that have been annotated by multiple observers (image annotators) offer valuable insight into the inter-observer variability and the corresponding ceiling of the performance that the segmentation methods can reach when trained from manual

annotations. Lee et al. (2017b) reported a mean DSC for human inter-observer variability of 0.75. As part of an international RETOUCH fluid segmentation and detection challenge (Bogunović et al., 2018), an inter-center inter-observer variability of DSC = 0.71 ( $\pm 0.17$  SD) for IRF, and a DSC = 0.73 ( $\pm 0.20$  SD) for SRF was reported on a large multi-device multi-disease dataset. With respect to fluid volumes, an inter-observer standard deviation of 100 nl for IRF and 40 nl for SRF across the baseline scans of treatment-naïve eyes was reported in RETOUCH. This illustrates the difficulty of fluid annotation on OCT, even when performed manually by experienced image annotators, particularly in annotating IRF pockets in scans with a low signal-to-noise ratio.

## 2.2. Fluid localization with supervised learning

Soon after Krizhevsky et al. (2012) discovered CNNs were highly successful at image recognition, they were redesigned to address the image segmentation task by training them to learn the mapping from raw OCT intensity images to dense voxel-wise tissue class labels. A popular initial approach was based on *patch classification*, where each pixel was classified separately using an image neighborhood (patch) surrounding it. The main reason for using patches was that CNNs’ components were made of fully connected layers that required a pre-specified fixed input size image. Schlegl et al. (2015) developed such a patch-based classification CNN for the task of fluid segmentation on OCT. In this first deep learning approach to fluid segmentation, a multi-scale CNN model was proposed that used patches of two different sizes to capture both small and large fluid pockets, and furthermore it was trained to distinguish between IRF and SRF fluid types.

Entirely convolutional neural networks (FCNNs) were proposed soon afterwards, without the need for fully connected layers (Long et al., 2015). Besides operating substantially faster than patch-based models, they allowed segmentations to be obtained from images of arbitrary sizes and opened the door for an image-to-image training, where CNNs learn to directly translate the input OCT image into the output image of labels. Thus, all of the subsequent segmentation models adopted the FCNN paradigm. A standard image segmentation CNN architecture consists of two processing components, an encoder and a decoder (Fig. 7). The encoder gradually encodes a high-resolution input image into an internal representation based on a few artificial neurons, and the decoder gradually recovers this abstract image representation to a full resolution image with pixels assigned to their respective labels. Note that such a processing pipeline closely resembles the human visual pathway, where an incoming image of the world is first captured with a high-resolution array of photoreceptors in the retina. It is then relayed to the brain through a comparably small number of neurons within the lateral geniculate nucleus and is consecutively reconstructed back to a high-resolution image within the primary visual cortex. Hence, AI-based image analysis in the retina should be understood and trusted naturally by the ophthalmological community.

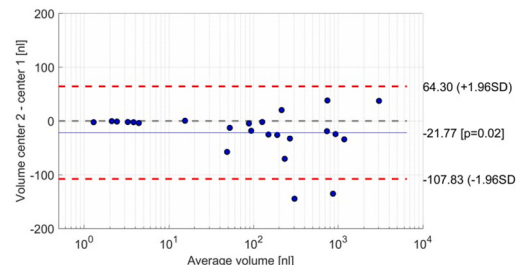
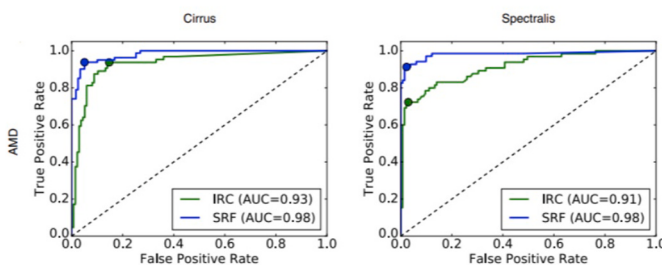


**Fig. 9.** (Left) Examples of receiver operating characteristic curves with operating points denoted for detecting fluid in patients with age-related macular degeneration (AMD) from scans acquired with Cirrus and Spectralis optical coherence tomography (OCT) devices (Reproduced from Schlegl et al. (2017)). (Right) Example of a Bland-Altman plot illustrating the inter-center, inter-observer limits of agreement (in red) in manual subretinal fluid (SRF) volume annotations (Reproduced from Bogunović et al., 2019)). (For interpretation of the references to color in this figure legend, the reader is referred to the Web version of this article.)

The current state-of-the-art CNN architecture for image segmentation is a *U-net* (Ronneberger et al., 2015), which further includes the so-called shortcut or *skip-connections* across an encoder and decoder to facilitate the fine-detail recovery by a decoder. There have already been multiple works that used and evaluated CNNs to show that they produce accurate fluid segmentations as outlined next. Lee et al. (2017b) used a U-net for a segmentation of IRF with a training set composed of 1289 annotated B-scans. The model achieved a DSC of 0.73, close to the inter-observer variability of DSC = 0.75, on a test set of 30 B-scans annotated by multiple experts. Schlegl et al. (2017) developed a CNN to segment IRF and SRF individually (Fig. 7). Its performance was extensively evaluated across a range of the main retinal diseases and OCT device manufacturers. The method was cross-validated on a very large dataset of 354 fully annotated OCT volumes comprising three main exudative diseases, nAMD (212), DME (32), RVO (110), and two OCT vendors, 268 Cirrus (Carl Zeiss Meditec, US) and 86 Spectralis (Heidelberg Engineering, Germany).

Further studies showed that CNNs can indeed be adapted to a specific OCT device vendor and macular disease. Venhuizen et al. (2018) implemented a multi-scale network that used a range of contextual windows to segment IRF. The method consisted of a cascade of two U-nets with two complementary tasks: The first one aimed at delimiting the retinal region (Venhuizen et al., 2017) and the second at segmenting IRF by integrating the output of the first U-net. A total of 221 OCT volumes from 151 patients (6158 B-scans) were used, from which the testing and evaluation had been performed on 99 OCT volumes (2487 B-scans) from 75 patients. To obtain segmentations from scans of different OCT manufacturers, a small amount of device-specific data was used for CNN fine-tuning. The authors reported a DSC of 0.79 and, furthermore, demonstrated a good robustness and generalization to the scans of other device manufacturers (DSC = 0.72).

A system developed by Google DeepMind for OCT-based diagnosis and clinical referral (De Fauw et al., 2018) used a 3D U-net (Çiçek et al., 2016) to segment IRF and SRF within a total of 15 different retinal labels. Nine contiguous B-scan slices were used as a 3D context input to segment the middle B-scan. In addition, to identify ambiguous regions, an ensemble of five instances of the network was constructed by training with a different order over the inputs and different CNN initializations. Networks were trained on 877 Topcon (Topcon, Japan) and 152 Spectralis (Heidelberg Engineering, Germany) OCT scans having only sparse annotations, i.e., 3–5 B-scans per volume were manually annotated, representing an equivalent of approximately 20 fully annotated OCT volumes. Unfortunately, the accuracy of the fluid segmentation performance has not been reported.

Another notable work is that of Lee et al. (2018), where they trained and evaluated a U-net for segmentation of IRF, SRF, SHRM and PED on 930 B-scans from 93 eyes of 93 patients with nAMD. Using data augmentation during training, where training examples are artificially deformed to increase the image appearance and shape variability, their CNN was trained using 11,550 augmented images derived from 550 B-scans. They reported high DSC scores of 0.78, 0.82, 0.75, and 0.80 for segmentation of IRF, SRF, SHRM, and PED. Lu et al. (2019) presented the winning solution of the RETOUCH challenge that performed both fluid segmentation and detection. The system was trained for each device manufacturer separately and relied on a combination of a U-net CNN as well as traditional random forest classifiers and graph-cut segmentation algorithms to detect and reject false-positive fluid voxels. This approach reached a segmentation performance of DSC = 0.77 and a perfect detection performance (AUC = 1). Recently, Guo et al. (2020) adapted the U-net to increase its capability for multiscale segmentation of retinal fluid in eyes with DME in OCT volumes. The U-net was trained and evaluated on data from 51 participants (45 with DME and 6 healthy controls) and obtained a DSC = 0.864 in segmenting retinal fluid, although without the ability to distinguish between IRF and SRF. The performance could be further improved to a DSC = 0.892 by including information from both OCT angiography (OCTA) and structural OCT,

which are acquired simultaneously by modern OCTA devices.

Supervised learning relies on an ample availability of pairs of OCT images and their corresponding pixel labels, requiring large, manually annotated datasets, which is slow and expensive. Furthermore, there is a lack of standardized scanning protocols in routine OCT imaging and each device manufacturer uses its own post-processing, resulting in volumetric OCT scans which strongly differ in image resolution and signal-to-noise ratios (Yanagihara et al., 2020). Thus, a model trained on images from one OCT device manufacturer may not readily generalize to images of another OCT device or even to a newer OCT device model from the same manufacturer. This challenge means training examples have to be obtained for each individual target OCT device. Producing such dense annotations is tedious and time-consuming. Collaboration and data-sharing between multiple institutions is often necessary to reach the data amount and quality necessary for achieving clinically applicable performance. As such exchange may lead to issues that concern data privacy and security, which in the real world often hinders sharing between institutions, Mehta et al. (2020b) demonstrated a proof-of-concept of a so-called *model-to-data approach*. The investigators at the sites trained an AI model from images coming from multiple institutions, with the model rather than the data traveling between them. There, a U-net for IRF segmentation was iteratively improved by training with the data available at each institution using a total of 400 OCT B-scans from 128 participants.

### 2.3. OCT segmentation with weakly supervised or unsupervised learning

A supervised learning approach for semantic segmentation requires pixel-wise annotations for training. As described above, such pixel-wise manual annotations are very expensive and time-consuming. Hence, two alternative learning schemes were pursued to respond to this demand: *Weakly supervised* and *unsupervised learning*. A weakly supervised segmentation technique aims at learning from a less costly OCT level or B-scan-level labels denoting fluid presence. This has been powerfully demonstrated by Schlegl et al. (2015) by using labels denoting an approximate spatial location of the fluid related to its retinal layer position and distance to the fovea. A performance equal to  $\approx 85\%$  of an equivalent pixel-level fully supervised model was reached. Other weakly supervised approaches exploit image interpretability techniques applied to the trained fluid detection network. Those can reveal the pixels that contribute to the decision making behind detecting the fluid, expecting that such identified pixels will be correlated with the pixels of the fluid regions. Several approaches showed that a pixel-level segmentation can be extracted in such a manner, albeit with moderate accuracy (Kermany et al., 2018; Lee et al., 2017a; Vidal et al., 2018).

Unsupervised learning approaches take this method one step further and are based around the concept of *anomaly detection*, which requires a training set of healthy retinas only, without any pixel-level or scan-level labels. A two-step process is used, where first the “normal” shape and appearance is learned, and then anomalies such as fluid can be detected as deviations from the norm. This reflects the traditional study process of medical students, who first learn what a healthy tissue looks like and subsequently gain the ability to recognize pathologies as deviating from this normal appearance. Seeböck et al. (2019b) trained a retinal layer segmentation on healthy images, and used a measure of segmentation uncertainty as a surrogate for local anomalies in the image. As an alternative, Schlegl et al. (2019, 2017) used generative adversarial networks (GANs) (Goodfellow et al., 2014) to synthesize a healthy version of the local image region, allowing the anomalies to be highlighted as the local difference between the diseased image patch and its synthetic healthy counterpart.

An alternative unsupervised learning approach is to use available, but unlabeled datasets, to improve the generalization capabilities of previously trained AI models. This is achieved by learning to perform image-to-image translation between scans acquired with different OCT device manufacturers. Such a proof-of-concept has recently been

demonstrated by Romo-Bucheli et al. (2020b), who used CycleGAN (Zhu et al., 2017) to produce synthetic but realistic OCT images that have the look-and-feel appearance of the target OCT device, while preserving the morphological retinal information of the original source OCT device. Thus, without any additional annotations, it is possible to extend the generalization performance of a pretrained fluid segmentation model.

#### 2.4. Detection of the presence or absence of fluid

Detecting the presence, recurrence and resolution with absence of fluid are basic tasks in the clinical management of macular disease, and these markers are often used for assessing substance efficacy in clinical trials. Having an accurate fluid segmentation method greatly facilitates such a basic fluid detection task, as detection of fluid presence or absence can be achieved either by thresholding the number of segmented fluid voxels or training another classifier to learn to detect fluid from the segmentation output. Schlegl et al. (2017) have conducted the largest evaluation of individual fluid detection to date. They evaluated automated segmentation against a volume-level manual grading of 1200 OCT volumes of eyes with nAMD (400), RVO (400) and DME (400) with an equal distribution of fluid presence and imaged with two different OCT devices, Cirrus (600) and Spectralis (600). AUCs for IRF and SRF ranged from 0.91 to 0.97 and 0.87–0.98, respectively. Chakravarthy et al. (2016) reported a diagnostic accuracy of overall fluid detection of 91% compared with the majority grading by three retinal specialists on 142 OCT scans (Zeiss Cirrus) of eyes with nAMD. Moraes et al. (2020) applied a previously published DeepMind algorithm using the Moorfields AMD clinical database. Two retinal specialists independently performed the binary classification task for IRF and SRF presence on a subset of 573 baseline scans. Evaluation of the cases with the expert agreement showed a detection performance of an AUC = 0.85 for IRF and an AUC = 0.95 for SRF.

Even when fluid segmentation is not available, CNNs are well suited for such a binary image classification task to detect whether fluid is present in the scan. In fact, research in deep learning has produced several powerful CNN models for image classification. The image classification setting has vastly benefitted from research efforts in the domain of visual recognition challenges such as the ImageNet (Russakovsky et al., 2015) containing millions of annotated images. This resulted in the availability of a few ready-made, pre-trained image classification CNN architectures which can be fine-tuned on an OCT fluid detection task. Such a *transfer learning* approach used by Treder et al. (2018) successfully detected nAMD from a central OCT B-scan by fine-tuning with 1012 OCT B-scans. An accuracy of 0.98 was achieved on a test set of 100 B-scans, equally balanced between nAMD and healthy examples. Lee et al. (2017a) proposed a CNN trained from scratch on more than 100,000 B-scans to distinguish nAMD B-scans from normal scans, relying on a popular VGG16 (Simonyan and Zisserman, 2014) network architecture. A total of 80,839 B-scans (41,074 from AMD, 39,765 from normal eyes) were used for training, and 20,163 B-scans (11,616 from AMD, 8547 from normal eyes) were used for validation. At the B-scan level, the approach achieved an AUC of 92.78% with an accuracy of 87.63%. At the macular OCT-scan level, the method achieved an AUC of 93.83% with an accuracy of 88.98%. Kurmann et al. (Kurmann et al., 2019) fine-tuned a popular ResNet CNN architecture (He et al., 2016) to detect a series of biomarkers on each B-scan of a volumetric OCT. After training on 23,030 B-scans from 327 patients, the investigators compared the performance on 1029 B-scans from 21 patients with a majority voting decision of eight experts. The CNN showed a high accuracy in the detection of fluid with an AUC of 0.98.

Overall, there are many approaches available and published in recent literature that can apply AI modalities to automatically identify the occurrence of fluid in retinal OCT scans. These could serve as major instruments for recognition and screening of retinal diseases not only by general ophthalmologists but also by eye-care and other professionals working at locations, such as the general practitioner's office or the

pharmacy, where large populations of individuals are at risk for exudative macular pathologies.

#### 2.5. Modeling of quantitative fluid development

The mere detection of fluid in the retinal space, similar to a clinician's qualitative discretion about fluid presence or absence, is not enough to import precision medicine into the retinal experts' decision making in high-quality and high-volume disease management. The unique paradigm shift which AI offers to real-world practice is its automated and objective quantification of fluid in different compartments, and at any visit for individuals as well as for large populations.

In macular edema, regular treatment with anti-VEGF agents restores and preserves vision by reducing fluid accumulations in the NSR. The necessity of periodic anti-VEGF treatment and corresponding monitoring with visual acuity scores and retinal OCT scans provide extensive and exceptional longitudinal datasets. In contrast to cross-sectional studies, where only a snapshot at a given point is analyzed, a longitudinal setting allows quantification off changes over time, and subsequently assessment of disease progression and treatment response. Here, changes in function and pathoanatomy under treatment are captured by in-vivo measurement of distinct fluid volumes in OCT scans and visual function in terms of BCVA. A proper analysis of these measurements allows assessment of a reliable association of structure (fluid) and function (BCVA) by correlating the changes in vision and fluid in disease progression and under treatment. In particular, distinguishing different fluid types, such as IRF, SRF and PED, and further integration of the spatial location of fluid with respect to the fovea, facilitates the evaluation of the differential impact of different fluid compartments on central vision. As a target of anti-VEGF treatment is the reduction of retinal fluid with optimal visual recovery, assessing fluid volumes by compartments may allow a precise determination of clinically relevant variables and an estimation of individual treatment outcome (Vogl et al., 2017). The variable of interest for the future in AI-based treatment decisions will not simply be the presence or absence of fluid, but rather a compartmentalized assessment of fluid.

Modeling longitudinal BCVA development under treatment and the effect of fluid compartmentalization is a challenging task. As highlighted in Fig. 11, we observed a high variance in BCVA at baseline visits, resulting a priori from different disease stages at the first visit and variance in the individual trajectories due to differing responses to treatment or different treatment regimens. The model also has to consider the rapid change in fluid reduction and major BCVA gain after the first treatment, and the losses in BCVA due to a recurrence of fluid as a result of a specific treatment regime, pro-re-nata (PRN) and T&E. The model should also be able to handle irregular visiting intervals, missing visits and drop-outs of patients, as these are common issues in longitudinal medical datasets. Linear mixed models (LMMs) are a powerful statistical tool capable of addressing these issues in longitudinal data. This statistics framework has been successfully applied in the medical imaging domain of neurodegenerative disorders (i.e. Alzheimers disease) (Bernal-Rusiel et al., 2013; Bilgel et al., 2016; Schiratti, 2017). Extensions of LMMs, such as joint models combining LMMs with time-to-event data (Proust-Lima et al., 2014; Rizopoulos et al., 2016), Bayesian inference (Fong et al., 2010) or with Gaussian processes (Lorenzi et al., 2017) increase the flexibility of the models and widen the scope of applications. LMMs have been successfully applied in retinal diseases to analyze structure-function in AMD, DME, and RVO from longitudinal data (Reiter et al., 2020a; Roberts et al., 2020; Schmidt-Erfurth et al., 2020b; Vogl et al., 2017). Details of the outcomes of these structure/function analyses are discussed in Chapter 4. Here, the focus is on the underlying method, in particular in the context of fluid-function correlation.

##### 2.5.1. Linear mixed models for longitudinal data

LMMs for longitudinal data (Verbeke and Molenberghs, 2009) are

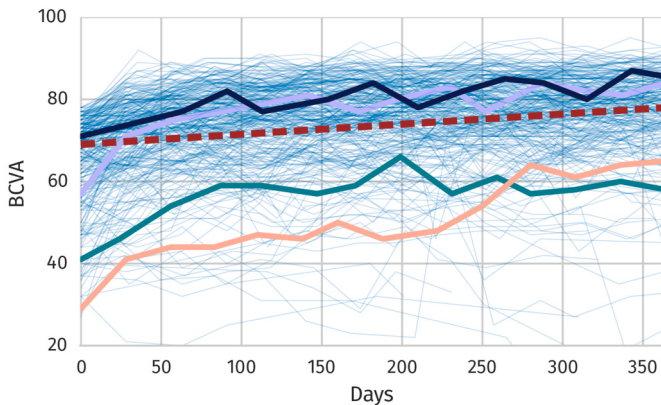


**Fig. 10.** Best-corrected visual acuity (BCVA) development in a cohort of patients with diabetic macular edema receiving anti-vascular endothelial growth factor treatment. Each blue line is the BCVA trajectory of an individual patient. Four cases are exemplarily highlighted, demonstrating the variance in the data due to the specific disease stage. (For interpretation of the references to color in this figure legend, the reader is referred to the Web version of this article.)

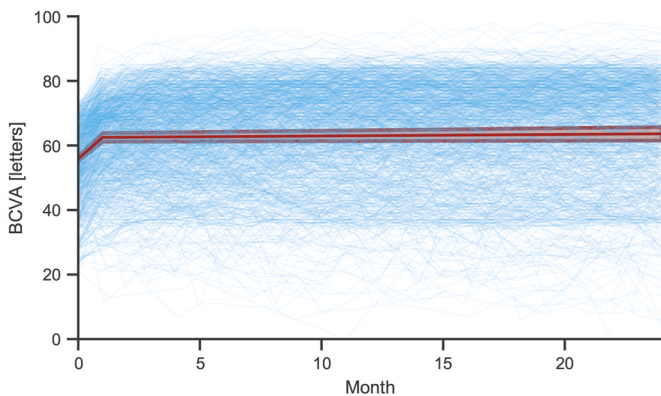


**Fig. 11.** Modeling best-corrected visual acuity (BCVA) trajectories in an age-related macular degeneration cohort as a split-linear model to capture rapid changes after the first treatment. The red line indicates the mean trajectory defined by fixed effects. (For interpretation of the references to color in this figure legend, the reader is referred to the Web version of this article.)

able to describe longitudinal trajectories, both on a population and individual level. Such models contain *fixed effects* and *random effects*. Fixed effects may be interpreted as population-wide mean effects, similar to coefficients in basic linear regression. Random effects are defined for a group and subsume factors that are not covered by fixed effects and/or cannot be assessed. In the case of longitudinal treatment data, we assume a grouping effect of follow-up measurements per patient and/or eye, as data points within a patient are not independent, and have a different variance structure than between patients. This is evident for instance in the BCVA trajectories, where the variance between different patients is higher than between follow-up scans of a patient (Fig. 10).

For modeling BCVA trajectories, the growth curve model of Laird and Ware (1982), which is a common realization for LMMs for longitudinal data, can be applied. In its most simple form, such a model has an intercept and a slope as fixed factors describing the mean value at baseline (intercept) and mean trend (slope) in BCVA development (Fig. 10 dotted red line). By including a random intercept and random slope per patient, we account for subject-specific deviation from the population-wide BCVA trajectory due to disease stage and speed of recovery. Formally, assuming we have  $i = 1, 2, \dots, n$  patients and for each patient  $j = 1, 2, \dots, m_i$  observations, such a model is defined for a single patient  $i$  and observation  $j$  as:

$$y_{ij} = \underbrace{\beta_0 + \beta_1 t_{ij}}_{\text{fixed}} + \underbrace{b_{0i} + b_{1i} t_{ij}}_{\text{random}} + \varepsilon_{ij} \quad (2)$$

$y_{ij}$  is the outcome variable, such as a BCVA measurement, measured at time-point  $t_{ij}$ .  $\beta_0$  and  $\beta_1$  are the intercept and slope of the mean trajectory.  $b_{0i}$  and  $b_{1i}$  are subject specific deviation from the general trajectory in terms of the random intercept and slope, respectively. The residuals  $\varepsilon_{ij}$  and random effects are assumed to be independent from each other and normally distributed. The coefficients  $\beta$  and (co-)variances are usually estimated from the data using maximum likelihood, restricted maximum likelihood (Bates et al., 2015) or Bayesian approaches (Fong et al., 2010). Additional fixed effects may be added similarly as in linear regression to estimate additional effects associated with the outcome, such as a different treatment regimen, age or sex.

A main advantage of LMMs compared with traditional statistical methods, as for instance analysis of variance (ANOVA) for repeated measures, is that the number and interval of observations is flexible, which makes it more suitable for analysis of non-RCT real-world datasets. Furthermore, a model can be extended easily to include additional hierarchies, for instance repeated observations for patients within subgroups. Furthermore, generalized and non-linear mixed models allow us to analyze non-normal data (e.g. categorical data) or more complex trajectories (Fong et al., 2010).

Roberts et al. (2020) and Reiter et al. (2020a) used a piecewise linear model with the split point after the first treatment. This approach allows the capture in particular of the rapid changes in BCVA that occurred after the first treatment more accurately than in a simple linear model. Fig. 11 shows such a mean trajectory in an AMD cohort. Roberts et al. (2020) used this model to assess the mean change of BCVA, IRF and SRF in patients with DME after the first injection and subsequently. Furthermore, by incorporating a categorical covariate encoding the administered drug (afibercept, bevacizumab, ranibizumab), the investigators were able to show that afibercept induces a significantly stronger reduction in fluid than bevacizumab.

### 2.5.2. Correlating structure/function in a longitudinal setting

As observed in Fig. 12, there is a correlation between central vision and the presence/absence of fluid volumes. This correlation can be modeled by adding fluid as a covariate to the model. Furthermore, by including fluid volumes at different retinal locations (i.e. IRF vs. SRF vs. PED, foveal vs. parafoveal), the differential association of these fluid types and locations with visual acuity can be determined. Vogl et al. (2017) and Roberts et al. (Roberts et al., 2020) included the accumulated IRF and SRF volume measures within a 1-mm diameter around fovea and within the parafovea, i.e., the 1- to 3-mm ring around fovea. Eq. (2) is then extended in the following way by fluid volumes measures  $v_{ij}^{fov-irf}$ ,  $v_{ij}^{fov-srf}$ ,  $v_{ij}^{para-irf}$ ,  $v_{ij}^{para-srf}$  that correspond to IRF and SRF volume at the fovea and para-fovea, respectively:

$$\begin{aligned} bcva_{ij} = & \beta_0 + \beta_1 \times t_{ij} + \beta_2 \times v_{ij}^{fov-irf} + \beta_3 \times v_{ij}^{fov-srf} + \beta_4 \times v_{ij}^{para-irf} + \beta_5 \\ & \times v_{ij}^{para-srf} + b_{0i} + b_{1i} \times t_{ij} + \varepsilon_{ij} \end{aligned} \quad (3)$$

The coefficients  $\beta_0$  and  $\beta_1$  are the mean intercept and slope, and  $b_{0i}$  and  $b_{1i}$  the subject specific intercept and slope deviations.  $\beta_2$  to  $\beta_5$  are interpreted as the effect that a particular fluid volume compartment has on average on BCVA per unit.

Examples of measures and individual model fit from fixed and random effects estimates for RVO, DME and AMD (Fig. 13) illustrate that the general trend in BCVA development under treatment is well captured by the model. The association of fluid and BCVA is particularly evident with a BCVA drop and recovery due to fluid recurrence and subsequent anti-VEGF treatment. This also demonstrates the benefit of using longitudinal data rather than cross-sectional data. The patient-specific variation in the trajectory due to individual disease stage and speed of disease progression can be separated from fluid effects by

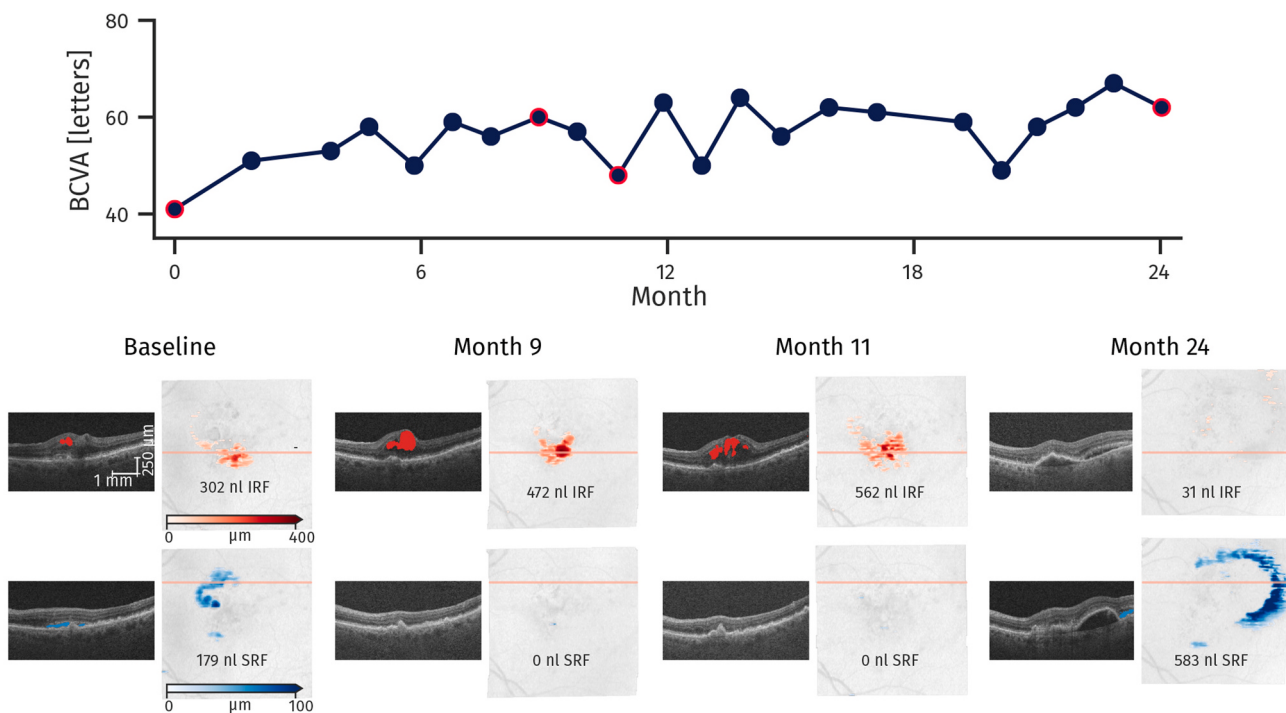


**Fig. 12.** Individual best-corrected visual acuity (BCVA) trajectory of a patient with neovascular age-related macular degeneration (nAMD) receiving anti-vascular endothelial growth factor treatment. For four time points (baseline, months 9, 11, 24) the corresponding intraretinal fluid (IRF) and subretinal fluid (SRF) segmentations are shown. The numbers represent the fluid volumes measured in the whole volumes. Note that at month 11 the letter score decreases and at the same time central IRF is observed, indicating a clear association of fluid and visual function.

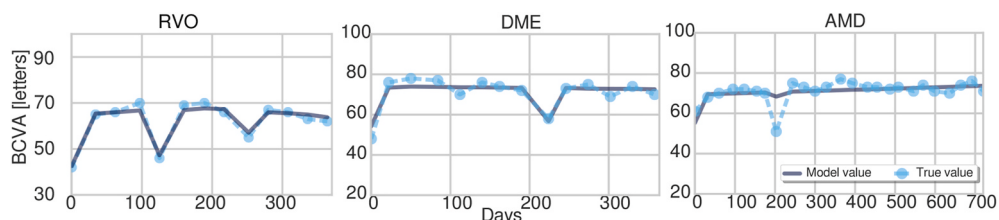


**Fig. 13.** Measured (light blue) and linear mixed model predictions (dark blue) of individual trajectories for the three diseases diabetic macular edema (DME), age-related macular degeneration (AMD) and retinal vein occlusion (RVO). Correlations of fluid and function are visible as spikes in the trajectory due to recurring fluid. (For interpretation of the references to color in this figure legend, the reader is referred to the Web version of this article.)

including a patient-specific random intercept and slope that are estimated from all available data points. Furthermore, as shown by Vogl et al. (2017), the model can also be used for individual prediction. Considering the fluid effect, estimating patient-specific random outcomes from initially observed time points were used to compute a trajectory based on Eq. (3) and to extrapolate it in order to estimate treatment outcome in terms of BCVA after one year.

There are limitations to the model described. First, a *linear* model is used to capture the trajectory. Whereas it is capable of capturing the general trend of the mean and individual trajectories, a more accurate model fit might be obtained by a polynomial or non-linear model fit. The split-linear model was introduced particularly for the purpose of capturing large changes in BCVA and fluid after the very first injection. However, especially in DME, fluid resolution is slower than in AMD and may be captured better by a non-linear method. Second, the relation of structure and function is also assumed to be linear in the model. Whereas this allows for an easy interpretation of the coefficients, a non-linear relation might provide a more precise estimate of the effect of fluid on function. Third, fluid volume is associated with BCVA at the same visit only in the model described. However, permanent damage to neurosensory structures caused by the presence of fluid resulting in reduced

vision, even after fully resolved fluid, is not covered by these coefficients. These changes are then subsumed in random effects, causing a drop in the slope, but not in the association of fluid/function. Furthermore, baseline fluid is not distinguished from fluid recurrence at later time points in the model. Fluid at baseline may be present for a longer period in the retina, and may have different effects on neurosensory structures than transient fluid recurrence followed by an anti-VEGF treatment regimen. As Riedl et al. showed in an AMD cohort, baseline foveal and parafoveal IRF is negatively associated with BCVA by  $-3.2$  and  $-1.1$  letters per 100 nl fluid volume, respectively, whereas at later time points only foveal IRF has a negative association of  $-4.3$  letters per 100 nl. A larger volume of fluid at baseline may be an indicator of more severe or longer untreated disease, which may be associated with a gradual loss of vision, whereas at later time points the association of fluid and function is more immediate, as indicated by the influence of foveal IRF on central vision. Finally, morphological changes, such as photoreceptor alterations, SHRM, atrophic and fibrotic changes were not specifically accounted for in the model. This can be observed for instance in the AMD case in Fig. 13, where a drop in vision occurred due to non-fluid-related alterations in the retina. However, the model can be easily extended by including other quantitative markers that affect

vision as additional covariates.

As shown in this section, LMMs are a powerful tool for analyzing the fluid-related treatment response in a longitudinal setting, and reliably quantify the association of fluid in the retina and resulting function, particularly in respect to different compartments. This opportunity based on a precise localization and quantification of fluid using AI-based tools is crucial in advancing our understanding of the pathomechanisms of exudative disease entities and identifying the clinically relevant targets for therapeutic intervention.

### 3. AI-based assessment of treatment response in anti-VEGF therapy

After the discovery of the cause-effect relation of VEGF, the first anti-VEGF substances, pegaptanib sodium and ranibizumab, were developed for ocular purposes in the early 2000s with the treatment of nAMD as the primary target (Lanzetta et al., 2013; Rosenfeld et al., 2006). In the meantime, the anti-VEGF agent bevacizumab was approved for the treatment of metastatic colon cancer, which led to a widely established off-label use in ophthalmology, which is still ongoing to this day. Initial attempts of intravenous administration of anti-VEGF were quickly discontinued due to side effects and intravitreal application of anti-VEGF was established as the primary route of administration (Campochiaro and Akhlagi, 2020). Beside the introduction of anti-VEGF therapy for nAMD, the same substances were also investigated and later approved to tackle other mainly, but not exclusively, VEGF-mediated retinal vascular diseases, especially DME and macular edema due to RVO (Lanzetta and Loewenstein, 2017). Monthly treatment was soon considered a large burden for patients and physicians, and novel treatment regimen strategies arose from the necessity to individually address a patient's need for re-treatment based on leakage activity. Further, the development of substances with extended durability or higher dosages were initiated. A second approach to tackle this issue is to investigate refillable drug delivery systems, which is ongoing.

As an essential base for deciding which treatment regimen/agent/system is superior in sustaining patients' visual function, a precise assessment of the therapeutic efficacy has to be performed and the resulting evidence analyzed. This is the primary task for AI methodology in the retina: To understand the mechanisms and realistic benefits of all available treatment modalities, to screen through all available conventional study data and to extract the ground truth for a sound orientation regarding the optimal use of current therapeutic tools.

#### 3.1. Impact of the chosen regimen on fluid volumes

Fluid is assessed at different time points in different treatment regimens, therefore leading to different results. Monthly treatments are associated with monthly visits and result in maximum treatment with overtreatment in a proportion of patients, and possibly an enhanced risk of complications. In a PRN or "as-needed" regimen, the patient is monitored, ideally monthly, for as long as disease activity is present, mostly life-long in a chronic progressive pathology such as nAMD. This regimen allows for less injections with a greater follow-up burden. Its large disadvantage lies in the amount of visits per patient, which makes this regimen time-consuming for patients and treating physicians (Lanzetta et al., 2013; Mitchell et al., 2011). Also, the lower number of injections has been identified as one of the most important factors of sub-optimal visual outcome. In a pro-active treatment (i.e. T&E), the treatment interval is individually adjusted based on the exudative activity cycle to identify the longest treatment interval before the recurrence of fluid. Therefore, the patient typically receives more treatments, even if no macular fluid and disease activity is present, but undergoes less monitoring (Campochiaro and Akhlagi, 2020; Freund et al., 2015).

It is important to consider the treating regimen when assessing and quantifying fluid under therapy. In a PRN regimen, macular fluid volumes will be higher at the time of treatment and fluid assessment can

additionally be performed at non-treatment visits. In a T&E regimen, where the retina is proactively treated, fluid might not be present at the time of treatment and visit intervals can vary considerably between patients. Irregular visits make it more difficult to calculate means for specific time points due to the fact that patients will never offer standardized intervals and identical time points throughout the population. In conclusion, the treatment regimen will greatly impact fluid measurements and PRN assessments might be more stable and present with higher volumes compared with the pro-active T&E regimen, where fluid volumes will always be minimal making fluid/function correlations more difficult.

#### 3.2. Central retinal thickness vs. fluid volumes

Assessment of OCT-based CRT as a quantitative measurement has been widely used as a surrogate of disease activity in addition to traditional BCVA testing in large RCTs. This tradition was likely an extrapolation from the earlier time domain TD-OCT, with only 6 radial B-scans not allowing volume measurements but offering a center point thickness (CPT) as the only semi-quantitative variable, used in the major trials such as PRONTO, CATT and IVAN (Lalwani et al., 2009; Martin et al., 2012; Chakravarthy et al., 2012). There are, however, critical issues with substituting exudative disease activity measurements with CRT alone. Commercial algorithms often fail to correctly delineate the ILM when there is intensive cystoid alteration of the inner retinal layers and different OCT devices use different boundaries for CRT determination (Mylonas et al., 2009). CRT is not always clearly defined and the measurement can alternatively include the distance from the ILM to the external boundary of the NSR versus the distance from the ILM to the RPE in eyes associated with SRF and SHRM (Moraes et al., 2020) versus the distance from the ILM to BM in eyes associated with fibrovascular PED, which are all different pathomorphological entities (Chakravarthy et al., 2021; Dugel et al., 2020a). In macular edema, it may be difficult for investigators to determine the foveal center, leading to incorrect CRT values (Toth et al., 2015). The major drawback of CRT or CST is their partial representation of an in reality three-dimensional fluid distribution, although a more accurate calculation is easily accessible with modern raster-scanning high-resolution OCT technology (Schmidt-Erfurth et al., 2017b; Schmidt-Erfurth and Waldstein, 2016).

The correlation between CRT and pathological fluid volumes was assessed at baseline and during the maintenance period in a large pooled dataset including nearly 2200 patients affected by the three major exudative diseases (1097 nAMD; 588 DME, 512 RVO). Most intriguingly, the correlation between SRF/IRF and CRT was the weakest in nAMD, with overall low to moderate correlations at baseline depending on the correlation based on either SRF, IRF or both (Pawloff et al., 2021). During follow-up, this correlation remained low for nAMD, indicating that CRT is not an appropriate variable for determining fluid and leakage activity at initial presentation, or for guiding retreatment. In DME, the baseline correlation between SRF or IRF and CRT was the highest among the three diseases, but still only achieved a moderate correlation. The combination of SRF and IRF with their direct association to the fovea led to a moderate association with CRT at baseline and follow-up. In RVO, baseline associations were also moderate, however, IRF and IRF/SRF combined showed a high correlation with CRT during follow-up, indicating that CRT is an effective marker for disease activity (Pawloff et al., 2021). IRF is the main driving force of a fluid/CRT correlation in the fovea. Therefore, pathognomonic differences between the diseases define the role of CRT/CST. Localization of fluid in an en face map showed characteristic correlations/co-localizations in nAMD (Klimscha et al., 2017). In nAMD, fluid does not only accumulate in the central mm but may extend far beyond, such that it is not captured by CRT determination alone. A retrospective cross-sectional study of 1182 OCT volumes ( $6 \times 6$  mm) from 1341 patients with treatment-naïve nAMD yielded more than 61 million A-scans for analysis. IRC, SRF and PED were detected on a per-voxel basis using fully automated

segmentation algorithms. Two subsets of 37 vol each were manually segmented to validate the automated results for ground truth performance. Overall, 81% of eyes showed IRC, 95% SRF and 92% PED. IRC-presenting A-scans also showed SRF in 2.5% and PED in 32.9%. Of the SRF-presenting A-scan locations, only 0.3% simultaneously demonstrated IRC and 1.4% PED. Vice-versa, of the PED-presenting A-scans, only 5.2% contained IRC and 2.0% SRF. Identical patterns were observed in the manually segmented subsets and via pixel-wise odds ratio analysis. In conclusion, nAMD demonstrated low spatial correlation of SRF with IRC and PED, in contrast to increased

co-localization of IRC and PED. These morphological associations may contribute to our understanding of patterns of progression and functional deficits in nAMD (Fig. 14) (Klimscha et al., 2017). The reasons for these pronounced differences are based on the topographic distribution and compartmentalization of fluid, which will be individually demonstrated for each disease in the following.

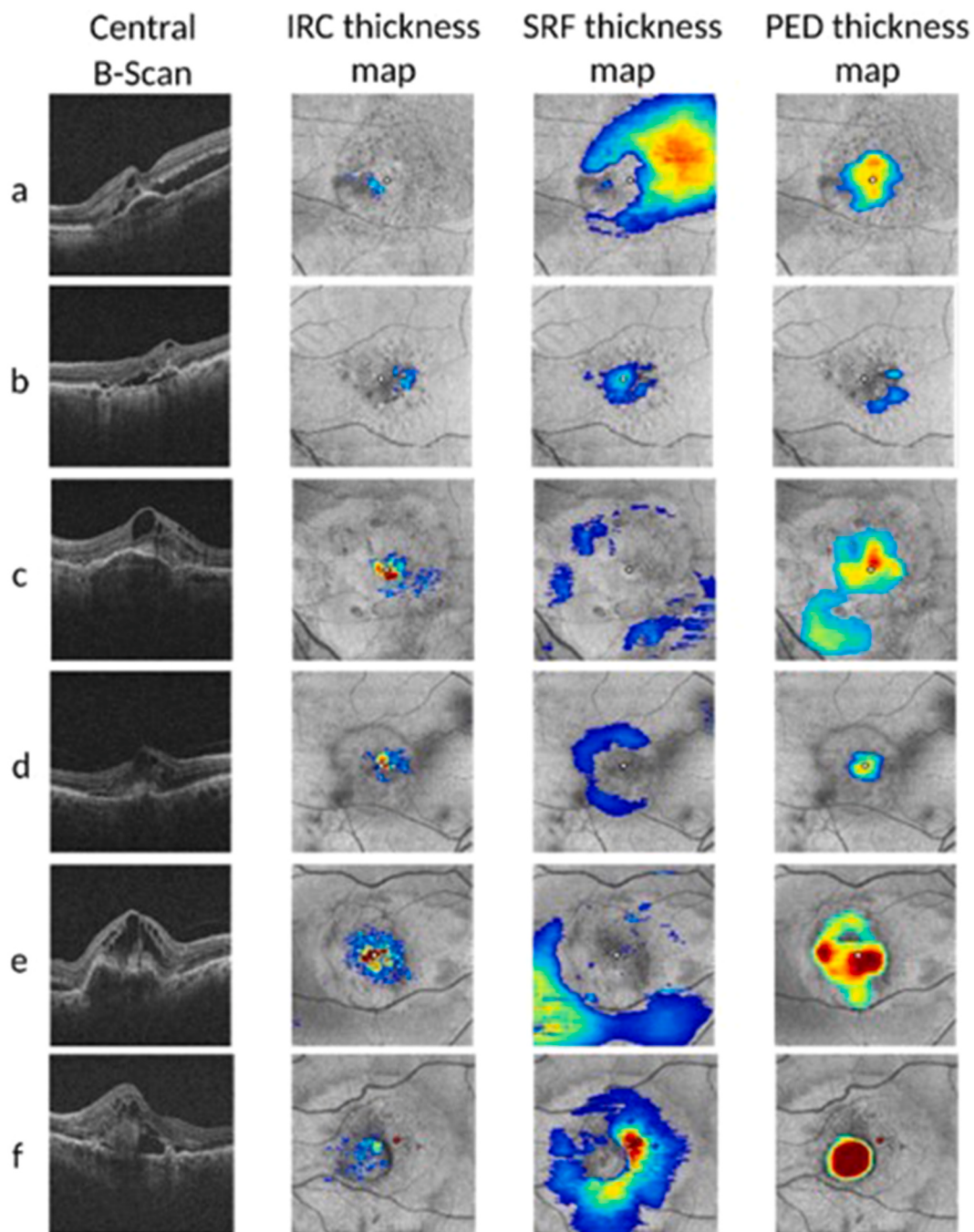


**FIG. 5.** Central B-scan and corresponding IRC-, SRF-, and PED-en face thickness maps of automatically (a–e) and manually (f) segmented example cases. Note how IRC mainly colocalize to PED lesions, whereas SRF is mainly localized in retinal locations outside PED- and IRC-affected areas.

**Fig. 14.** Central B-scan and corresponding intraretinal fluid- (IRC-), subretinal fluid (SRF-), and pigment epithelial detachment- (PED-) en face thickness maps of automatically (a–e) and manually (f) segmented example cases. Note how IRC mainly colocalize to PED lesions, whereas SRF is mainly localized in retinal locations outside PED- and IRC-affected areas (reproduced from (Klimscha et al., 2017)).

### 3.3. Measurement of fluid resolution in nAMD

#### 3.3.1. Therapeutic response measured by manual annotations

Detection of an incomplete response to therapy is crucial during anti-VEGF therapy in AMD, as this will severely affect treatment outcomes. An incomplete response was previously defined as 1) persistent macular fluid, 2) new or unresolved hemorrhage, 3) progressive fibrosis and scarring and 4) suboptimal visual outcome (Mettu et al., 2020). But before analyzing (persistent) fluid in AMD, one must also be aware of the topographic distribution of different fluid compartments associated with exudation. The amount of fluid is not evenly distributed across the macular region. IRF is abundantly present in the foveal center, whereas SRF is present in only small amounts in the fovea. The major component of SRF volume is located outside the foveal center and might extend over the entire macular region sparing the fovea (Klimscha et al., 2017).

Early work using manual quantification of macular fluid for a small number of eyes showed SRF and IRF responded immediately after initial ranibizumab treatment. SRF especially resolved, mostly during the first week after initial treatment, and achieved almost complete resolution after one month. Subretinal PED volume exhibited a delayed response, but continuously decreased with further treatment of the loading dose (Ahlers et al., 2008). A manual OCT quantification ancillary to the EXCITE trial investigated the impact of monthly compared with quarterly administered ranibizumab (Golbaz et al., 2011; Schmidt-Erfurth et al., 2011). Most distinctively, SRF volumes decreased in both treatment arms, however, SRF was noticeably lower in the monthly treatment arm, demonstrating the need to precisely quantify treatment response in an objective and reliable manner (Golbaz et al., 2011). Subretinal PED volume was also considerably smaller with monthly treatment, but did not resolve completely. Quarterly ranibizumab not only showed overall higher PED volumes but also exhibited higher rates of fluctuations in all fluid compartments, which might have an additional negative effect on VA outcomes (Evans et al., 2020). Keane et al. presented similar findings of macular fluid with manual segmentation

during ranibizumab and bevacizumab therapy. IRF as a distinct marker was not used but the volume of the NSR served as a substitute (Keane et al., 2012, 2008).

Human graders achieved this manual work by exhausting segmentation of macular fluid, which required up to 15 h per OCT volume (Waldstein et al., 2016a). In addition, only small numbers of patients could be assessed using manual segmentation, and considerable differences between readers and physicians were identified (Toth et al., 2015), weakening the initial advantage of expert manual fluid assessments. Undoubtedly, a paradigm change was urgently needed for the assessment of macular fluid, not only for the identification of macular fluid in general, but also for differentiation of individual fluid compartments. OCT has already been established as the primary diagnostic tool in retina outpatient clinics. However, automation is necessary to expand research on macular fluid to large patient cohorts with frequent visits to harness the full potential of three-dimensional OCT volumes (Schmidt-Erfurth et al., 2017b). High-resolution capability of 5–8 μm, the clear depth of focus and the precision to detect extremely small volumes of fluid in nanoliters enables AI of OCT imaging to unveil subclinical fluid features to the physician. Precise quantifications using automated AI algorithms made analysis of macular fluid possible in a fast, reliable and objective manner. Therefore, re-investigations of previous studies were performed to obtain realistic insights into the mechanics of fluid under treatment.

#### 3.3.2. Automatic quantification of fluid resolution using artificial intelligence

An analysis of macular fluid volumes from 1095 patients was conducted in the HARBOR trial, which was a 24-month, phase III, randomized, multi-center study that evaluated the efficacy of ranibizumab with different dosages (0.5 and 2.0 mg) and different regimens (fixed monthly and PRN), (Schmidt-Erfurth et al., 2020b). Macular fluid was automatically identified, quantified and classified into SRF, IRF or PED using deep learning (Schlegl et al., 2018). Most distinctively, IRF

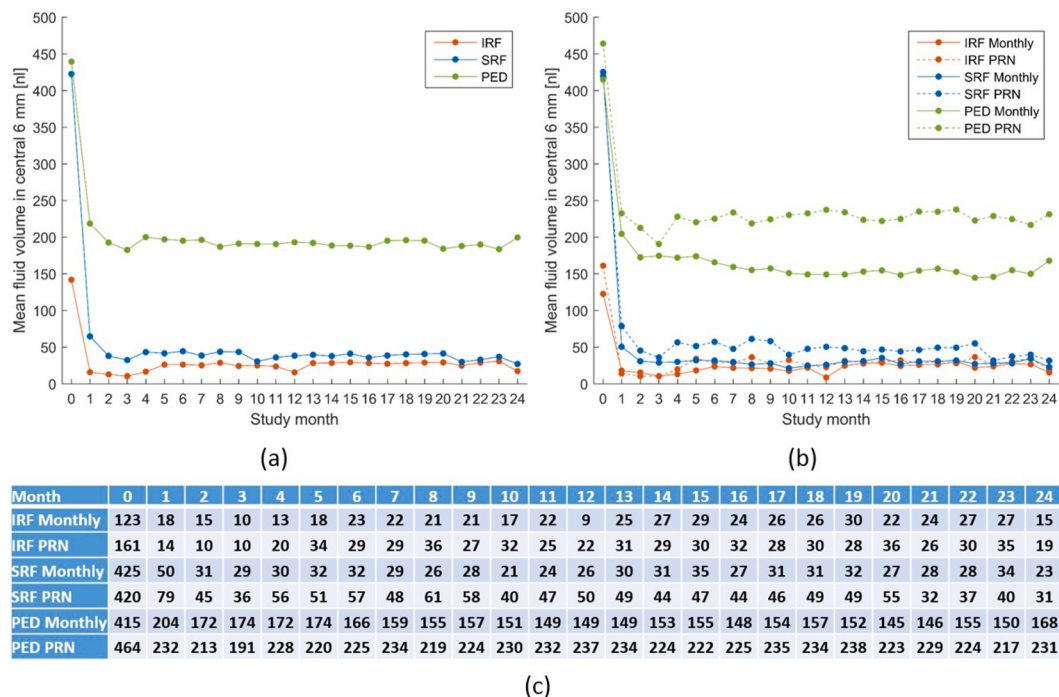


**Fig. 15.** Response pattern of different macular fluid compartments under anti-vascular endothelial growth factor (anti-VEGF) therapy in the HARBOR study. (a) pooled macular fluid compartments regardless of treatment intervals. (b) separated by treatment regimen. (c) numerical values in nanoliters (nl). Intraretinal fluid (IRF): Red; Subretinal fluid (SRF): Blue; Pigment epithelium detachment (PED): Green. Reprinted with permission from (Schmidt-Erfurth et al., 2020b) Application of automated quantification of fluid volumes to anti-VEGF therapy of neovascular age-related macular degeneration. *Ophthalmology* 127:1211–1219. (For interpretation of the references to color in this figure legend, the reader is referred to the Web version of this article.)

volumes dramatically decreased after the first injection and IRF volumes remained on a barely detectable level in both the monthly and PRN treatment arms (Fig. 15). A substantially larger volume of SRF also decreased significantly after the first injection, however, SRF persisted in higher volumes compared with IRF throughout the study. By contrast, subretinal PED decreased to about half of its baseline volume and resolution was dependent on the injection regimen. However, a complete response to the treatment could not be achieved, even with monthly interventions (Fig. 15). In conclusion, a dose and regimen effect was precisely quantifiable with deep learning when assessing macular fluid under anti-VEGF therapy. The strength of the HARBOR analyses was the monthly visits for both treatment regimens, which allowed a most reliable assessment of macular fluid and detection of characteristic resolution patterns (Schmidt-Erfurth et al., 2020b). Retinal fluid as the major hallmark of disease activity became measurable with nanoliter precision.

The FLUID study was a 24-month, phase IV, randomized multi-center study that investigated the clinical tolerance of SRF to a maximum height of 200  $\mu\text{m}$  at the foveal center in a T&E regimen. The primary goal was to investigate non-inferiority of visual acuity between a SRF-tolerant and SRF-intolerant treatment arm after 24 months. Re-treatment of anti-VEGF was based on a qualitative assessment

(presence or absence) of macular fluid. No difference in VA was identified at the end of the study, with the SRF-tolerant group receiving 1.2 injections less during the 24 months' follow-up. Therefore, the authors concluded that tolerating mild SRF (less than 200  $\mu\text{m}$ ) might be a practical path in a T&E regimen (Guymer et al., 2019). Interestingly, it became apparent in a subsequent quantitative analysis of the FLUID study, using the collected SD-OCT data, that the reduction of injections was in fact not associated with the expected higher volumes of (tolerated) SRF in the first place (Reiter et al., 2020a). On the contrary, quantified SRF volumes did not differ between the treatment arms. This was also true for IRF volumes, which was a treatment trigger in both treatment arms. No significant difference was again found between the treatment arms in the quantified assessment of absence of SRF (no detectable SRF volume). The conclusion is that qualitative assessment of macular fluid is insufficient, lacking the important volumetric dimension of assessment. It might therefore be more appropriate to assume that it was not essential to increase or decrease the number of injections by a mean of 1.2 over 24 months, but rather to precisely identify and quantify the treatment response before concluding on the impact of SRF. An ancillary analysis on structure-function correlation, in which fluid quantification was applied to the FLUID study data, is discussed in Chapter 4. Examples of quantifications in the FLUID study are shown in

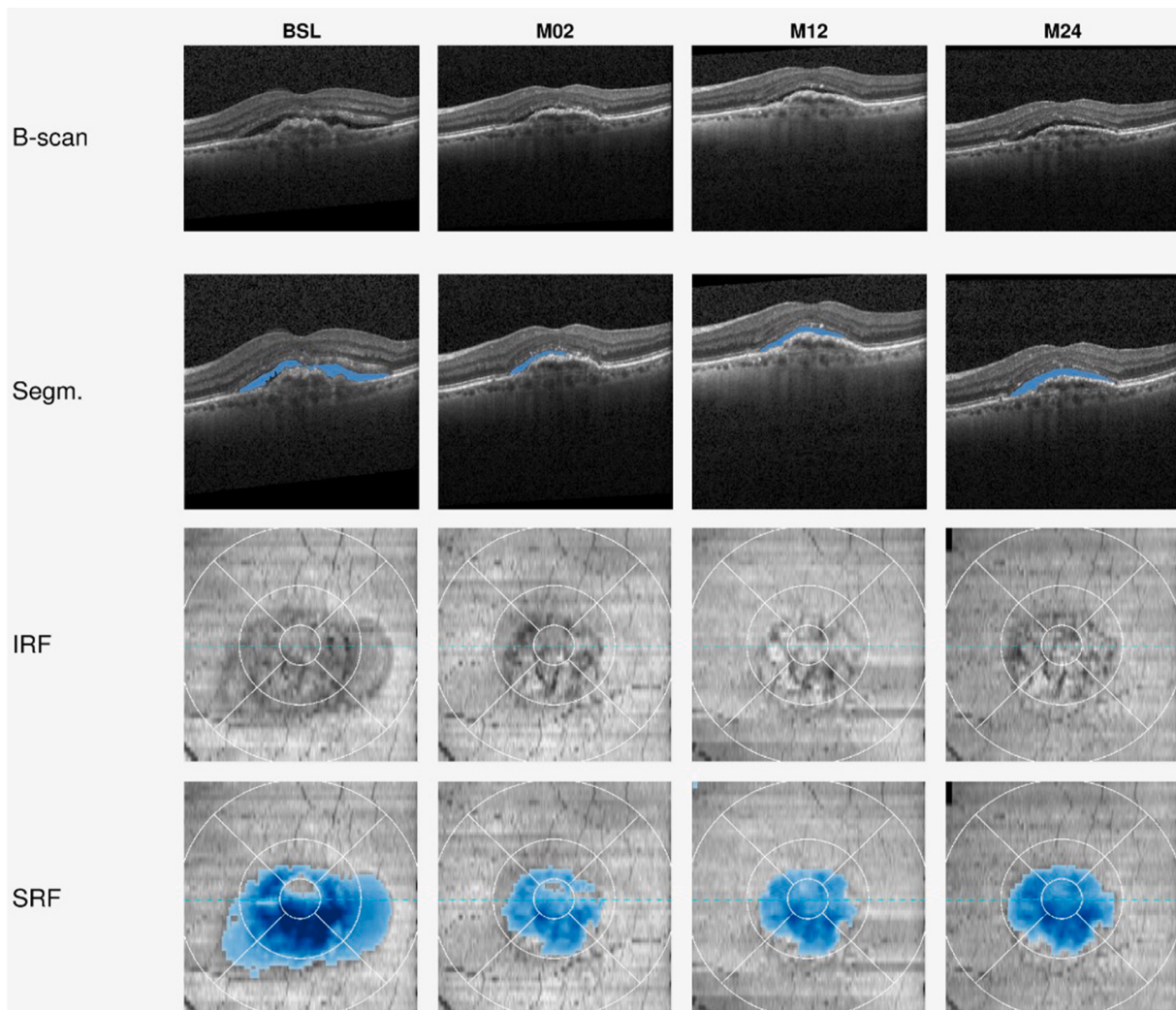


**Fig. 16.** Example of macular fluid quantifications under therapy of a patient randomized into the SRF-intolerant treatment arm of the FLUID study. Note: Subretinal fluid did not resolve under monthly therapy. The majority of subretinal fluid volume is located outside of the fovea. Subretinal fluid (SRF): Blue; Intraretinal fluid (IRF): Red. The B-Scan in the second row is the central B-Scan. The third and fourth row show en face maps of IRF and SRF, respectively. (For interpretation of the references to color in this figure legend, the reader is referred to the Web version of this article.)

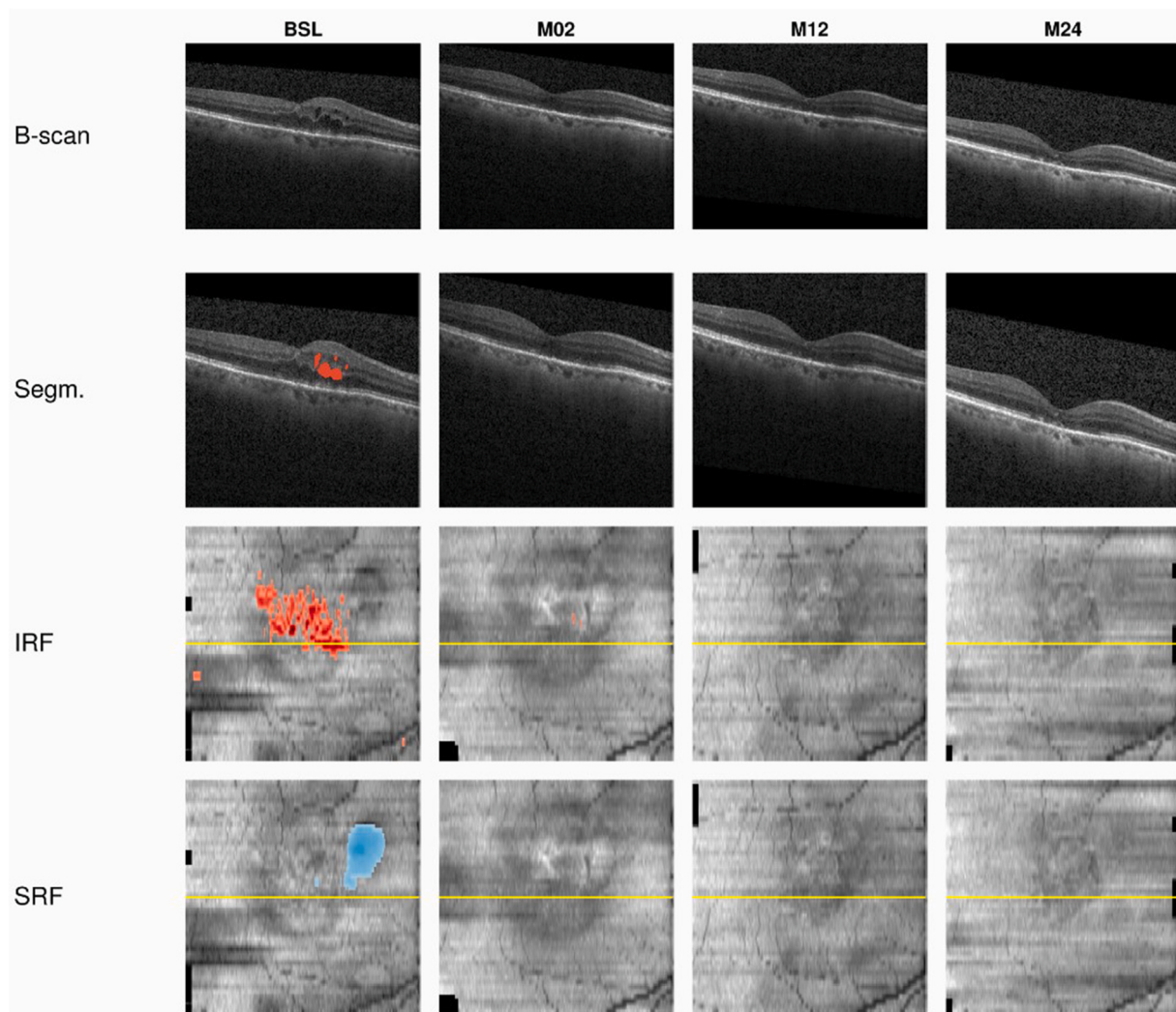


**Fig. 17.** Example of macular fluid quantifications under therapy of a patient randomized into the SRF-tolerant treatment arm of the FLUID study. Note: Subretinal and intraretinal fluid completely resolves after the first injection and the macula remains dry thereafter. Subretinal fluid (SRF): Blue; Intraretinal fluid (IRF): Red. The B-Scan in the second row is shown as a yellow line in row three and four. The third and fourth row show en face maps of IRF and SRF, respectively. (For interpretation of the references to color in this figure legend, the reader is referred to the Web version of this article.)

**Fig. 16** and **Fig. 17**. HAWK and HARRIER were phase III, two-year, multi-center randomized clinical trials that assessed the efficacy and safety of brolucizumab 6mg/3 mg against aflibercept 2 mg after a loading phase of three injections in each treatment arm. Aflibercept was administered bi-monthly, whereas brolucizumab was planned every 12 weeks with a possible bi-monthly rescue (Dugel et al., 2020b). The HAWK study included a 3-mg brolucizumab arm in addition to the 6-mg brolucizumab arm. OCT assessments were performed at every visit and automated detection and quantification of macular fluid volumes was performed subsequently (Schmidt-Erfurth et al., 2020a). Consistent with the characteristic anti-VEGF performance described, IRF was similarly and significantly decreased after the first injection in both the brolucizumab and aflibercept arm. IRF volumes remained at a very low level in both arms during follow-up. Total SRF volume was considerably greater than IRF volumes at baseline. Under brolucizumab treatment, SRF volumes decreased more than with aflibercept, i.e., between 74 and 97%, demonstrating a more intensive and stable reduction of SRF throughout the maintenance period. For PED volumes, fluid showed a larger decrease in the brolucizumab than aflibercept arm. PED volumes under brolucizumab therapy also remained more stable at a lower quantitative level. Moreover, lower levels of all types of macular fluid resulted in a better visual outcome than higher levels of any residual fluid, especially

IRF, but also SRF and PED (Schmidt-Erfurth et al., 2020a).

The same group also proposed and evaluated a machine learning methodology to predict anti-VEGF treatment needs from OCT scans taken during treatment initiation in the HARBOR trial (Romo-Bucheli et al., 2020a). In an AI-based fluid analyses of 317 patients, 71 presented low ( $\leq 5$ ), 176 medium, and 70 high ( $\geq 16$ ) injection requirements during PRN maintenance from month 3 to month 23. Classification of low and high treatment requirements demonstrated an AUC of 0.7 and 0.77, respectively. Interestingly, the most important feature for prediction was SRF in the central 3 mm, with the highest predictive values at month 2. This is easily explained by the slower resolution of SRF and the clinicians' instinctive reaction to retreat persistent SRF (Bogunovic et al., 2017). Use of AI analyses for predicting the prospective retreatment schedule offers a powerful management tool in large populations with active nAMD, saving manpower and economic efforts.

In conclusion, extensive research with numerous high-quality randomized clinical trials has been performed in AMD. The value of CRT as the most commonly applied morphological variable in large RCTs to date has to be questioned due to the lack of correlation with objective fluid volumes (Dugel et al., 2020b; Heier et al., 2012; Martin et al., 2011). Future approaches using AI-algorithms for the evaluation of anti-VEGF treatment response might be useful to predict a patient's need

of re-treatment. For this reason, patients with a high number of anti-VEGF re-treatments can be identified and given the adequate treatment and regimen. This will mitigate both over- and under-treatment, minimize individual risks of complications and optimize real-world treatment budgets (Bogunovic et al., 2017; Feng et al., 2020; Romo-Bucheli et al., 2020a). AI-based algorithms to precisely identify and quantify macular fluid in all different compartments and their longitudinal changes under treatment are therefore urgently needed to realize the full potential of high-resolution OCT imaging and better understand the real threat of macular fluid in AMD. Most relevant for an optimized fluid management is a precise assessment of fluid dynamics to distinguish stable from recurrent SRF and novel from persistent, i.e., degenerative, IRF, which is enabled by the accuracy of AI-based fluid measurement in nl.

### 3.4. Measurement of fluid resolution in diabetic macular edema

In contrast to nAMD, total quantitative fluid in DME is topographically highest in the foveal center. This applies to both IRF and SRF (Michl et al., 2020a). When looking at the parafoveal distribution of IRF, highest volumes can be found temporally, which overlaps with qualitative measures of leakage on FA and the area with advanced capillary drop-out (Haj Najeeb et al., 2017). AI tools can easily visualize the compartment and location of volumes separately.

Manual quantifications of fluid in DME showed resorption of both SRF and IRF under therapy. Interestingly, IRF in the INL did not decrease under therapy, in contrast to IRF in the outer plexiform layer (OPL) or ONL (Lee et al., 2019). However, baseline IRF volume in the INL was associated with the area of disorganization of retinal inner layers (DRIL) found later in the study, which per se might be an important subclinical factor for reduced visual function (Lee et al., 2019; Sun et al., 2014). These morphological details are relevant in the context of the characteristic pathophysiology of diabetic retinal disease described earlier. The INL compartment of fluid may represent either a degenerative or exudative pathway (Chen et al., 2015; Lenis et al., 2020), but is more likely degenerative in the absence of intraretinal fluid or cysts in the adjacent outer retinal layers.

The three most frequently used anti-VEGF agents (bevacizumab, ranibizumab and aflibercept) were compared for their efficacy in treating DME in protocol T from the DRCR Network (Wells et al., 2015). Using AI methods in a quantitative post hoc analysis, found that although IRF decreased significantly in all treatment arms, treatment response measured with quantitative fluid assessment showed a significantly higher decrease in IRF with aflibercept and ranibizumab than bevacizumab. After initial treatment, fluid volumes continuously decreased until month 12. No such agent-related difference was found for SRF. Visual acuity analyses in DME showed worse baseline VA was associated with SRF, however, a larger gain in VA was also associated with baseline SRF (Roberts et al., 2020).

VISTA-DME was a double masked, randomized, phase III trial that investigated the efficacy of monthly against every-other-month injections of 2 mg aflibercept after 5 initial monthly treatments. Similar to protocol T, both SRF and IRF were significantly reduced in both groups after 2 years of treatment. SRF was almost non-existent after treatment in both groups and IRF was interestingly further decreased in the every-other-month treatment group (Ehlers et al., 2019). Such pathognomonic patterns of fluid resolution highlight the differences in disease pathomechanisms between CNV and DME. In the future, algorithms guiding patient management in DME may also include systemic variables such as age, diabetes duration, blood pressure etc.

Although not based on macular fluid, but CRT, a deep learning model was trained to predict the treatment response in DME. Similar to the application of treatment prediction in AMD, this approach might be useful to identify patients benefitting from less intensive treatment without the burden of overtreatment and enhanced risk of severe complications, such as endophthalmitis. In this example, a CNN was trained

to identify treatment response defined as a reduction of CRT of 10%. The algorithm achieved an AUC of 0.866 for discriminating patients responding well to anti-VEGF compared with those who did not respond well (Rasti et al., 2020). As CRT has been proven, by AI analysis, to represent a valid marker of IRF/SRF volumes in DME, such a CRT-based tool may be clinically useful in DME.

### 3.5. Measurement of fluid resolution in retinal vein occlusion

The BRIGHTER (for branch vein occlusion) and CRYSTAL (central vein occlusion) studies investigated the use of ranibizumab in PRN regimens for RVO, and encompassed detailed quantitative analysis of macular fluid resulting RVO. Similar to DME, IRF and SRF volumes are highest in the foveal center (Michl et al., 2020a). Comparable to DME, IRF was also located higher temporally than in other topographic locations around the fovea. SRF on the other hand was higher in the inferior section of the macula, indicating a gravitational tract which can also be seen in rhegmatogenous retinal detachments and CSC (Ahn et al., 2013; Kirkby and Chignell, 1985; Pang and Freund, 2014).

Different to DME, most of the IRF volume (over 95%) is absorbed after the initial injection in RVO, followed by a further decline of less than 1% of the original volumes over the subsequent months. The same is true for the decline in SRF; initially almost 95% of SRF resolves with less than 1% of SRF volume reduction thereafter. Ultimately, almost 98% of macular fluid will be resolved after 12 months of follow-up (Michl et al., 2020a). This resolution pattern reflects in a most robust manner the value of AI-based OCT analyses as a fluid-meter under therapy. Fig. 18 highlights the different resolution patterns in an exemplary manner, revealing the fingerprint style of therapeutic fluid dynamics in the different pathologies. As described in the pathophysiology section, many pathognomonic variables are to be considered: The cytokine patterns including VEGF alone or other inflammatory cytokines as occurs for example in DME, the combination of different cellular mechanisms such as photoreceptor, Muller cells or RPE cell metabolism as occurs for example in AMD as well as a manifest vascular biological alteration in DME and RVO or a predominantly neurodegenerative component in AMD and DME.

### 3.6. Fluid determination using AI in different diseases

Some macular fluid investigations have been performed in other retinal diseases, where anti-VEGF was not the primary treatment. In CSC, SRF volumes do not differ between chronic and acute forms. Unsurprisingly, acute CSC showed greater spontaneous reduction in SRF fluid volume after one month of follow-up (Ahn et al., 2013). In ocular toxoplasmosis, SRF topographically co-localizes with the site of inflammation and retinal necrosis. A good response to anti-toxoplasmosis therapy can be seen in these cases, however, worse response rates have been described for IRF or secondary neovascularization, even with anti-VEGF therapy (Ouyang et al., 2015). How fluid volumes in chronic CSC respond to photodynamic therapy and how anti-VEGF treatment supports fluid decrease due to secondary neovascularization in diseases such as CSC, macular telangiectasia or myopic degenerations is not yet known. Nevertheless, with automated AI algorithms becoming commercially available, fluid volume measurement will introduce clear guidance for the management of any disease associated with macular fluid. A precise evaluation of fluid and other (sub-)clinical markers by means of AI in disease progression as well as under therapy will allow OCT imaging to be used beyond just as a VEGF-meter (Schmidt-Erfurth et al., 2017b).

### 3.7. AI in real-world fluid analysis

Macular fluid assessment is the best option for exploiting the full potential of three-dimensional OCT images used every day in busy clinics. Volumetric OCT also offers the opportunity to include even more

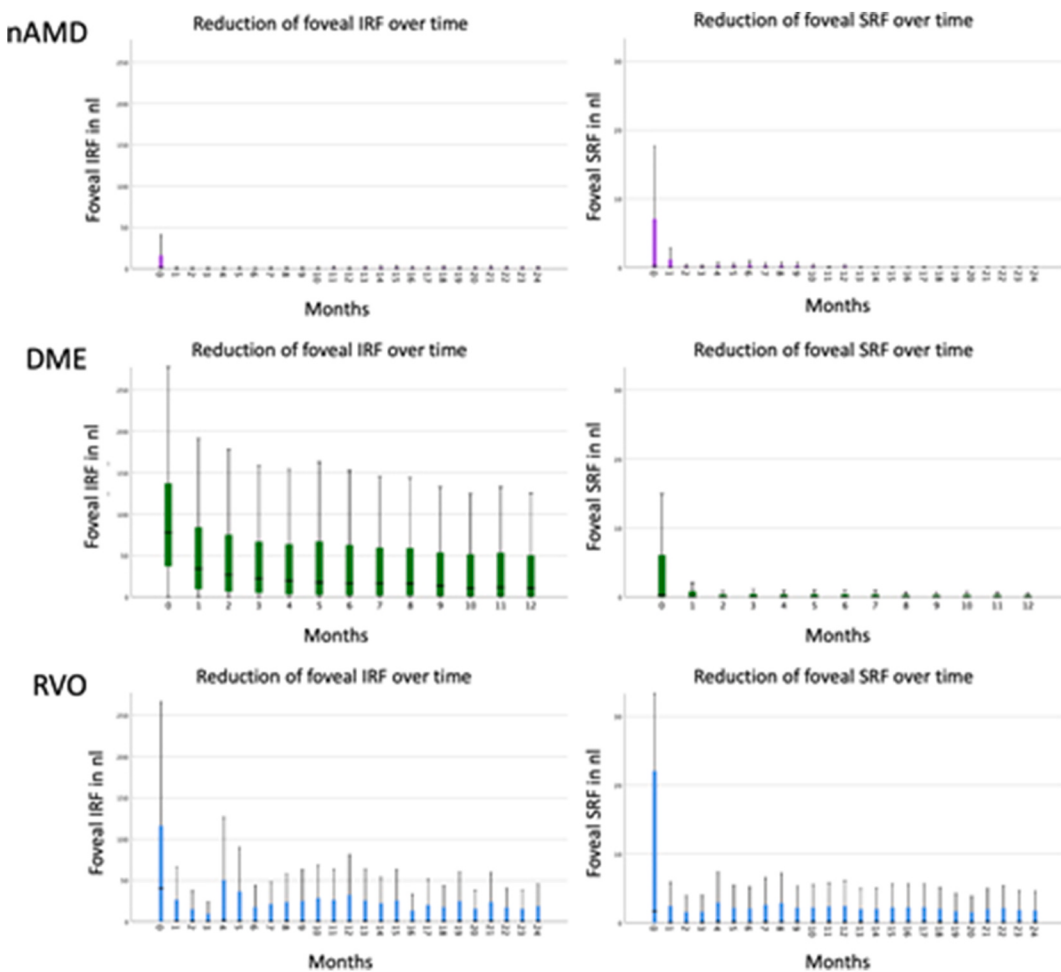


**Fig. 18.** Artificial intelligence for fluid monitoring over time offers insight into disease-specific fluid resolution patterns. Intraretinal fluid (IRF) and subretinal fluid (SRF) are presented with the same scale for all three diseases. In neovascular age-related macular degeneration (nAMD), IRF volumes are primarily low, respond immediately to treatment and remain low with fluctuations in extremely small volumes. SRF is usually present in higher volumes and resolves slightly slower than IRF. In diabetic macular edema (DME), IRF is most resistant to treatment and this is seen throughout the entire follow-up, while SRF resolves early and rapidly. Retinal vein occlusion (RVO) is associated with continuous fluctuations during therapeutical monitoring in both IRF and SRF compartments. SRF appears more relevant in RVO than in the other two diseases at baseline and during follow-up.

relevant biomarkers when assessing real-world patients. SHRM and fibrosis are just two important clinical markers that need to be investigated in their relation to macular fluid (Roberts et al., 2019). A paradigm shift is needed to move away from substitutes of disease activity to real-time and reproducible quantifications that realistically identify the pathomechanisms of disease and are the key features responsible for vision loss in our patients. Understanding disease activity and true responses to established therapies will drive novel treatment strategies, such as prolonged treatment intervals with innovative intravitreal agents and refillable drug delivery systems. Furthermore, those patients benefitting most from each of the available treatment options will be identified. Real-world outcomes are crucial for an unbiased understanding of conversion and progression of disease activity and therapeutic potentials. Yet so far, only few analyses using AI in the retina are available.

Moraes et al. applied a deep learning algorithm for automated quantification to OCT images of eyes with nAMD in the Moorfields Eye Hospital AMD database. The images were taken at baseline presentation before therapy (Moraes et al., 2020). A total of 2473 first-treated eyes and 493 s-treated fellow eyes were included. Volumes were segmented and calculated for multiple features such as NSR, drusen, IRF, SRF, SHRM, RPE, HRF, fibrovascular PED (fvPED) and serous PED (sPED). In conclusion, the majority of first-treated eyes exhibited both IRF and SRF

features. First-treated eyes had greater volumes for all segmented tissues. With the exception of drusen, older age was associated with lower volumes for RPE, SRF, NSR, and sPED. In second-treated eyes, older age was associated with lower volumes of NSR, RPE, sPED, fvPED, and SRF. Greater volumes of the majority of features were associated with worse VA. Spatial location in respect to the fovea was not considered. Fluid volumes did not follow a linear regression, which makes the interpretation of this analysis difficult. A ground truth evaluation for the feature segmentation by a reading center would be useful to separate anatomically confluent features such as SHRM, fvPED and RPE volume.

Gerendas et al. performed deep-learning-based automated fluid quantification in real-world clinical routine OCT images showing neovascular AMD with a follow-up of over 5 years (Gerendas et al., 2018b, 2021). Data from the Vienna Imaging Biomarker Eye Study (VIBES) registry from 2007 to 2018 (electronic patient record, treatment database and two OCT devices) were analyzed using the Vienna fluid monitor, an automated fluid segmentation tool based on deep learning. Matching all entries and filtering for active nAMD by baseline OCT of suitable quality for automated IRF, SRF and CST segmentation led to inclusion of 1127 eyes. Visual acuity and OCT at baseline, month 1–3 and years 1–5, age, sex and number of treatments were included in the analysis. The investigators found that the mean CST with 358 µm at baseline decreased to 280–303 µm over the entire follow-up. IRF and

SRF volumes were at their maximum at baseline (IRF: 21.5/76.6/107.1 nl in 1/3/6 mm area; SRF 13.7/86/262.5 nl in the 1/3/6 mm area). IRF decreased to a mean of 4–5 nl at month 1–3 in the 1-mm area and increased to 11 nl at year 1 and to 16 nl at year 5. SRF decreased to a mean of 3–5 nl at month 1–3 in the 1-mm area and remained below 7 nl until year 5. IRF was the only variable to symmetrically reflect the course of visual acuity change over time. Fluid control was optimal during the loading dose and volumes increased only slightly and in a stable manner over the following years in this real-world treat-and-extend regimen. 4.5 treatments were given during the first year and about 2.5 treatments per year subsequently. A ground truth validation by readers certified by the Vienna Reading Center was also performed in this study and confirmed the findings from automated analyses. This work provided proof-of-principle that deep learning-based automated fluid quantification in clinical routine images is well-suited for objectively, reliably and rapidly measuring treatment response and potentially for guiding clinical management in nAMD. Moreover, the fluid monitor introduced reading center expertise and substantial time saving analyses to clinical routine. Automated volume measurements of retinal fluid compartments in a real-world dataset over a period of many years suggested IRF volume as an ideal guidance for optimal treatment decisions.

Keenan et al. evaluated retinal fluid volume data extracted from OCT scans by AI algorithms from different clinical trial and real-world settings. Interestingly, wide ranges that differed by population were observed at the treatment-naïve stage: 0–3435 nl (IRF), 0–5018 nl (SRF), and 0–10022 nl (PED). Mean volumes in each compartment decreased rapidly and consistently during anti-VEGF therapy under standardized trial conditions as well as in real-world scenarios. During the maintenance therapy, mean IRF volumes under therapy were highest in a Tel-Aviv practice dataset (100 nl), lower in the clinical cohort set from Belfast and the HARBOR-PRN study arm, and lowest in the HARBOR monthly arm (21 nl). Mean SRF volumes were low in all cohorts with 30 nl in HARBOR monthly and 48–49 nl in the other cohorts. Yet, fluid quantification also demonstrated less control of fluid in real-world settings (Keenan et al., 2020a). This detailed comparison of fluid outcome variables in different settings also highlights the variability in individual populations and the influence of different treatment patterns.

Chakravarthy et al. studied the effect of repeated macular fluid volume fluctuations during anti-VEGF maintenance in nAMD (Chakravarthy et al., 2021). Data were extracted from electronic medical records of 381 patients with nAMD, aged ≥50 years; baseline VA ≥33 and ≤73 letters; ≥24 months' follow-up and ≥2 OCT measurements. OCT scans were analyzed using an AI algorithm that quantified the volumes of IRF, SRF, PED and CST. As a measure for volume fluctuations, the SDs were computed and categorized into quartiles (SD-Q1-4). However, SDs from the a priori small volumes resulted in very low fluid amounts and were based on few (>2) visits with widely different intervals over 24 months. BCVA was significantly lower after 2 years in eyes experiencing most fluctuations in CRT. IRF had the greatest impact on function and SRF the lowest. Noteworthy, PED had the highest SD volume values and was included in CRT and total fluid amounts. The differences were consistent between Q1, showing close to no fluid, and Q4, with most fluid. However, less consistent correlation was seen between the other quartiles and fluid volumes. Visit numbers varied extensively across the cohort, the patient sample was moderate, with only 22% of eyes from the overall cohort included, and the performance of the algorithm used has so far not been demonstrated in the literature. Fluctuations can only be detected if high enough fluid volumes are present. In overall small volumes, a relative change or SD of minor amount will not cause substantial clinical effects. Continuous fluctuations in a bimonthly fixed regimen with aflibercept did not lead to inferior outcomes in clinical trials. In routine practice, fluid volumes should be quantified accurately and in a user-friendly manner during the individual course of therapy to control for recurrence in a timely manner.

Behavior in clinical practice has particularly changed further

towards an anatomic, i.e., OCT-guided, treatment and away from extended visits including visual acuity assessments due to the impact of the COVID pandemic. AI does not only offer quantification, but also a detailed qualitative differentiation of retinal fluid. Treat-and-extend regimens with their proactive approach may provide optimal outcomes, although at a higher injection frequency. However, it is not the total number of injections but the time-sensitive personalized application that matters.

#### 4. Association of fluid with function by AI-based fluid quantification

Structure-function analysis in ophthalmology has traditionally been associated with the field of glaucoma. Despite the opportunity of precise topo- and tomographic evaluation of the structure of interest following the introduction of OCT, researchers have been struggling with the development of robust structure-function correlation in glaucoma. Investigating structure-function in macular disease poses an even more complex task. Macular disease typically alters a multitude of structures, of which functional impairment is routinely measured by BCVA, a variable which does not reflect the entire functional spectrum of the macular area, but merely the fovea. Nevertheless, the introduction of SD-OCT as a standard assessment in both clinical trials and routine tertiary care has extended the possibilities for tackling this task. Reliable structure-function analysis allows 1) drawing of conclusions about the functional impact of disease and thereby the development of hypotheses about underlying pathoanatomical mechanisms, 2) observation and interpretation of the treatment response, and consequently, 3) the development of informed standards and guidelines for optimal therapeutic outcomes. Macular fluid has been proven relevant to function, most prominently in nAMD, DME and RVO, and its assessment has been revolutionized by AI-based assessment of its appearance on three-dimensional SD-OCT data. The increase in informative content following such sophisticated extraction is reflected by the opportunities which arise from the novel technology: Quantified explainability of function through fluid enables a more differentiated understanding of a disease activity and its progression course. Furthermore, quantification of fluid changes introduced by treatment opens a whole new dimension of interpretable data with the ultimate goal of informing prognosis and treatment strategies. Challenges and limitations of structure-function analysis include the difficulty of interpreting retrospective data with respect to the underlying protocols according to which the data was collected, the inherent bias of feature presentation such as the topographic co-localization of features, and the effect of morphological and functional factors not accounted for.

##### 4.1. Fluid and function in neovascular AMD

Standardized OCT imaging and functional assessment in the pivotal anti-VEGF trials, mentioned in the previous chapters, have provided a promising basis for structure-function analyses in nAMD. Prior to automated fluid segmentation, such analyses were naturally based on expert grader-based determination of the mere presence/absence of fluid in the intra-, subretinal and sub-RPE compartments unrelated to the amount and mostly also without localization. The results gave rise to the concept of distinct functional implications of exudative features or morphological “phenotypes”. Before reviewing the success story of the role of AI-quantified fluid in fluid-function analyses, we will therefore summarize the main findings based on qualitative post-hoc analyses of large, prospective clinical trials.

Post-hoc analysis of the CATT, EXCITE and VIEW trials of nAMD showed that the presence of foveally located IRF at the treatment-naïve stage corresponded to lower BCVA by up to two lines at baseline and at follow-up in several analyses. This observation was made for IRF independently as well as in combination with other morphological features (Jaffe et al., 2019; 2013; Schmidt-Erfurth et al., 2015; Sharma et al.,

2016; Simader et al., 2014; Waldstein et al., 2016b). Furthermore, baseline IRF predicted lower BCVA gains during anti-VEGF therapy, independent of baseline BCVA and the therapeutic agent or regimen, in a post-hoc analysis of the VIEW trials. IRF occurring during follow-up corresponded to commensurate reduction of BCVA. Persistent IRF beyond the loading phase in particular has been shown to correspond to even lower VA. Further, recurrent IRF when switching to infrequent (quarterly afibercept) dosing in combination with an underlying PED was associated with progressive functional decline (Schmidt-Erfurth et al., 2015).

Interpretation of the impact of SRF on function is less straightforward, as results do not present as uniformly. In general, however, the presence of SRF shows less association with BCVA than does the presence of IRF. Reported implications of baseline SRF range from no prognostic value to predicting higher BCVA gains by month 12 (after adjusting for baseline BCVA). Analyses suggest the presence of SRF at baseline, particularly when it is the only exudative feature, are associated with a lower risk for significant vision loss during anti-VEGF therapy (Simader et al., 2014; Waldstein et al., 2016b, 2016c). Patients presenting with foveal SRF at year 2 showed better BCVA in a post-hoc analysis of the CATT study than patients with extrafoveal or no SRF, even when controlling for other confounding variables, such as concomitant atrophy which has been suspected to be less likely in patients with SRF (Gune et al., 2020). Furthermore, BCVA gains from infrequent treatment appeared to be similar to those in frequent treatment in patients presenting with SRF at baseline in a post-hoc analysis of the EXCITE trial (Waldstein et al., 2016b). Consequently, a less stringent need for retreatment of SRF is suspected by many in the scientific and clinical community. The T&E regimen offers suitable conditions for shedding light onto the role of SRF as a biomarker for determination of subsequent treatment intervals. Hence, the FLUID trial investigated the non-inferiority of a T&E regimen more tolerant of SRF. The authors reported comparable BCVA outcomes in patients treated with an SRF-tolerant approach versus those in which complete resolution of SRF was mandated. However, AI-based quantification of fluid applied to the FLUID trial data, as discussed previously, provides intriguing evidence of the necessity for an objective fluid quantification for in-depth interpretation of such datasets, as overall SRF volumes did not differ in the study arms at any study-specific time point (see following paragraphs).

#### 4.2. Fluid-function correlation enabled by precise fluid quantification

Waldstein et al. were the first to report on the correlation of three-dimensionally manually quantified fluid and visual acuity in a small patient cohort (Waldstein et al., 2016a). Several weights (with respect to topographic location of fluid and dimensions of fluid extent) were applied to the manually delineated features and revealed IRF to show the best correlation with BCVA when analyzed by area, height up to 20 µm, and foveal location. Thereby, 60% of baseline BCVA could be explained by three-dimensionally quantified IRF. 40% of the BCVA change by one year was explained by changes in IRF-related metrics. Nevertheless, irrespective of baseline BCVA and morphological change, baseline IRF correlated with BCVA at month 12, explaining it by 20%. This highlights the permanent damage caused to the retina by IRF. None of the weighted variables calculated for SRF showed any significant correlation with BCVA.

With the rise of automated image analysis, tedious and time-consuming annotation of exudative components such as in the previously described investigation were surpassed by AI-based segmentation. This enabled analyses on immense scales, such as that of the HARBOR dataset: Schmidt-Erfurth et al. used a random forest machine learning approach to investigate the strength of correlation between AI-quantified measurements of IRF, SRF and PED with BCVA in more than 600 patients. Baseline correlation between fluid and function was moderate and confirmed IRF, specifically the horizontal extension of IRF, as the most relevant fluid-based marker for function. SRF and PED

ranked low, even inferior to measurement of total retinal thickness (Schmidt-Erfurth et al., 2018a). As expected in a sensitive neurosensory environment, the potential of fluid alone in explaining BCVA in nAMD, but also other macular diseases, is limited by the influence of additional morphological conditions, such as photoreceptor integrity, vitreomacular interface as well as fibrotic and atrophic changes. Our group applied a multivariable mixed effects regression model in a different approach to the HARBOR dataset aimed at providing quantitative correlation between foveal fluid volumes and BCVA. While IRF showed a consistently negative impact, SRF correlated slightly positively with BCVA. Both effects were more pronounced at baseline. This was the first time the volume-dependent impact of fluid on BCVA in nAMD was quantified in a reproducible manner enabled by its AI-based segmentation: Per 100 nl of foveal IRF, BCVA was reduced by -4 letters, whereas the same amount of foveal SRF correlated with an increase of BCVA by +2 letters (Schmidt-Erfurth et al., 2020b). Automated fluid segmentation also allows quantification of fluid and function dynamics under therapy. The HARBOR data showed a therapeutic decrease of foveal IRF and even more so of foveal SRF reflected in a corresponding increase in BCVA (+2.13 letters per 100 nl decrease of foveal IRF and +5.88 letters per 100 nl decrease of foveal SRF) (Riedl et al., 2021). Furthermore, the study provides evidence that patients presenting with persistent IRF after the loading dose are more strongly compromised even before treatment initiation, suggesting that persistent IRF should be considered as degenerative instead of exudative and may be a sign of disrupted retinal integrity.

Post-hoc AI-based quantification of fluid in the aforementioned FLUID trial allows for more in-depth analysis of SRF and function. Reiter et al. reported that SRF volumes did not differ between treatment arms, a fact inherently limiting the possibility of detecting any relevant difference in function (Reiter et al., 2020a). Furthermore, Grechenig et al. showed that residual SRF followed by visit extension had a negative effect on visual acuity. Interestingly, residual SRF volumes further increased to the subsequent visit when tolerated. Visual acuity declined at the visit subsequent to SRF-tolerance, indicating an – at least in the short term – worsening in BCVA. (Grechenig et al., 2021).

#### 4.3. Fluid as a predictor of function

The pre-AI era provided valuable evidence of the prognostic implications of morphological phenotypes: The presence of IRF at baseline correlated with lower BCVA gains, while similarly increased gains in BCVA have been reported in association with baseline SRF (Simader et al., 2014; Waldstein et al., 2016b, 2016c). Nevertheless, even using objective fluid-function correlation by fluid quantification, fluid variables rank far behind baseline BCVA in predicting BCVA outcomes. Advanced neurosensory alteration can be noted even in early AMD. Obviously, therefore, pre-existing neurosensory damage has to be considered in nAMD before CNV develops (Vogl et al., 2021).

Based on random forest machine learning, metrics related to the IRF area proved most informative among all fluid-based features for predicting BCVA outcome (Schmidt-Erfurth et al., 2018a). No prognostic effect of baseline fluid volumes could be determined in the multivariable mixed effects regression models reported in the previous paragraph. Persistent parafoveal IRF following the anti-VEGF loading phase was the only variable of prognostic value, being associated with lower BCVA gains (7.5 vs 11 letters)(Riedl et al., 2021; Schmidt-Erfurth et al., 2020b). Hence, fluid per se is not a surrogate marker for absolute function, as it is greatly for exudative activity and therapeutic efficacy. While quantitative fluid metrics have not proven to be informative in prognosticating functional outcome, they have been associated with other important aspects of disease course, such as anti-VEGF treatment requirements. Accordingly, a classifier was able to predict a low (no more than 5 injections within 2 years) and a high (more than 15 injections within 2 years) treatment requirement by using the quantitative fluid metrics of baseline and the following 2 months (Bogunovic et al.,

2017). However, underestimating the individual retreatment need and lack of timely retreatment is the overwhelming dilemma in real-world practice. The aim now is to identify those fluid components and features which are optimal and functionally relevant guides for therapeutic intervention by using advanced AI tools.

Topographic co-localization of exudative features of different compartments presents one of the challenges in interpreting fluid-function analyses. AI-based quantification of fluid has here once more contributed to improving our understanding. Precise voxel-wise localization has shown that IRF and SRF, as well as SRF and PED, demonstrate low (axial) spatial correspondence, while IRF and PED are more likely co-localized (Klimscha et al., 2017). Also, SRF is more likely to be found in large amounts outside the foveal region, whereas IRF is often located centrally (Michl et al., 2020a). Regarding functional implications, the suitability of BCVA as a measure of macular function for in-depth morphologic considerations has to be questioned. To this end, an alternative approach is discussed in the following paragraph.

#### 4.4. Reaching beyond conventional functional and morphologic testing

The conventional assessment of BCVA is solely a measure of photopic function at the point of central fixation, while functional assessments such as topographic microperimetry (MP) offer higher-level, spatially resolved information (von der Emde et al., 2019). Applying methods of deep learning to MP data has shown that predicting retinal sensitivity from OCT is feasible in healthy and diseased cases within the test-retest variability of the method itself (Seeböck et al., 2019a). With respect to structure-function analyses, relevant knowledge is expected to be gained from the correlation of OCT-derived morphology with MP-derived retinal sensitivity, i.e., functional mapping. Such analysis has revealed a high potential for functional improvement in topographic locations affected by SRF at baseline using manual annotation. Interestingly, a disintegration of the photoreceptor signal on OCT has been shown to follow SRF resolution (Riedl et al., 2020). AI-based quantification of fluid and analysis of the photoreceptor bands (Orlando et al., 2020) is expected to shed light onto the functional implications of such anatomical phenomena. Furthermore, the development of high-resolution imaging modalities such as adaptive optics (AO)-OCT opens new horizons in assessing photoreceptor morphology (Reumueller et al., 2020). Reumueller et al. showed photoreceptor misalignment persisting through one year after resolution of SRF in macula-off detachments receiving successful surgery.

In conclusion, AI-based quantification of fluid has achieved a deeper understanding of the effects of fluid on function in nAMD. IRF at all time points was proven detrimental for VA in a volume-dependent fashion. Assessment of three-dimensional IRF has revealed a tighter association with permanent damage than has been shown for other forms of exudation, especially if IRF does not resolve following an anti-VEGF loading phase. SRF in comparison appears to entail a higher potential of functional recovery in nAMD. However, optimal outcomes in this respect depend on appropriate treatment, as BCVA improvement is shown to correlate with SRF to an even greater extent than to IRF. While quantitative metrics of fluid at baseline indicate little about prognosis – highlighting the potential of recovery by fluid resolution – these metrics present a unique and most relevant indicator of disease activity and therapeutic response.

#### 4.5. Fluid and function in diabetic macular edema

Post-hoc analysis of IRF and SRF in DME has delivered coherent results on fluid-function correlation. As in nAMD, qualitative morphological analysis provided preliminary observations. Results of a manual morphological grading of the RESTORE and RESTORE-Extension data, performed in the standardized setting of a reading center, revealed lower BCVA levels at baseline in patients with IRF of more than 380 µm in height in the foveal center point. This effect accounted for around ± 3

letters and was maintained throughout the first year. The prognostic value of SRF in the same dataset was dependent on the underlying treatment strategy. While there was a trend for patients with baseline SRF to show beneficial visual outcomes when treated with ranibizumab, it appeared that laser treatment applied in patients with baseline SRF resulted in inferior BCVA (Gerendas et al., 2018a). With respect to anti-VEGF treatment, similar results regarding outcomes of patients with SRF were reported by Sophie, Lu and Campochiaro (2015).

Data such as that of the Protocol T trial of the DRCR, with more than 600 patients receiving anti-VEGF therapy according to a standardized protocol, provided suitable grounds for the extraction of quantitative information based on AI-based segmentation of fluid. Gerendas et al. conducted a post-hoc analysis of Protocol T and applied a random forest machine learning approach to a set of fluid-related features derived from retinal thickness and fluid (IRF and SRF) area and volumes, depending on ETDRS areas and three time points (baseline, month 3 and 6) (Gerendas et al., 2017). The results showed a limited potential for explaining BCVA at baseline, with IRC fluid being the most relevant feature. Baseline fluid also seemed to play a subordinate role in predicting BCVA at month 12. However, under therapy the importance of IRC resolution was relevant, as total retinal thickness and several IRC-related features at week 24 showed the highest predictive impact. Only foveal SRF area as a baseline feature seemed to convey a better functional outcome (Gerendas et al., 2017). A consecutive analysis of Protocol T revealed baseline SRF to be associated with a worse baseline BCVA (63.2 vs. 66.9) (Roberts et al., 2020). However, accurate fluid quantification allows for precise correlation with the functional response: Despite adjustment for baseline BCVA, patients with SRF showed higher BCVA gains than those without SRF. In quantified terms, every 10-nl reduction in foveal IRF corresponded to +0.15 letters improvement in BCVA, while every 10-nl reduction in foveal SRF corresponded to an improvement in BCVA by +0.34 letters. Effects of fluid in the parafovea were not found clinically relevant. Of interest, eyes with baseline SRF also presented with more baseline IRF and a higher reduction thereof after the first anti-VEGF injection, possibly adding to the higher potential of functional recovery in these patients. This pattern is unique for DME and cannot be extrapolated to nAMD.

Intraretinal exudation in DME can present as cystoid spaces, so-called IRC, but often also results in diffuse edema. A post-hoc semi-automatic approach of quantification of morphology in around 100 patients treated with aflibercept in the VISTA study differentiated between these presentations of intraretinal edema by introducing the metric of actual retinal thickness after subtraction of IRC volume. Both actual retinal thickness and quantified IRC showed a significant correlation with BCVA from baseline throughout week 100, but IRC proved most relevant in subsequent multivariate analysis. A semi-automated analysis revealed a weak correlation of SRF change with BCVA change as well as a correlation of SRF presence with higher functional gains and outcomes (+5 letters) (Ehlers et al., 2019).

In conclusion, knowledge obtained from manual, mostly qualitative morphological gradings was strongly supported by analyses applying automated AI-based fluid quantification. With respect to IRC/IRF, there is evidence of a role in vertical extension which shows function to deteriorate after surpassing an elasticity threshold of supportive retinal tissue. SRF, while being associated with decreased function at baseline, shows a potential for excellent visual recovery under anti-VEGF therapy, possibly surpassing that of patients without SRF at baseline. The fact that in the 5-year extension of protocol T CRT remained similar between years 2 and 5, but BCVA further worsened, indicates that neurodegenerative processes unrelated to fluid may be relevant (Glassman et al., 2020).

#### 4.6. Fluid and function secondary to retinal vein occlusion

Fluid-function correlation in RVO has not been as intensively investigated as in nAMD and DME. Analysis based on human grader

evaluation revealed only a moderate correlation of fluid components with BCVA. The functional response during therapy was irrespective of baseline morphology (Michl et al., 2020b; Yiu et al., 2020). To date the only available analysis including AI-based fluid quantifications as an influencing factor on BCVA has been provided by Vogl et al. Results of this repeated-measure, mixed-effects regression model show foveal IRF volumes to impact BCVA in a more pronounced negative way than foveal SRF volumes. Fluid volumes explained only a small portion of variance in BCVA, but did increase the accuracy of BCVA prediction (Vogl et al., 2017). RVO differs from DME and nAMD in duration with a sudden onset in a previously intact retina, while the two other diseases are the consequence of a chronic progressive pathway. Accordingly, the timing of the initial intervention is the most important prognostic factor in RVO, suggesting that fluid in different exudative diseases of the macula is not interchangeable despite the similar morphological appearance.

## 5. Potentials and challenges of AI-based fluid reading

The previous chapters have highlighted the breakthrough brought by the advantages of AI-based fluid segmentation systems in retrospective data analysis. Having an AI system that is able to automatically conduct fluid readings potentially in real-time also offers new opportunities in terms of prospective disease monitoring, patient handling and quality of treatment. At the same time, there are multiple aspects that need to be considered in order to successfully deploy such a system in clinical studies and the real world.

### 5.1. Issues of AI in clinical studies

Applying the AI-based fluid segmentation models prospectively in clinical studies would facilitate measurement of treatment effects more sensitively than the current traditional mode of measurement. For instance, CRT is a widely used measure of treatment effect, despite the fact that it represents a rather vague measure of disease progression and subsumes highly diverse pathological alterations in a single number (Deák et al., 2018). Instead, treatment effects and disease progression can be analyzed in more detail by applying an automated fluid segmentation algorithm. The type of fluid that causes the thickening, its location and quantity could be analyzed on a large-scale basis. Moreover, the ability of AI-systems to segment fluid in real-time is particularly useful in the case of treatment regimens that require immediate feedback based on the OCT during a visit, e.g., as in HAWK and HARRIER (Dugel et al., 2020a), where decisions about the injection interval are dependent on disease activity at a specific visit. Automated algorithms also have the potential to minimize measurement errors and reduce human-induced biases in the analysis, as has been demonstrated recently for the task of detecting the presence of fluid in OCT (Keenan et al., 2020b). Having a more detailed and standardized evaluation of treatment effects based on fluid segmentation in clinical studies would (1) improve comparability between drugs, (2) provide a better basis for treatment decisions in clinical practice and (3) be important for innovative drug development.

Validation of the algorithm is the first crucial step to bring AI ‘from bench to bedside’. AI algorithms are defined by the data used to train them and any bias in the data will hence be reflected in them. For example, AMD affects disproportionately more Caucasians than other ethnic groups and as a consequence many clinical trials are dominated by Caucasian patients. However, the PCV subtype of nAMD is more prevalent in Asian populations and AI trained on Caucasian clinical trial data may not operate with the same performance on the data from Asian patients. Thus, verifying robustness and accuracy requires validation on datasets that resemble the patient population which the algorithm will be applied to (Ting et al., 2019). This is essential, as there is no guarantee that AI models will generalize to new diseases, other device manufacturers or even imaging protocols that have not been seen during

training (De Fauw et al., 2018; Romo-Bucheli et al., 2020b; Terry et al., 2016). Due to well-defined patient populations, specific imaging protocols and predefined treatments, the validation for clinical studies is easier than for the real-world setting. However, it is also important to evaluate and compare the accuracy of the algorithm in the context of human-level performance, as accuracy can vary with respect to the target, disease population and/or the quality of image data (Hopkins et al., 2020). Besides the initial validation at an early stage, continuous monitoring and surveillance to detect potential flaws is also required (Qayyum et al., 2020).

### 5.2. Difficulties of AI fluid measurements in the real world

In general, digitization and the development of high-resolution imaging has been a driving factor in improving clinical care in ophthalmology over the past years. While inspecting the retina at a  $\mu\text{m}$  resolution allows the retinal condition to be diagnosed and analyzed in a more detailed way, it comes at the expense of overwhelming clinicians with massive amounts of data (Kurmann et al., 2019). The large number of OCTs in connection with millions of pixels per volume make manual inspection and analysis of these scans on a large-scale basis practically impossible (Foot and MacEwen, 2017; Schmidt-Erfurth et al., 2018b). Even assuming a consensus regarding the relevant imaging biomarkers such as fluid, clinical decisions may vary between physicians due to differences in professional experience, image quality, workload or time restrictions (Framme et al., 2012; Keenan et al., 2020b). In this context, AI-based approaches have the potential to overcome these limitations by segmenting and quantifying the amount of fluid in OCT scans in an automated way, providing a powerful tool for clinicians.

Rather than having clinicians performing a rough estimation of the amount of fluid in the retina by scrolling through the OCT volume, automated algorithms can provide exact numbers and statistics to clinicians (Schlegl et al., 2018). This constitutes a fundamental change, shifting from subjective, fuzzy interpretations towards precise and objective disease monitoring, analysis and decision making. The synergy between doctors and AI-systems has the potential to improve the quality of clinical care in several ways: First, rather than thinking about “how much fluid is there?” clinicians can focus on answering the question “what to do with this amount of fluid?”, which is the more important underlying question. Second, clear treatment guidelines based on quantitative numbers can be developed and – equally or even more importantly – will be transferable into clinical practice. This is of particular importance as the problem of treatment discrepancy between studies and the real-world is a well-known problem, e.g., the under-treatment of patients with AMD (Ciulla et al., 2018; Lad et al., 2014). Third, having these precise guidelines and real-time AI-based measures available, expertise could be extended to regions where not enough experts are available for patients (Kelly et al., 2019).

The well-defined patient cohorts, imaging protocols and treatment regimens that provide confidence in clinical studies are not available in the real-world setting, making it hard to define the extent to which an algorithm is properly validated. However, there are solutions to cope with this situation, such as implementing a feedback loop as an integral part of the system to enable continuous validation, providing uncertainty estimates together with the segmentation output of the AI model, or detecting samples that deviate from the expected distribution of diseases or imaging protocols (Kendall and Gal, 2017; Mundt et al., 2020; Orlando et al., 2019; Seeböck et al., 2020). Model uncertainty could be used to identify unreliable predictions, providing warnings to clinicians about samples to which the model does not generalize well. For instance, this has been proposed for the use case of diabetic retinopathy screening (Lim et al., 2019). In combination with the aforementioned feedback loop, the unreliable cases with inaccurate predictions could be subsequently used to re-train and also re-validate the model, improving its robustness and generalizability over time (Budd et al., 2019). An overview of this feedback loop is illustrated in

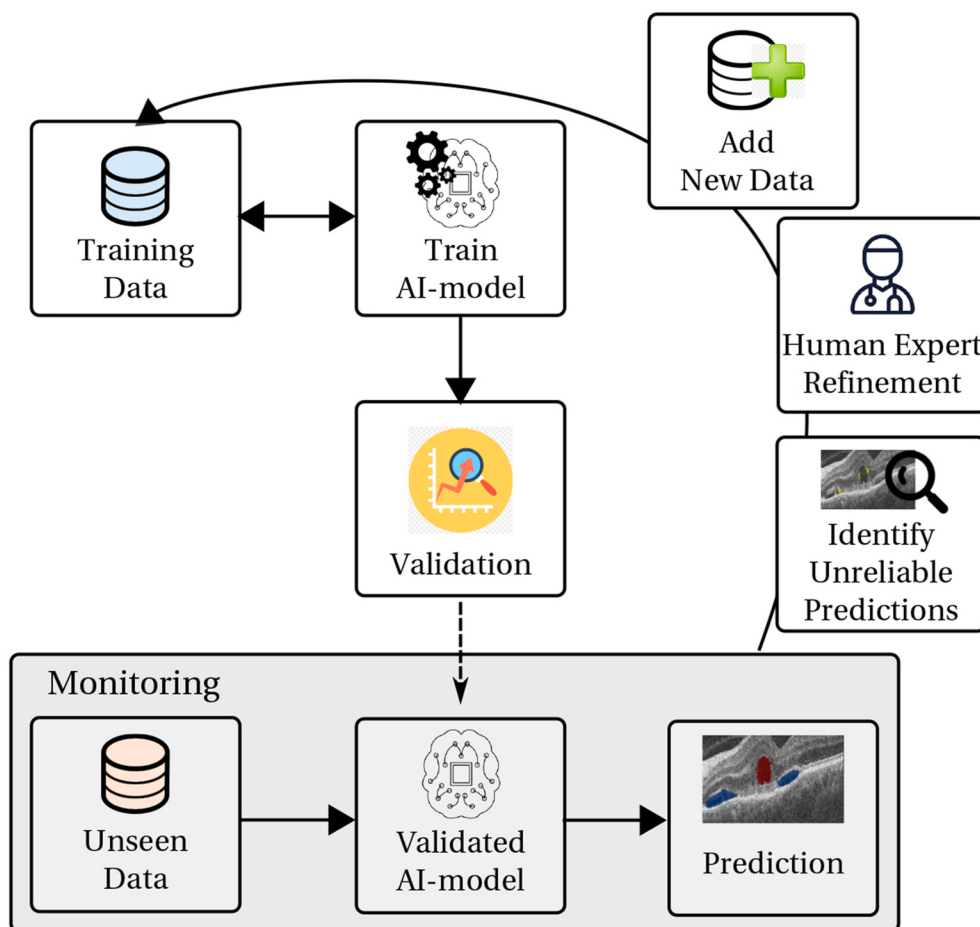


**Fig. 19.** Exemplary workflow of a feedback loop. After training and validation of the artificial intelligence model with the available datasets, unreliable predictions are identified during the monitoring process. This data can then be analyzed/labeled by experts and subsequently used to improve the performance of the segmentation model.

**Fig. 19.**

### 5.3. Technological solutions to improve AI performance in real-world data

The process of smartly selecting the most informative cases for extending the training data of the model is also known as an ‘active learning’ strategy (Goriz et al., 2017; Otálora et al., 2017). Tightly related to this is so-called ‘online’, ‘lifelong’ or ‘continuous’ learning, where models continuously learn with increasing amounts of data (Parisi et al., 2019). While one straightforward option is to incrementally train the models with new data, this can lead to the problem of catastrophic forgetting, where the performance of the AI model decreases on the data which was originally used for training the algorithm. Therefore, a better approach in the medical domain may be to clearly define new versions and releases of the algorithm that have been re-trained and re-evaluated on the complete dataset, including both ‘old’ and new samples.

Besides validation in retrospective datasets, prospective studies are needed to not only understand the performance of the AI model in the real-world setting, but also the system’s clinical effectiveness and how it integrates with specific clinical workflows. A DR screening tool developed by Google Health recently failed in a real-world setting due to several socio-environmental factors that had an impact on model performance, nursing workflows and patient experience (Beede et al., 2020). Amongst others, the combination of the cloud-based solution and a slow and unreliable internet connection slowed the whole screening

process, and differing lighting conditions rendered images ‘ungradable’ for the AI system. This highlights the importance of prospective evaluation and understanding contextual needs of clinicians and patients prior to widespread deployment, which is at least as important as the retrospectively evaluated accuracy of AI systems. It is critical that the end-users (clinicians, optometrists, nurses, etc.) not only understand the benefit and usefulness of the system, but also accept its use in clinical practice.

The interpretability of the model and transparency of decisions are usually important aspects with regard to AI models, especially for decision-making systems and screening tools (Qayyum et al., 2020). We argue that this is probably less important for the use case of AI-based fluid reading and providing accurate as well as robust segmentations (maybe together with their uncertainty) is enough to secure user acceptance.

One of the key challenges when deploying an AI segmentation model in practice is to ensure a certain response time until the segmentation result is available. AI-based systems allow segmentation of fluid in real-time, which would not be possible in a manual way. From a technical point of view, this requires sufficient computational power, sufficient redundancy to compensate for failures and a fast transmission of data between the systems involved. One implementation option is the ‘offline mode’, which provides computational resources at the site where the OCT is acquired (Fig. 20(a–b)). The advantage is that data remain on-site and must not be sent elsewhere. The downside is that this can be expensive and impractical with respect to deployment and maintenance, e.g., due to diverse computing environments at the sites. A second

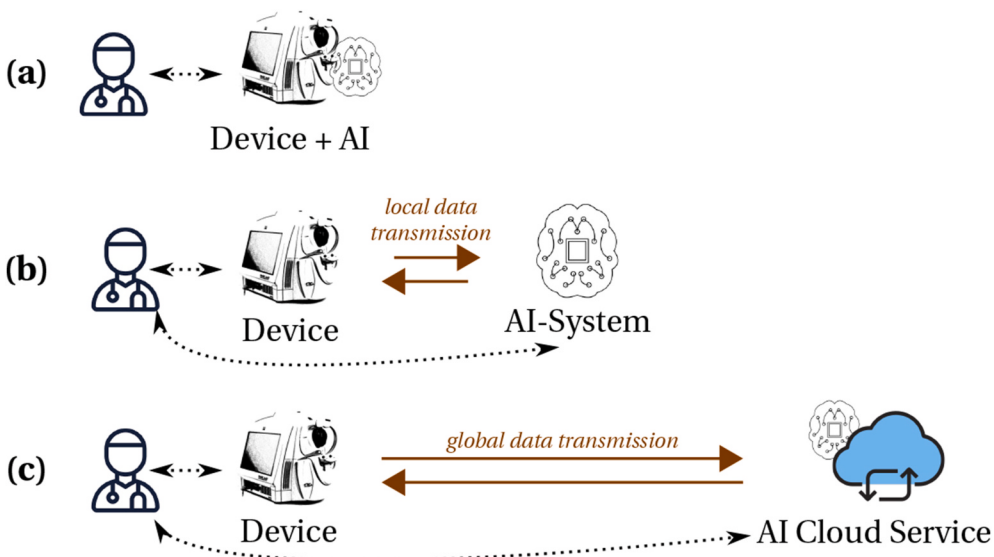


**Fig. 20.** Schematic view of different technical implementation options. In the ‘offline mode’, the algorithm can either be (a) directly integrated into the imaging device (no data transfer necessary) or (b) run on a separate dedicated local machine (data transfer only in the local network of the site). Results can be visualized in the imaging device or the separated machine. (c) In the ‘online mode’ the imaging data is sent via the internet to a cloud-based service, which either provides an online visualization or sends the results back to the site.

option likewise with pros and cons is the ‘online mode’, which offers a cloud-based solution with a centralized service where sites upload their data and download and/or view the results after processing has been finished (Fig. 20(c)). A fast internet connection is required to ensure real-time segmentation results. Examples for such a solution are the IDx-DR device for screening diabetic retinopathy in color fundus images and the Singapore Integrated Diabetic Retinopathy Programme, a national telemedicine DR screening program in Singapore (Nguyen et al., 2016; Van Der Heijden et al., 2018). Even though the second solution may be preferable from a technical point of view, other environmental factors, such as the speed of the internet connection, and legal, regulatory or data protection requirements, may be an impediment. Home-OCT is another interesting opportunity to provide immediate feed-back on retinal fluid at a patient level (Keenan et al., 2020a).

An open question is how to best present and visualize the fluid segmentation results to the clinicians. Besides highlighting the segmented fluid directly in the image, additional visualizations and statistics can be useful (Röhlig et al., 2019). Calculating the total amount of fluid over the whole volume enables a summary of the segmentation in a single number and a clear visualization of the general trend of fluid over time, but may be an oversimplification from a clinical point of view, not capturing localized fluid dynamics (Klimscha et al., 2017; Michl et al., 2020a). Doing the same for specific regions may be a better trade-off (e.g. based on the ETDRS grid), but could complicate the interpretation over time between visits and may still miss important information such as the (spatial) relation between different types of fluid. The best visualization variant is probably a combination of multiple techniques and depends on the specific application as well as on established treatment guidelines (Johnson, 2004; Kortüm et al., 2017). Another potential aid could be to present complex treatment guidelines visually mapped in comparison with the individual progression of disease.

In conclusion, real-time, AI-based fluid reading has the potential to improve the quality of clinical care as well as to complete tasks more efficiently and facilitate measurement of treatment effects immediately in detail. To take advantage of this potential, however, it is necessary to be aware of the challenges and to address them in a proper and plausible manner.

## 6. Deep learning in OCTA in CNV and DME

OCTA is an advanced development of OCT imaging and is strongly dependent on AI methodology for signal detection and analyses. Angiographic imaging can support fluid analysis because pathologic

vascular changes usually precede or accompany fluid accumulation (Bailey et al., 2019; Hsieh et al., 2019). As exudation consecutively produces irreversible vision loss (Brown et al., 2006; Douvali et al., 2014; Martin et al., 2011), the ability to predict eyes that will develop exudative lesions from preceding subclinical vascular biomarkers may improve clinical outcomes. The ability to monitor MNV itself rather than exudation associated with MNV may improve guidance of anti-VEGF treatments for nAMD. However, traditional angiographic imaging modalities – which include fluorescein (FA) and indocyanine green angiography – are invasive and time-consuming procedures that rely on dye injection to highlight blood vessels and do not register directly to OCT images. This means they must be used sparingly and are ill-suited for routine monitoring. Consequently, they are less likely to detect early or subclinical pathology and less able to guide treatment. OCTA is better approach to fulfilling this need.

Small blood vessels and capillaries have similar reflectivity to the tissues they are embedded in. Structural OCT is not sensitive to such small vessels as it relies on reflectivity to produce images. To detect capillaries and other small vessels, OCTA measures motion contrast between multiple sequentially captured OCT scans (Jia et al., 2012; Makita et al., 2006; Wang et al., 2007). Motion contrast enables OCTA to image retinal microvasculature because the flow of erythrocytes through blood vessels produces dynamic alterations in the OCT signal that are not present in static tissue (Fig. 21).

OCTA inherited many of the properties of OCT imaging because it is based on the structural OCT signal. It is non-invasive, which is paramount for routine imaging and monitoring. But OCTA also has several other advantages over dye injection techniques. It offers high-resolution and is depth-resolved, offering accurate axial localization and focus. Both of these features can help detect even subclinical pathology, for instance by providing the capability to characterize vessel density and morphology precisely (Alam et al., 2020; Hsieh et al., 2019; Khansari et al., 2017; Kuehlewein et al., 2015a; Wang et al., 2019a; Xu et al., 2018).

### 6.1. OCTA algorithms for precision diagnosis in neovascular AMD

High-resolution, three-dimensional imaging is especially useful for characterizing MNV (De Carlo et al., 2015; Jia et al., 2014; Moult et al., 2014). As noted above, this is in part because OCTA is ideally suited for monitoring MNV progression and treatment response (Fig. 22). OCTA quantification of MNV can be informative even beyond mere observation. By quantifying MNV size, it has been shown that MNV vessel area

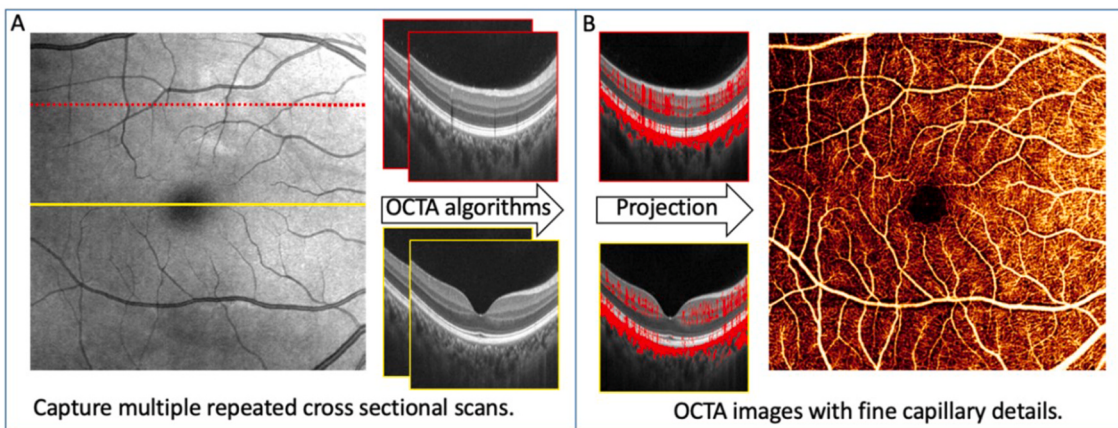


**Fig. 21.** Signal generation in optical coherence tomography angiography (OCTA). (A) Sequential structural OCT B-scans are captured at two different transverse locations, indicated by the red and yellow lines. (B) Motion contrast measurements yield the location of blood vessels, shown overlaid in red on cross-sectional images. By segmenting retinal layers and projecting the flows signal across the slabs, en face OCTA images can be constructed. (For interpretation of the references to color in this figure legend, the reader is referred to the Web version of this article.)

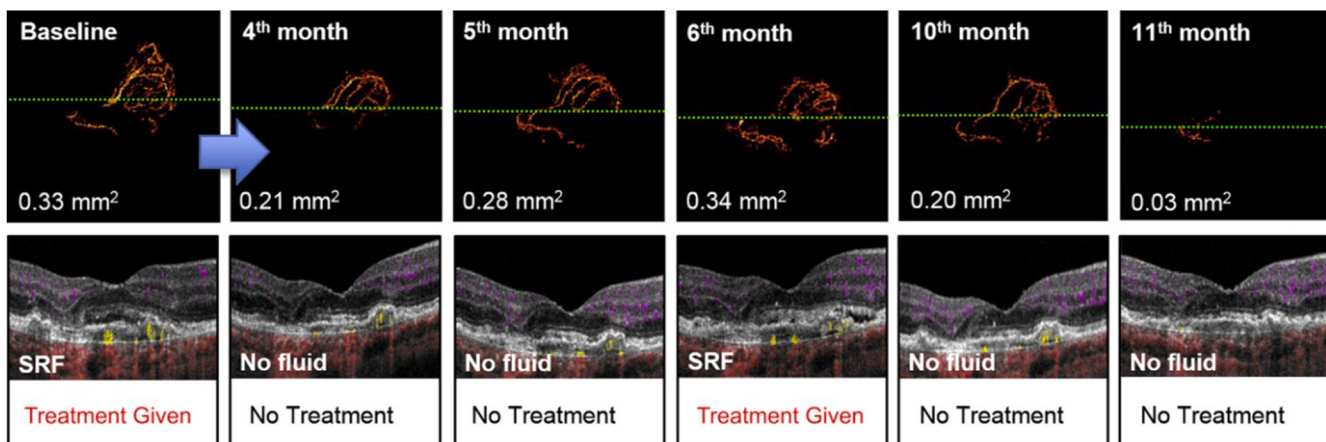


**Fig. 22.** Choroidal neovascularization (CNV) treatment response as seen by optical coherence tomography angiography (OCTA). Top row: En face OCTA of the outer retina. Bottom row: Cross-sectional images taken at the location of the green line in the en face image. The flow signal is overlaid on the reflectance signal, and color coded according to depth (violet: Inner retina; yellow: Pathological vessels in the outer retina; red: Choroid). This patient underwent pro re nata anti-vascular endothelial growth factor treatment, receiving injections each of the first 3 months until sub-retinal fluid (SRF) resolved. During 5 months the CNV vessel area increased, but as no fluid was detected, additional treatment was not administered. At 6 months, fluid recurred and treatment was applied. Between months 10 and 11 a large spontaneous reduction in CNV vessel area occurred. OCTA quantification was able to detect changes in lesion size that preceded exudation during the treatment course. Reprinted with permission from McClintic et al. (McClintic et al., 2018). (For interpretation of the references to color in this figure legend, the reader is referred to the Web version of this article.)

tends to correlate with future exudation (McClintic et al., 2018). The same study also suggested that OCTA can be useful in predicting when exudation will develop. Because it can precisely determine the depth location of vessels, OCTA can easily differentiate type I (below the retinal pigment epithelium), type II (above the retinal pigment epithelium), and type III (originating in the retina) MNV (Coscas et al., 2015; Kuehlewein et al., 2015b; Malihi et al., 2017; Patel et al., 2018). OCTA has been used to measure the treatment response in specific lesion types (Lumbroso et al., 2015; McClintic et al., 2018; Miere et al., 2019; Nesper et al., 2018; Xu et al., 2018), with type II lesions shrinking more rapidly (Kim et al., 2019). Furthermore, because it does not rely on dye leakage to detect pathological neovascularization, OCTA can detect pre-clinical, non-exudative MNV lesions (Bailey et al., 2019; de Oliveira Dias et al., 2018). Multiple studies have found that eyes with non-exudative MNV are at increased risk for developing exudative AMD (Fig. 23) (Bailey et al., 2019; de Oliveira Dias et al., 2018; Heiferman and Fawzi, 2019; Yang et al., 2019).

All of these features support the clinical efficacy of MNV characterization using OCTA. However, OCTA imaging relies heavily on AI

methods to primarily extract the vascular signals. Locating MNV alone within the outer retinal layer of an OCTA volume (the slab between outer plexiform layer and Bruch's membrane) is challenging for several reasons, mostly as a consequence of the anatomic location of the MNV posterior to several retinal and RPE layers. Overall, flow signals are weaker in deeper layers than in superficial ones due to OCT signal attenuation. OCTA analysis of MNV must therefore contend with a noisier environment than OCTA focused on pathology that occurs in more anterior regions. Furthermore, many OCTA artifacts are strong and/or only occur in deeper layers. Predominant among these are projection artifacts, which project the appearance of superficial vasculature into deeper layers. Projection artifacts can be compensated by slab-subtraction (Jia et al., 2015; 2014; Zhang et al., 2015) or projection-resolved algorithms (Hou et al., 2019; Wang et al., 2017; Zhang et al., 2016), but even when these approaches are used, residual projection artifacts may remain. Another type of inevitable artifact is caused by eye ball motion. As the outer retinal slab includes the RPE layer which has a very strong reflectance, eye motion artifacts can coexist with MNV flow signals, even though multiple algorithms have

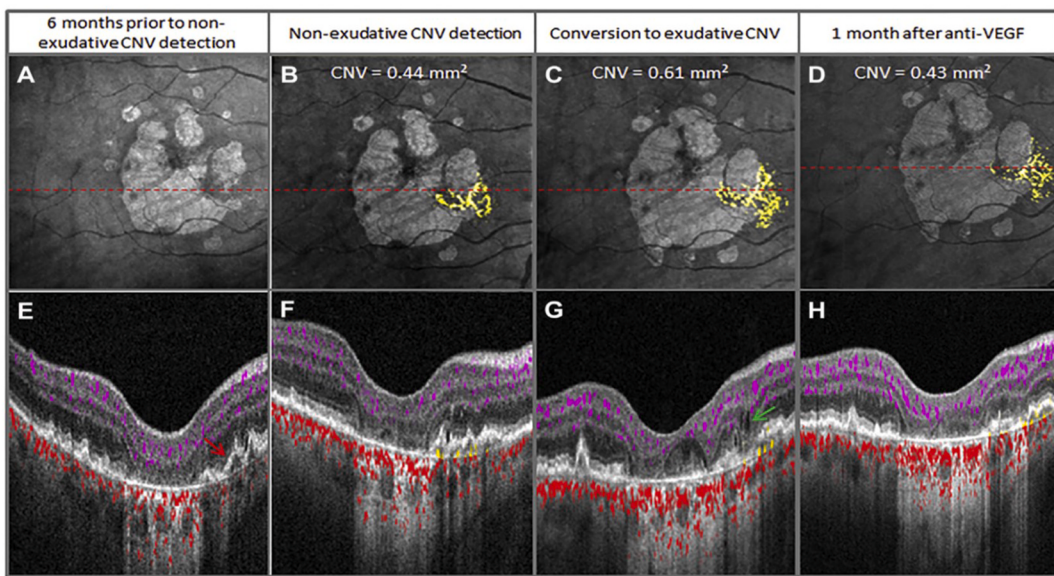


**Fig. 23.** Optical coherence tomography angiography (OCTA) imaging of choroidal neovascularization (CNV) progression. (A–D)  $6 \times 6$ -mm en face structural OCT images, with pathological outer retinal flow signal overlaid in yellow. (E–H) Cross-sectional images, with flow signal overlaid (violet: Inner retina; yellow: Pathological outer retina; red: Choroid). (A,E) Regions of geographic atrophy are apparent, as well as an irregularly elevated retinal pigment epithelium. However, no flow signal was detected. (B,F) OCTA detects CNV vessels prior to exudation. (C,G) Conversion to exudative CNV, with intraretinal fluid visible at the location of the green arrow. (D,H) Intraretinal fluid resolution and reduction in CNV vessel area following anti-vascular endothelial growth factor (anti-VEGF) treatment. Reprinted with permission from Bailey et al. (Bailey et al., 2019). (For interpretation of the references to color in this figure legend, the reader is referred to the Web version of this article.)

been developed to suppress them (Camino et al., 2017; Hou et al., 2019; Kraus et al., 2012; Makita et al., 2006; Wang et al., 2019b; Wei et al., 2018; Zang et al., 2016). Residual projection and motion artifacts can interfere significantly with MNV quantification.

For these reasons, manual MNV detection is prohibitively time-consuming. Due to the increasing clinical burden imposed by an aging population, this is not an inconsequential issue. As with some other OCTA biomarkers, reliable automation is the best solution for combating the issues arising from MNV's location. However, the location of MNV deep in the retina is not the only problem software solutions have to contend with. MNV lesions can also vary greatly in signal intensity, size,

shape, and location. Such wide variation in configuration can transform into critical mistakes for handcrafted algorithms (Liu et al., 2015). MNV quantification strongly requires context, and is thus a problem best approached by AI technology.

Wang et al. developed a composite MNV diagnosis and segmentation network by leveraging deep learning and a well-reasoned set of inputs (Wang et al., 2020a). The approach (Fig. 24) relies on inputting OCTA images processed in several ways which can be used complimentarily to distinguish projection and motion artifacts from a true MNV signal. The first step is a detection step, in which a CNN trained to segment MNV lesions diagnoses MNV based on the predicted lesion size. A separately

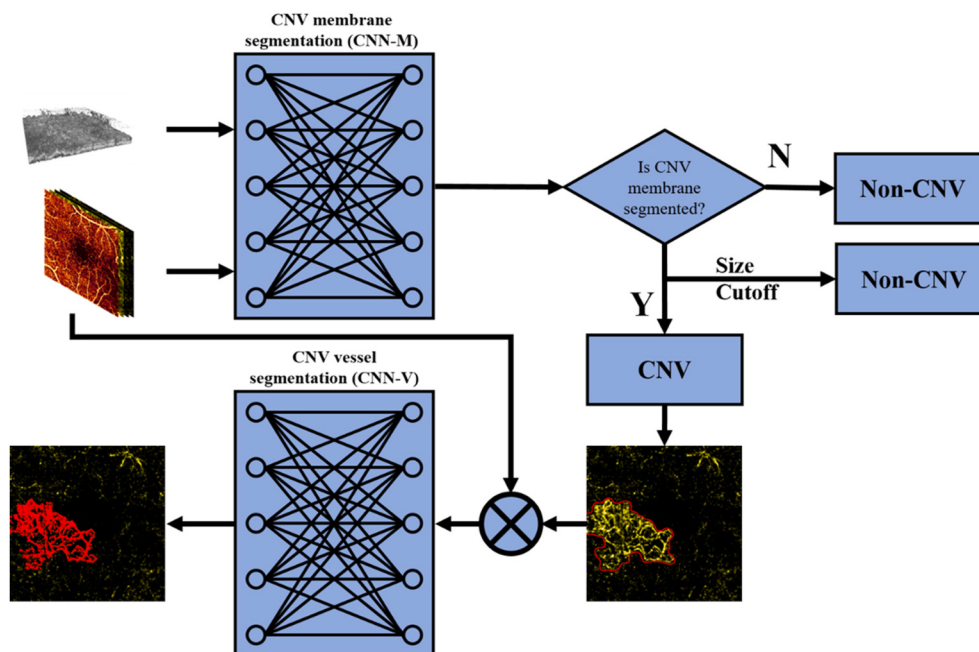


**Fig. 24.** Choroidal neovascularization (CNV) detection algorithm overview (schematic). This deep learning network uses a structural optical coherence tomography (OCT) volume and several en face OCT angiography (OCTA) images as input (top left). The en face OCTA image set consists of en face images processed using different artifact removal approaches, which collectively enable the network to distinguish projection artifacts from CNV with high accuracy. These inputs are fed into a membrane segmentation network, which diagnoses CNV if a membrane above a size cutoff is detected. The segmented membrane is then used as input, along with the en face OCTA image set, as input to a second convolutional neural network that is trained to segment vessels. The resulting algorithm can therefore both detect and segment CNV. Reprinted with permission from Wang et al. (Wang et al., 2020a).

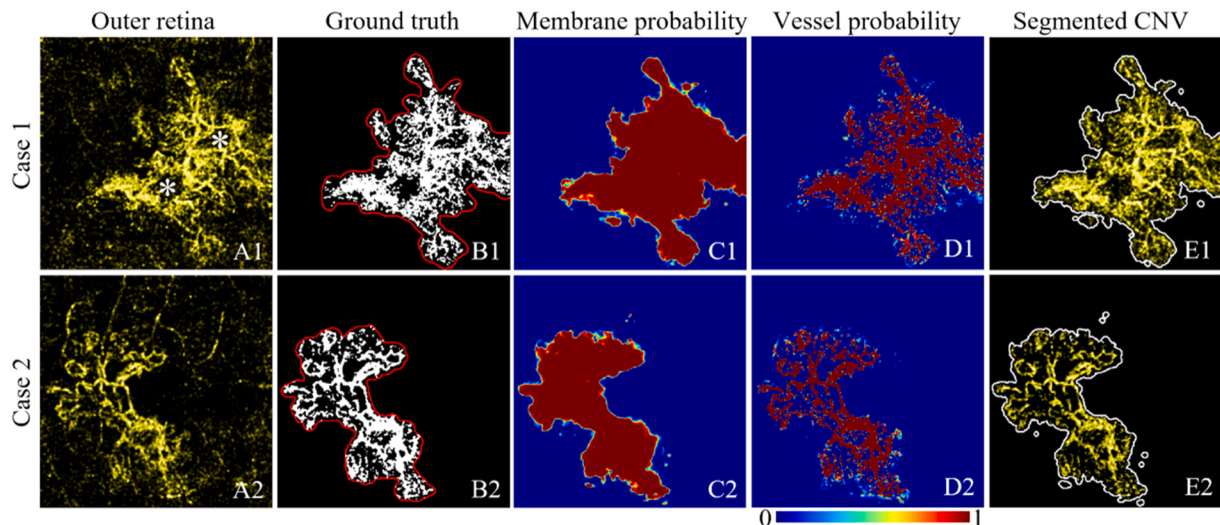


**Fig. 25.** Choroidal neovascularization (CNV) detection and segmentation using deep learning. Each row shows a different case. Column A: Outer retinal optical coherence tomography angiography (OCTA) en face images, showing both CNV lesions and residual projection artifacts. The white asterisks in case 1 show regions with no flow that were still correctly segmented as part of the CNV membrane. Column B: Manually generated ground truth, with the membrane area outlined in red and vessels shown in white. Column C, D: Network probabilities for membrane area and vessels, respectively. The largely binary character of the probability maps indicate that the network has high confidence in its predictions. Column E: Network outputs showing the segmented membrane (white outline) and vessels (yellow). The algorithm ignored residual artifacts and correctly segmented the CNV lesion and vessels. Reprinted with permission from Wang et al. (Wang et al., 2020a). (For interpretation of the references to color in this figure legend, the reader is referred to the Web version of this article.)

trained network then takes the detected lesion as input and segments the CNV vessels. The result is a distinct vessel map that can be used for further quantification (Fig. 25).

The angiofibrotic switch within the lesion in MNV consecutively induces SF, which together with atrophy is the leading cause of irreversible loss in macular function (Toth et al., 2019). To identify baseline predictors for SF, Roberts et al. used OCTA en face images which were quantitatively evaluated for lesion area, vessels area, vessels percentage area, number of junctions, total vessel length, vessel length density, total number of endpoints, mean lacunarity, junction density and endpoint density using the open-source and validated software Angiotool. Additionally, the type of MNV and classic markers for neovascular activity including SRF, IRF, SHRM and retinal hemorrhage at baseline were assessed. After a 12-month follow-up period and a mean of 8.3 ( $\pm 1.6$ ) intravitreal afibbercept injections, 18% of eyes had developed SF. The investigators did not observe a significant difference in any of the quantitative OCTA variables evaluated ( $p > 0.05$ ). However, eyes in the SF group had worse baseline BCVA ( $p = 0.001$ ) and a higher prevalence of IRF and SHRM at baseline (Roberts et al., 2021). Vascular pattern analyses also showed that SF usually originated from the center of MNV growth. This observation closes the loop between fluid-based variables delineated in OCT imaging and the prognosis of nAMD, and illustrates OCTA's potential to become an important imaging support system.

## 6.2. OCTA in diabetic macular and retinal disease

For patients with diabetic retinopathy (DR), DME is a vision-threatening phenotype that triggers anti-VEGF treatment. Capillary damage from hyperglycemia such as retinal ischemia occurs before edema (Darvich et al., 2018), and FA angiographic findings demonstrate that macular ischemia predicts progression to proliferative diabetic retinopathy (Ip et al., 2015). Capillary vasculature information is therefore essential for improving our understanding of DME and for developing targeted treatments. OCTA can distinguish DR severity levels by quantifying non-perfusion areas (NPA) in all plexi (Hwang et al., 2018; 2016a; 2016b; You et al., 2020). NPA is less affected by OCTA signal attenuation than alternative perfusion metrics such as vessel density (Hwang et al., 2018). More interestingly, a recent study has

shown that extrafoveal NPA is significantly associated with disease progression and treatment requirements over a year, providing clinically useful information (You et al., 2020).

NPA segmentation is another task well-suited to AI. Like MNV segmentation, NPA segmentation will be inaccurate if artifacts are not correctly accounted for. In particular, shadowing artifacts can appear similar to capillary dropout. This is a problem that traditional image processing algorithms may struggle with, but CNN can be trained to correctly distinguish shadows from NPA (Guo et al., 2019; Wang et al., 2020b). To do so, these algorithms incorporate both the structural and angiographic OCT signal as inputs (Fig. 26). As shadows darken both the structural and angiographic channels indiscriminately, their combination can be used to differentiate shadows and NPA (which will appear dark only in the OCTA channel). However, even when shadows are correctly identified, NPA quantification can be complicated by the presence of retinal fluid. Fluid pockets will also appear avascular in OCTA, and retinal slabs containing fluid may therefore appear avascular even when vessels still exist outside of the fluid region. One study was able to correlate NPA in the deep capillary plexus with visual acuity in DR patients; however, this correlation was insignificant when eyes with IRF due to DME were excluded (You et al., 2020). This may indicate that the presence of DME should be controlled for when measuring NPA.

Conversely, the fact that fluid pockets appear avascular in OCTA data can support direct quantification of fluid itself. To explore this idea, Guo et al. trained several CNN to segment retinal fluid using a composite image formed by summing structural OCT and OCTA data volumes (Guo et al., 2019). Another advantage of OCTA imaging is that it is automatically registered to structural OCT data, making this addition trivial. By training different models on different weightings of the OCTA data in the composite image, Guo et al. were able to quantify the relative importance of OCTA data in AI decision-making for the fluid segmentation task by comparing the performance of different trained networks. An important conclusion of this work is that OCTA data improved fluid segmentation because a null weighting, which is the same as not including OCTA data at all, underperformed relative to any other weighting. However, the investigators were also able to demonstrate that structural OCT information is still more important as the best performing model trained on an 80/20 OCT/OCTA weighting (Fig. 27).

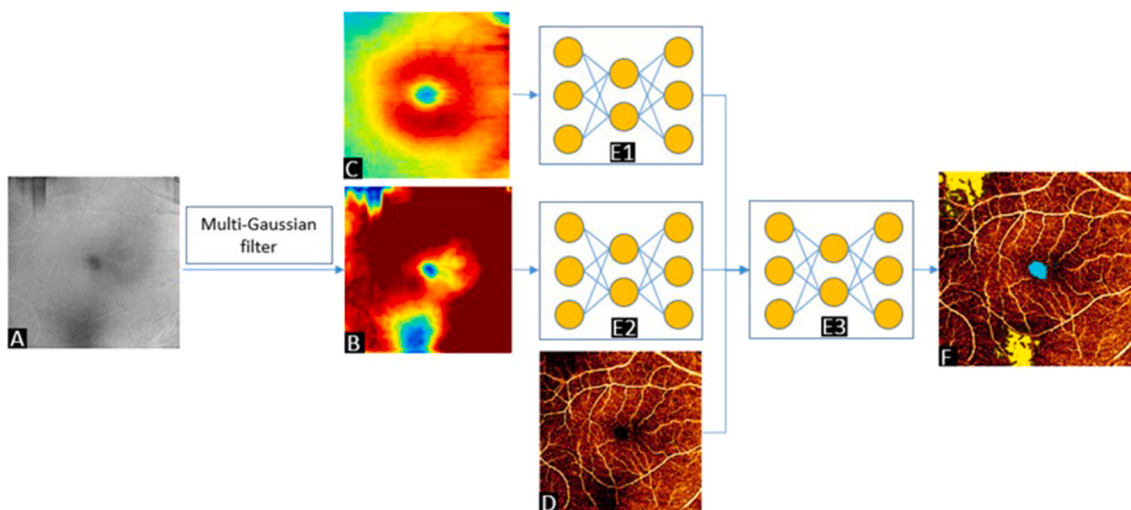


**Fig. 26.** Non-perfusion area (NPA) detection using deep learning. Intelligent choices for network inputs allow the model to learn to distinguish shadowing artifacts from capillary drop out. (A) A structural optical coherence tomography angiography (OCTA) volume is passed through a multi-Gaussian filter (B). The filtered image and a retinal thickness map (C) are passed to separate convolutional neural networks (E1, E2), which are trained to identify shadows. The outputs of these networks along with an en face OCTA image of the same region are then passed to a final convolutional neural network (E3) that segments non-perfusion and shadow artifacts. Reprinted with permission from Guo et al. (Guo et al., 2019).

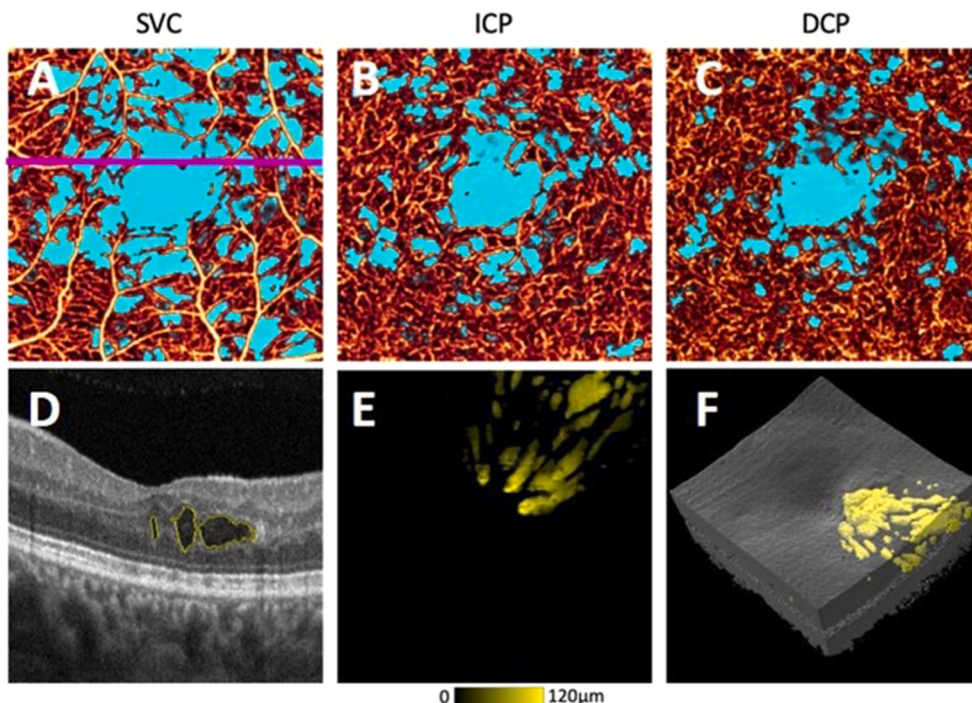


**Fig. 27.** Non-perfusion area (NPA) and retinal fluid detection using deep learning. (A–C)  $3 \times 3$ -mm en face optical coherence tomography angiography (OCTA) images with NPA (teal) automatically segmented by a convolutional neural network (CNN) in three different plexuses (A: Superficial vascular complex (SVC); B: Intermediate capillary plexus (ICP); C: Deep capillary plexus). (D) Cross-sectional image at the location of the magenta line in (A). Retinal fluid is apparent at this location, and can be automatically segmented by a different CNN (yellow outline). (E) Thickness map for the segmented retinal fluid, which indicates that some fluid regions cover a greater depth than others-information that is lost with a simple projection. (F) A volume rendering of the same data helps visualize the location of fluid within the retina. (For interpretation of the references to color in this figure legend, the reader is referred to the Web version of this article.)

## 7. Future directions and conclusions: Beyond fluid and VEGF

Most of the exudative diseases of the macula are chronic and progressive in nature. The destructive course is most obvious in the setting of nAMD and invariably leads to vision loss over time despite continuous therapeutic care. Fluid is a major component of progressive functional loss as concluded from the association of lower treatment frequency, residual and recurrent fluid with worse outcomes in the real world (Mehta et al., 2018). Nevertheless, in the absence of precise and automated fluid quantification such statistics broadly average large populations and do not establish robust cause-effect correlations. A recently reported 10-year follow-up of the Fight Retinal Blindness registry, which

documents routine clinical practice in a standardized manner, highlighted that the cohort treated with a T&E regimen yielded outcomes superior to the PRN cohort (Gillies et al., 2020). T&E reduces the presence of fluid in the retina with proactive intervention, while PRN awaits fluid recurrence and intervenes subsequently, another strong piece of evidence suggesting tight fluid monitoring.

Of note, T&E-treated retinas were indeed mostly dry, but were associated with a higher prevalence of macular atrophy of 41% versus 6% in the PRN group. While retinas in the PRN regimen demonstrated persistent fluid most of the time and developed SF by 78% versus 28% in the T&E group. These competing pathways are still not fully understood. There is the hypothesis that neovascularization evolves as a biological

rescue in type 1 MNV to provide additional nutritional support to the overlying photoreceptors, and intensive fluid resolution could induce involution of the nurturing membrane thereby accelerating macular atrophy (Chen et al., 2020). By contrast, SRF in nAMD contains potent inflammatory cytokines such as the NLRP3 inflammasome, potentially inducing a gliotic and fibrotic response in the subretinal space (Celkova et al., 2015). Alternatively, IRF may reflect a severely disrupted photoreceptor layer and external limiting membrane allowing fluid to enter the neurosensory layers from the underlying MNV (Spaide et al., 2020b).

Lack of a tight correlation between fluid volumes and visual performance in nAMD over long-term observation strongly points towards an important role for neurodegenerative processes. Accordingly, RPE atrophy and photoreceptor loss on OCT were highly predictive of the development of macular atrophy (Finn et al., 2020). As noted previously, GA was shown to be preexisting in about a quarter of MNV eyes before therapy and excessive damage to neurosensory layers was documented by AI-based feature detection on OCT images of patients with intermediate AMD consecutively converting to MNV (Schmidt-Erfurth et al., 2018c). Novel sensitive algorithms are able to identify early signs of neurosensory degeneration, i.e., INL/OPL subsidence (OPL), with focal thinning of the photoreceptor layer and the ONL preceding macular atrophy for as long as 12 months (Rivail et al., 2021). Complement inhibition has recently demonstrated success in slowing the progression of lesion growth (Liao et al., 2020). Interestingly, macular fluid indicative of MNV developed in 20.9% of eyes in the monthly treatment arm, highlighting the common biological path in the dry and wet AMD subtypes. Innovative therapeutic strategies suggest combining anti-VEGF and anti-complement substances or designing bispecific fusion proteins. Sensitive AI tools must complement such experimental interventions into the complex biology of macular disease to recognize resulting effects on a subclinical level. This will strongly apply to irreversible interventions such as gene therapy in multifactorial chronic disease such as AMD or DRP.

Combination approaches are also suggested regarding the various exudative pathways in MNV, DME and RVO. The aim of the combination components is to target other pathognomonic cytokines such as angiopoietin2 for leakage induction (Sahni et al., 2020). More efficient fluid resolution and particularly extended durability with a lower need for retreatment frequency are the goals. With the increasing number of patients affected by MNV and DME, an extended drying effect is the only way to use existing resources for more efficient patient care. Novel drug designs are numerous and a multitude of clinical trials are providing head-to-head comparisons of extended retreatment intervals. Objective measurements of fluid volumes and dynamics have to be provided to allow the community a realistic evaluation, particularly as retreatment criteria vary widely and blend in various functional and morphological components. A clear determination of fluid in a standardized manner is best suited to the identify efficacy and durability of each substance objectively and offer a hands-on diagnostic companion for large-scale use in real-world practice consecutively.

AI-based identification and quantification of subclinical biomarkers will play an important role in screening for patients at risk for developing advanced disease and allow intervention before vision loss occurs. Signs of imminent neovascular conversion were clearly delineated in fellow eyes in the HARBOR trial at one month before conversion (Hu et al., 2020). Such markers included HRF, PED, focal RPE defects, and haze (slightly hyper- or isoreflective changes located between the RPE and inner retinal layers), which were present in the majority of eyes. Areas of external limiting membrane and ellipsoid zone loss significantly increased at the onset of exudation, when IRF and SRF occurred. Another deep learning algorithm recently achieved an 80% per-volumetric-scan sensitivity to predict the conversion to wet AMD within a 6-month time window (Yim et al., 2020). Russakoff et al. introduced a new architecture, AMDnet, as a method for predicting the likelihood of converting from early/intermediate to advanced wet AMD

using OCT imaging and methods of deep learning, and achieved an area under the ROC curve (AUC) of 0.89 at the B-scan level and 0.91 for volumes (Russakoff et al., 2019).

Efficient clinical monitoring of millions of individuals under therapy and early detection by efficient screening in patients at risk are the most successful paths to saving vision. Automated AI tools introducing personalized precision medicine into ophthalmology and identifying a wide spectrum of subclinical markers of disease activity are needed to support physicians and patients in this challenging task.

## Funding sources

Christian Doppler Forschungsgesellschaft, Vienna, Austria.

## CRediT authorship contribution statement

**Ursula Schmidt-Erfurth:** Writing – original draft, Writing – review & editing, Conceptualization. **Gregor S. Reiter:** Writing – original draft, Writing – review & editing. **Sophie Riedl:** Writing – original draft, Writing – review & editing. **Philipp Seeböck:** Writing – original draft, Visualization. **Wolf-Dieter Vogl:** Writing – original draft, Visualization. **Barbara A. Blodi:** Writing – original draft. **Amitha Domalpally:** Writing – original draft. **Amani Fawzi:** Writing – original draft. **Yali Jia:** Writing – original draft. **David Sarraf:** Writing – original draft. **Hrvoje Bogunović:** Writing – original draft, Writing – review & editing, Visualization.

## Acknowledgements

Paulína Šujanova, paulina.sujanova@meduniwien.ac.at, Medical University of Vienna, Vienna, Austria.

## References

- Adjianto, J., Banzon, T., Jalicee, S., Wang, N.S., Miller, S.S., 2009. CO<sub>2</sub>-induced ion and fluid transport in human retinal pigment epithelium. *J. Gen. Physiol.* 133, 603–622. <https://doi.org/10.1085/jgp.200810169>.
- Agarwal, A., 2019. Commentary: hyperreflective dots - an imaging biomarker of inflammation? *Indian J. Ophthalmol.* 67.
- Ahlers, C., Golbaz, I., Stock, G., Fous, A., Kolar, S., Prunte, C., Schmidt-Erfurth, U.M., 2008. Time course of morphologic effects on different retinal compartments after ranibizumab therapy in age-related macular degeneration. *Ophthalmology* 115, e39–e46. <https://doi.org/10.1016/j.ophtha.2008.05.017>.
- Ahn, S.-E., Oh, J., Oh, J.-H., Oh, I.K., Kim, S.-W., Huh, K., 2013. Three-dimensional configuration of subretinal fluid in central serous chorioretinopathy. *Invest. Ophthalmol. Vis. Sci.* 54, 5944. <https://doi.org/10.1167/iovs.13-12279>.
- Aiello, L.P., Beck, R.W., Bressler, N.M., Browning, D.J., Chalam, K.V., Davis, M., Ferris 3rd, F.L., Glassman, A.R., Maturi, R.K., Stockdale, C.R., Topping, T.M., 2011. Rationale for the diabetic retinopathy clinical research network treatment protocol for center-involved diabetic macular edema. *Ophthalmology* 118, e5–14. <https://doi.org/10.1016/j.ophtha.2011.09.058>.
- Alam, M., Zhang, Y., Lim, J.I., Chan, R.V.P., Yang, M., Yao, X., 2020. Quantitative optical coherence tomography angiography features for objective classification and staging of diabetic retinopathy. *Retina* 40, 322–332. <https://doi.org/10.1097/IAE.0000000000002373>.
- American Society of Retina Specialists, 2020. *Global Trends in Retina*.
- Antonetti, D.A., Lieth, E., Barber, A.J., Gardner, T.W., 1999. Molecular mechanisms of vascular permeability in diabetic retinopathy. *Semin. Ophthalmol.* 14 (4), 240–248. <https://doi.org/10.3109/08820539909069543>.
- Bailey, S.T., Thaware, O., Wang, J., Hagag, A.M., Zhang, X., Flaxel, C.J., Lauer, A.K., Hwang, T.S., Lin, P., Huang, D., Jia, Y., 2019. Detection of nonexudative choroidal neovascularization and progression to exudative choroidal neovascularization using OCT angiography. *Ophthalmol. Retin.* 3, 629–636. <https://doi.org/10.1016/j.oret.2019.03.008>.
- Bates, D., Mächler, M., Bolker, B., Walker, S., 2015. Fitting {Linear Mixed}–{Effects models using} lme4. *J. Stat. Software* 67, 1–48. <https://doi.org/10.18637/jss.v067.i01>.
- Beede, E., Baylor, E., Hersch, F., Iurchenko, A., Wilcox, L., Ruamviboonsuk, P., Vardoulakis, L.M., 2020. A human-centered evaluation of a deep learning system deployed in clinics for the detection of diabetic retinopathy. In: Proceedings of the 2020 CHI Conference on Human Factors in Computing Systems, pp. 1–12.
- Bernal-Rusiel, J.L., Greve, D.N., Reuter, M., Fischl, B., Sabuncu, M.R., 2013. Statistical analysis of longitudinal neuroimage data with Linear Mixed Effects models. *NeuroImage* 66, 249–260. <https://doi.org/10.1016/j.neuroimage.2012.10.065>.
- Bilge, M., Prince, J.L., Wong, D.F., Resnick, S.M., Jedyak, B.M., 2016. A multivariate nonlinear mixed effects model for longitudinal image analysis: application to

- amyloid imaging. *Neuroimage* 134, 658–670. <https://doi.org/10.1016/j.neuroimage.2016.04.001>.
- Bland, J., Altman, D., 1986. Statistical methods for assessing agreement between two methods of clinical measurement. *Lancet* 1 (8476), 307–310.
- Bogunović, H., Venhuizen, F., Klimscha, S., Apostolopoulos, S., Bab-Hadiashar, A., Bagci, U., Beg, M.F., Bekalo, L., Chen, Q., Ciller, C., Gopinath, K., Gostar, A.K., Jeon, K., Ji, Z., Kang, S.H., Koozekanani, D.D., Lu, D., Morley, D., Parhi, K.K., Park, H.S., Rashno, A., Sarunic, M., Shaikh, S., Sivaswamy, J., Tennakoon, R., Yadav, S., Zanet, S., De, Waldstein, S.M., Gerendas, B.S., Klaver, C., Sánchez, C.I., Schmidt-Erfurth, U.M., 2018. RETOUCH - the Retinal OCT Fluid Detection and Segmentation Benchmark and Challenge. *IEEE Trans. Med. Imag.* 38, 1858–1874. <https://doi.org/10.1109/TMI.2019.2901398>.
- Bogunovic, H., Waldstein, S.M., Schlegl, T., Langs, G., Sadeghipour, A., Liu, X., Gerendas, B.S., Osborne, A., Schmidt-Erfurth, U.M., 2017. Prediction of anti-VEGF treatment requirements in neovascular AMD using a machine learning approach. *Invest. Ophthalmol. Vis. Sci.* 58, 3240. <https://doi.org/10.1167/iovs.16-21053>.
- Boyer, D., Heier, J., Brown, D.M., Clark, W.L., Vitti, R., Berliner, A.J., Groetzbach, G., Zeitz, O., Sandbrink, R., Zhu, X., Beckmann, K., Haller, J.A., 2012. Vascular endothelial growth factor Trap-Eye for macular edema secondary to central retinal vein occlusion: six-month results of the phase 3 COPERNICUS study. *Ophthalmology* 119, 1024–1032. <https://doi.org/10.1016/j.ophtha.2012.01.042>.
- Boykov, Y., Funka-Lea, G., 2006. Graph cuts and efficient N-D image segmentation. *Int. J. Comput. Vis.* 70, 109–131. <https://doi.org/10.1007/s11263-006-7934-5>.
- Boykov, Y., Veksler, O., Zabih, R., 2001. Fast approximate energy minimization via graph cuts. *IEEE Trans. Pattern Anal. Mach. Intell.* 23, 1222–1239. <https://doi.org/10.1109/34.969114>.
- Bringmann, A., Pannicke, T., Grosche, J., Francke, M., Wiedemann, P., Skatchkov, S.N., Osborne, N.N., Reichenbach, A., 2006. Müller cells in the healthy and diseased retina. *Prog. Retin. Eye Res.* 25, 397–424. <https://doi.org/10.1016/j.preteyes.2006.05.003>.
- Broaddus, V.C., Light, R.W., 1992. What is the origin of pleural transudates and exudates? *Chest*. <https://doi.org/10.1378/chest.102.3.658>.
- Brown, D.M., Kaiser, P.K., Michels, M., Soubrane, G., Heier, J.S., Sy, R.Y., Sy, J.P., Schneider, S., 2006. Ranibizumab versus verteporfin for neovascular age-related macular degeneration. *N. Engl. J. Med.* 355, 1432–1444. <https://doi.org/10.1056/NEJMoa062655>.
- Brown, D.M., Michels, M., Kaiser, P.K., Heier, J.S., Sy, J.P., Ianchulev, T., 2009. Ranibizumab versus verteporfin photodynamic therapy for neovascular age-related macular degeneration: two-year results of the ANCHOR study. *Ophthalmology* 116, 57–65. [https://doi.org/10.1016/j.ophtha.2008.10.018 e5](https://doi.org/10.1016/j.ophtha.2008.10.018).
- Budd, S., Robinson, E.C., Kainz, B., 2019. A Survey on Active Learning and Human-In-The-Loop Deep Learning for Medical Image Analysis arXiv Prepr. *arXiv1910.02923*.
- Camino, A., Jia, Y., Liu, G., Wang, J., Huang, D., 2017. Regression-based algorithm for bulk motion subtraction in optical coherence tomography angiography. *Biomed. Opt. Express* 8, 3053–3066. <https://doi.org/10.1364/BOE.8.003053>.
- Campochiaro, P.A., Akhlag, A., 2020. Sustained suppression of VEGF for treatment of retinal/choroidal vascular diseases. *Prog. Retin. Eye Res.*, 100921 <https://doi.org/10.1016/j.preteyes.2020.100921>. In press.
- Caselles, V., Kimmel, R., Sapiro, G., 1997. Geodesic active contours. *Int. J. Comput. Vis.* 22, 61–79. <https://doi.org/10.1023/A:1007979827043>.
- Celkova, L., Doyle, S.L., Campbell, M., 2015. NLRP3 inflammasome and pathobiology in AMD. *J. Clin. Med.* 4, 172–192. <https://doi.org/10.3390/jcm4010172>.
- Chakravarthy, U., Goldenberg, D., Young, G., Havilio, M., Rafaeli, O., Benyamin, G., Loewenstein, A., 2016. Automated identification of lesion activity in neovascular age-related macular degeneration. *Ophthalmology* 123, 1731–1736.
- Chakravarthy, U., Harding, S.P., Rogers, C.A., Downes, S.M., Lotery, A.J., Wordsworth, S., Reeves, B.C., 2012. Ranibizumab versus bevacizumab to treat neovascular age-related macular degeneration: one-year findings from the IVAN randomized trial. *Ophthalmology* 119, 1399–1411. <https://doi.org/10.1016/j.ophtha.2012.04.015>.
- Chakravarthy, U., Havilio, M., Syntosi, A., Pillai, N., Wilkes, E., Benyamin, G., Best, C., Sagkriotis, A., 2021. Impact of macular fluid volume fluctuations on visual acuity during anti-VEGF therapy in eyes with nAMD. *Eye*. <https://doi.org/10.1038/s41433-020-01354-4>.
- Chakravarthy, U., Pillai, N., Syntosi, A., Barclay, L., Best, C., Sagkriotis, A., 2020. Association between visual acuity, lesion activity markers and retreatment decisions in neovascular age-related macular degeneration. *Eye* 34, 2249–2256. <https://doi.org/10.1038/s41433-020-0799-y>.
- Chen, L., Messinger, J.D., Sloan, K.R., Swain, T.A., Sugiura, Y., Yannuzzi, L.A., Curcio, C.A., Freund, K.B., 2020. Nonexudative macular neovascularization supporting outer retina in age-related macular degeneration: a clinicopathologic correlation. *Ophthalmology* 127, 931–947. <https://doi.org/10.1016/j.ophtha.2020.01.040>.
- Chen, X., Al-Sheikh, M., Chan, C.K., Hariri, A.H., Abraham, P., Lalezary, M., Lin, S.G., Sadda, S., Sarraf, D., 2016. Type 1 versus type 3 neovascularization IN pigment epithelial detachments associated with age-related macular degeneration after anti-vascular endothelial growth factor therapy: a prospective study. *Retina* 36 (Suppl. 1), S50–S64. <https://doi.org/10.1097/IAE.00000000000001271>.
- Chen, X., Kuehlewein, L., Pineles, S.L., Tandon, A.K., Bose, S.X., Klufas, M.A., Sadda, S.R., Sarraf, D., 2015. EN face optical coherence tomography of macular microcysts due to optic neuropathy from neuromyelitis optica. *Retin. Cases Brief Rep.* 9.
- Chen, X., Niemeijer, M., Zhang, L., Lee, K., Abramoff, M.D., Sonka, M., 2012. Three-dimensional segmentation of fluid-associated abnormalities in retinal OCT: probability constrained graph-search-graph-cut. *31*, 1521–1531.
- Cheung, C.M.G., Lai, T.Y.Y., Ruamviboonsuk, P., Chen, S.J., Chen, Y., Freund, K.B., Gomi, F., Koh, A.H., Lee, W.K., Wong, T.Y., 2018. Polypoidal Choroidal Vasculopathy: Definition, Pathogenesis, Diagnosis, and Management. *Ophthalmology* 125 (5), 708–724. <https://doi.org/10.1016/j.ophtha.2017.11.019>.
- Chiu, S.J., Allingham, M.J., Mettu, P.S., Cousins, S.W., Izatt, J.A., Farsiu, S., 2015. Kernel Regression Based Segmentation of Optical Coherence Tomography Images with Diabetic Macular Edema, vol. 6, pp. 1172–1194.
- Chong, V., 2016. Ranibizumab for the treatment of wet AMD: a summary of real-world studies. *Eye* 30, 1526. <https://doi.org/10.1038/eye.2016.202>.
- Çiçek, Ö., Abdulkadir, A., Lienkamp, S.S., Brox, T., Ronneberger, O., 2016. 3D UNet: Learning Dense Volumetric Segmentation from Sparse Annotation, pp. 424–432. [https://doi.org/10.1007/978-3-319-46723-8\\_49](https://doi.org/10.1007/978-3-319-46723-8_49).
- Ciulla, T.A., Bracha, P., Pollack, J., Williams, D.F., 2018. Real-world outcomes of Anti-vascular endothelial growth factor therapy in diabetic macular edema in the United States. *Ophthalmol. Retin.* 2, 1179–1187.
- Cohen, S.Y., Dubois, L., Nghiem-Buffet, S., Ayrault, S., Fajnkuchen, F., Guiberteau, B., Delahaye-Mazza, C., Quentel, G., Tadayoni, R., 2010. Retinal pseudocysts in age-related geographic atrophy. *Am. J. Ophthalmol.* 150, 211–217. [https://doi.org/10.1016/j.ajo.2010.02.019 e1](https://doi.org/10.1016/j.ajo.2010.02.019).
- Coscas, G.J., Lupidi, M., Coscas, F., Cagini, C., Souied, E.H., 2015. Optical coherence tomography angiography versus traditional multimodal imaging in assessing the activity of exudative age-related macular degeneration: a new diagnostic challenge. *Retina* 35, 2219–2228. <https://doi.org/10.1097/IAE.0000000000000076>.
- Daniel, E., Ying, G.S., Kim, B.J., Toth, C.A., Ferris, F., Martin, D.F., Grunwald, J.E., Jaffe, G.J., Dunaief, J.L., Pan, W., Maguire, M.G., 2019. Five-year follow-up of nonfibrotic scars in the comparison of age-related macular degeneration treatments trials. *Ophthalmology* 126, 743–751. <https://doi.org/10.1016/j.ophtha.2018.11.020>.
- Daruich, A., Matet, A., Moulin, A., Kowalcuk, L., Nicolas, M., Sellam, A., Rothschild, P.R., Omri, S., Gélizé, E., Jonet, L., Delaunay, K., De Kozak, Y., Berdugo, M., Zhao, M., Crisanti, P., Behar-Cohen, F., 2018. Mechanisms of macular edema: beyond the surface. *Prog. Retin. Eye Res.* 63, 20–68. <https://doi.org/10.1016/j.preteyes.2017.10.006>.
- Day, S., Acquah, K., Lee, P.P., Mruthyunjaya, P., Sloan, F.A., 2011. Medicare costs for neovascular age-related macular degeneration, 1994–2007. *Am. J. Ophthalmol.* 152, 1014–1020. <https://doi.org/10.1016/j.ajo.2011.05.008>.
- de Azevedo, A.G.B., Takitani, G.E. da S., Godoy, B.R., Marianelli, B.F., Saraiva, V., Tavares, I.M., Roisman, L., 2020. Impact of manual correction over automated segmentation of spectral domain optical coherence tomography. *Int. J. Retin. Vitr.* 6, 4. <https://doi.org/10.1186/s40942-020-0207-6>.
- De Carlo, T.E., Bonini Filho, M.A., Chin, A.T., Adhi, M., Ferrara, D., Baumal, C.R., Witkin, A.J., Reichel, E., Duker, J.S., Waheed, N.K., 2015. Spectral-domain optical coherence tomography angiography of choroidal neovascularization. *Ophthalmology* 122, 1228–1238. <https://doi.org/10.1016/j.ophtha.2015.01.029>.
- De Fauw, J., Ledsam, J.R., Romera-Paredes, B., Nikolov, S., Tomasev, N., Blackwell, S., Askham, H., Glorot, X., O'Donoghue, B., Visentin, D., van den Driessche, G., Lakshminarayanan, B., Meyer, C., Mackinder, F., Bouton, S., Ayoub, K., Chopra, R., King, D., Karthikesalingam, A., Hughes, C.O., Raine, R., Hughes, J., Sim, D.A., Egan, C., Tufail, A., Montgomery, H., Hassabis, D., Rees, G., Back, T., Khaw, P.T., Suleyman, M., Cornebise, J., Keane, P.A., Ronneberger, O., 2018. Clinically applicable deep learning for diagnosis and referral in retinal disease. *Nat. Med.* 24, 1342–1350. <https://doi.org/10.1038/s41591-018-0107-6>.
- de Oliveira Dias, J.R., Zhang, Q., Garcia, J.M.B., Zheng, F., Motulsky, E.H., Roisman, L., Miller, A., Chen, C.L., Kubach, S., de Sisternes, L., Durbin, M.K., Feuer, W., Wang, R.K., Gregori, G., Rosenfeld, P.J., 2018. Natural history of subclinical neovascularization in nonexudative age-related macular degeneration using swept-source OCT angiography. In: *Ophthalmology*. American Academy of Ophthalmology, pp. 255–266. <https://doi.org/10.1016/j.ophtha.2017.08.030>.
- Deák, G.G., Schmidt-Erfurth, U.M., Jampol, L.M., 2018. Correlation of central retinal thickness and visual acuity in diabetic macular edema. *JAMA Ophthalmol.* 136, 1215–1216. <https://doi.org/10.1001/jamaophthalmol.2018.3848>.
- DeCroos, F.C., Toth, C.A., Stinnett, S.S., Heydary, C.S., Burns, R., Jaffe, G.J., Group, C.R., 2012. Optical coherence tomography grading reproducibility during the comparison of age-related macular degeneration treatments trials. *Ophthalmology* 119, 2549–2557. <https://doi.org/10.1016/j.ophtha.2012.06.040>.
- Díaz-Coránguez, M., Ramos, C., Antonetti, D.A., 2017. The inner blood-retinal barrier: cellular basis and development. *Vis. Res.* 139, 123–137. <https://doi.org/10.1016/j.visres.2017.05.009>.
- Domalpally, A., Blodi, B.A., Scott, I.U., Ip, M.S., Oden, N.L., Lauer, A.K., VanVeldhuisen, P.C., 2009. The Standard Care vs Corticosteroid for Retinal Vein Occlusion (SCORE) study system for evaluation of optical coherence tomograms: SCORE study report 4. *Arch. Ophthalmol.* 127, 1461–1467. <https://doi.org/10.1001/archophthalmol.2009.277>.
- Douvali, M., Chatziralli, I.P., Theodossiadis, P.G., Chatzistefanou, K.I., Giannakaki, E., Rouvas, A.A., 2014. Effect of macular ischemia on intravitreal ranibizumab treatment for diabetic macular edema. *Ophthalmologica* 232, 136–143. <https://doi.org/10.1159/000360909>.
- Dugel, Pravin U., Koh, A., Ogura, Y., Jaffe, G.J., Schmidt-Erfurth, U.M., Brown, D.M., Gomes, A.V., Warburton, J., Weichselberger, A., Holz, F.G., 2020a. HAWK and HARRIER: phase 3, multicenter, randomized, double-masked trials of brolucizumab

- for neovascular age-related macular degeneration. *Ophthalmology* 127, 72–84. <https://doi.org/10.1016/j.ophtha.2019.04.017>.
- Dugel, Pravin U., Singh, R.P., Koh, A., Ogura, Y., Weissgerber, G., Gedif, K., Jaffe, G.J., Tadayoni, R., Schmidt-Erfurth, U.M., Holz, F.G., 2020b. HAWK and HARRIER: ninety-six-week outcomes from the phase 3 trials of brolucizumab for neovascular age-related macular degeneration. In: *Ophthalmology*. Elsevier Inc. <https://doi.org/10.1016/j.ophtha.2020.06.028>.
- Ehlers, J., Uchida, A., Sevgi, D., Hu, M., Reed, K., Berliner, A., Vitti, R., Chu, K., Srivastava, S., 2020. Retinal fluid volatility associated with interval tolerance and visual outcomes in diabetic macular edema in the VISTA phase III trial. *Am. J. Ophthalmol.* 224, 217–227. <https://doi.org/10.1016/j.ajo.2020.11.010>.
- Ehlers, J.P., Uchida, A., Hu, M., Figueiredo, N., Kaiser, P.K., Heier, J.S., Brown, D.M., Boyer, D.S., Do, D.V., Gibson, A., Saroj, N., Srivastava, S.K., 2019. Higher-order assessment of OCT in diabetic macular edema from the VISTA study: ellipsoid zone dynamics and the retinal fluid index. *Ophthalmol. Retin.* 3, 1056–1066. <https://doi.org/10.1016/j.oret.2019.06.010>.
- Espina, M., Arcinue, C.A., Ma, F., Camacho, N., Barteselli, G., Mendoza, N., Ferrara, N., Freeman, W.R., 2016. Outer retinal tubulations response to anti-VEGF treatment. *Br. J. Ophthalmol.* 100, 819–823. <https://doi.org/10.1136/bjophthalmol-2015-307141>.
- Evans, R.N., Reeves, B.C., Maguire, M.G., Martin, D.F., Muldrew, A., Peto, T., Rogers, C., Chakravarthy, U., 2020. Associations of variation in retinal thickness with visual acuity and anatomical outcomes in eyes with neovascular age-related macular degeneration lesions treated with anti-vascular endothelial growth factor Agents. *JAMA Ophthalmol.* 138 (10), 1043–1051. <https://doi.org/10.1001/jamaophthalmol.2020.3001>.
- Feng, D., Chen, X., Zhou, Z., Liu, H., Wang, Y., Bai, L., Zhang, S., Mou, X., 2020. A preliminary study of predicting effectiveness of anti-VEGF injection using OCT images based on deep learning. In: 2020 42nd Annual International Conference of the IEEE Engineering in Medicine & Biology Society (EMBC). IEEE, pp. 5428–5431. <https://doi.org/10.1109/EMBC44109.2020.9176743>.
- Fernández, D.C., 2005. Delineating fluid-filled region boundaries in optical coherence tomography images. *Retina* 24, 929–945.
- Finn, A.P., Pistilli, M., Tai, V., Daniel, E., Ying, G.-S., Maguire, M.G., Grunwald, J.E., Martin, D.F., Jaffe, G.J., Toth, C.A., 2020. Localized optical coherence tomography precursors of macular atrophy and fibrotic scar in the comparison of age-related macular degeneration treatments trials. *Am. J. Ophthalmol.* 223, 338–347. <https://doi.org/10.1016/j.ajo.2020.11.002>.
- Folgar, F.A., Jaffe, G.J., Ying, G.-S., Maguire, M.G., Toth, C.A., 2014. Comparison of optical coherence tomography assessments in the comparison of age-related macular degeneration treatments trials. *Ophthalmology* 121, 1956–1965. <https://doi.org/10.1016/j.ophtha.2014.04.020>.
- Fong, Y., Rue, H., Wakefield, J., 2010. Bayesian inference for generalized linear mixed models. *Biostatistics* 11, 397–412. <https://doi.org/10.1093/biostatistics/kxp053>.
- Foot, B., MacEwen, C., 2017. Surveillance of sight loss due to delay in ophthalmic treatment or review: frequency, cause and outcome. *Eye* 31, 771–775.
- Framme, C., Panagakis, G., Walter, A., Gamulescu, M.A., Herrmann, W., Helbig, H., 2012. Interobserver variability for retreatment indications after Ranibizumab loading doses in neovascular age-related macular degeneration. *Acta Ophthalmol.* 90, 49–55.
- Freund, K.B., Korobelnik, J.-F., Devenyi, R., Framme, C., Galic, J., Herbert, E., Hoerauf, H., Lanzetta, P., Michels, S., Mitchell, P., Monés, J., Regillo, C., Tadayoni, R., Talks, J., Wolf, S., 2015. TREAT-AND-EXTEND regimens with anti-vegf agents IN retinal diseases: a literature review and consensus recommendations. *Retina* 35, 1489–1506. <https://doi.org/10.1097/IAE.0000000000000627>.
- Freund, K.B., Straurenghi, G., Zweifel, S., Hill, L., Blotner, S., Tsuboi, M., Gune, S., 2020. Relationship between baseline anatomic lesion type, fluid location, and vision outcomes in the HARBOR clinical trial. In: The Macula Society 43rd Annual Meeting, February 19 - 22 2020. San Diego.
- Funk, M., Karl, D., Georgopoulos, M., Benesch, T., Sacu, S., Polak, K., Zlabiniger, G.J., Schmidt-Erfurth, U.M., 2009. Neovascular age-related macular degeneration: intraocular cytokines and growth factors and the influence of therapy with ranibizumab. *Ophthalmology* 116, 2393–2399. <https://doi.org/10.1016/j.ophtha.2009.05.039>.
- Funk, M., Schmidinger, G., Maar, N., Bolz, M., Benesch, T., Zlabiniger, G.J., Schmidt-Erfurth, U.M., 2010. Angiogenic and inflammatory markers in the intraocular fluid of eyes with diabetic macular edema and influence of therapy with bevacizumab. *Retina* 30, 1412–1419. <https://doi.org/10.1097/IAE.0b013e3181e095c0>.
- Gallemore, R.P., Hughes, B.A., Miller, S.S., 1997. Retinal pigment epithelial transport mechanisms and their contributions to the electroretinogram. *Prog. Retin. Eye Res.* 16 (4), 509–566. [https://doi.org/10.1016/S1350-9462\(96\)00037-7](https://doi.org/10.1016/S1350-9462(96)00037-7).
- Gerendas, B.S., Bogunovic, H., Sadeghipour, A., Schlegl, T., Langs, G., Waldstein, S.M., Schmidt-Erfurth, U.M., 2017. Computational image analysis for prognosis determination in DME. *Vis. Res.* 139, 204–210. <https://doi.org/10.1016/j.vires.2017.03.008>.
- Gerendas, B.S., Prager, S., Deak, G.-G., Simader, C., Lammer, J., Waldstein, S.M., Guerin, T., Kundt, M., Schmidt-Erfurth, U.M., 2018a. Predictive imaging biomarkers relevant for functional and anatomical outcomes during ranibizumab therapy of diabetic macular oedema. *Br. J. Ophthalmol.* 102, 195–203. <https://doi.org/10.1136/bjophthalmol-2017-310483>.
- Gerendas, B.S., Sadeghipour, A., Buehl, W., Sacu, S., Schmidt-Erfurth, U., 2018b. Real world Vienna: the VIBES study - outcomes and procedures in neovascular AMD. *Invest. Ophthalmol. Vis. Sci.* 59, 1621.
- Gerendas, B.S., Sadeghipour, A., Michl, M., Goldbach, F., Mylonas, G., Alten, T., Leingang, O., Sacu, S., Bogunović, H., Schmidt-Erfurth, U.M., 2021. Deep learning-based automated fluid quantification in clinical routine OCT images in neovascular AMD over 5 years. *JAMA Ophthalmology*. In preparation.
- Gillies, M., Arnold, J., Bhandari, S., Essex, R.W., Young, S., Squirrell, D., Nguyen, V., Barthelmes, D., 2020. Ten-year treatment outcomes of neovascular age-related macular degeneration from two regions. *Am. J. Ophthalmol.* 210, 116–124. <https://doi.org/10.1016/j.ajo.2019.10.007>.
- Glassman, A.R., Wells III, J.A., Josic, K., Maguire, M.G., Antoszyk, A.N., Baker, C., Beaulieu, W.T., Elman, M.J., Jampol, L.M., Sun, J.K., 2020. Five-year outcomes after initial aflibercept, bevacizumab, or ranibizumab treatment for diabetic macular edema (protocol T extension study). *Ophthalmology* 127, 1201–1210. <https://doi.org/10.1016/j.ophtha.2020.03.021>.
- Golbaz, I., Ahlers, C., Stock, G., Schütze, C., Schriefl, S., Schlanitz, F., Simader, C., Prünke, C., Schmidt-Erfurth, U.M., 2011. Quantification of the therapeutic response of intraretinal, subretinal, and subpigment epithelial compartments in exudative AMD during anti-VEGF therapy. *Invest. Ophthalmol. Vis. Sci.* 52, 1599. <https://doi.org/10.1167/iows.09-5018>.
- Goodfellow, I.J., Pouget-Abadie, J., Mirza, M., Xu, B., Warde-Farley, D., Ozair, S., Courville, A., Bengio, Y., 2014. Generative Adversarial Networks.
- Gorriz, M., Carlier, A., Faure, E., Giro-i-Nieto, X., 2017. Cost-effective Active Learning for Melanoma Segmentation arXiv Prepr. arXiv1711.09168.
- Grechenig, C., Reiter, G.S., Riedl, S., Arnold, J., Guymer, R., Grenadas, B.S., Bogunovic, H., Schmidt-Erfurth, U.M., 2021. Impact of Residual Subretinal Fluid Volumes on Treatment Outcomes in a SRF-Tolerant Treat & Extend Regimen. <https://doi.org/10.1097/IAE.00000000000003180>. *Retina*.
- Gune, S., Abdelfattah, N.S., Karamat, A., Balasubramanian, S., Marion, K.M., Morgenstien, E., Sadda, S.R., 2020. Spectral-Domain OCT-Based Prevalence and Progression of Macular Atrophy in the HARBOR Study for Neovascular Age-Related Macular Degeneration. *Ophthalmology* 127 (4), 523–532. <https://doi.org/10.1016/j.ophtha.2019.09.030>.
- Guo, Y., Hormel, T.T., Xiong, H., Wang, B., Camino, A., Wang, J., Huang, D., Hwang, T.S., Jia, Y., 2019. Development and validation of a deep learning algorithm for distinguishing the nonperfusion area from signal reduction artifacts on OCT angiography. *Biomed. Opt Express* 10, 3257. <https://doi.org/10.1364/bbe.10.003257>.
- Guo, Y., Hormel, T.T., Xiong, H., Wang, J., Hwang, T.S., Jia, Y., 2020. Automated Segmentation of Retinal Fluid Volumes from Structural and Angiographic Optical Coherence Tomography Using Deep Learning. <https://doi.org/10.1167/tvst.9.2.54> arXiv.
- Guymer, R.H., 2020. Treating neovascular age-related macular degeneration—so much more to learn. *JAMA Ophthalmol.* 138, 1051–1052. <https://doi.org/10.1001/jamaophthalmol.2020.3000>.
- Guymer, R.H., Markey, C.M., McAllister, I.L., Gillies, M.C., Hunyor, A.P., Arnold, J.J., FLUID Investigators, 2019. Tolerating subretinal fluid in neovascular age-related macular degeneration treated with ranibizumab using a treat-and-extend regimen: FLUID study 24-month results. *Ophthalmology* 126, 723–734. <https://doi.org/10.1016/j.ophtha.2018.11.025>.
- Haj Najeeb, B., Simader, C., Deak, G.-G., Vass, C., Gamper, J., Montuoro, A., Gerendas, B.S., Schmidt-Erfurth, U.M., 2017. The distribution of leakage on fluorescein angiography in diabetic macular edema: a new approach to its etiology. *Invest. Ophthalmol. Vis. Sci.* 58, 3986. <https://doi.org/10.1167/iows.17-21510>.
- He, W., Goodkind, D., Kowal, P., 2016. An Aging World. <https://doi.org/10.13140/RG.2.1.1088.9362>.
- Heier, J.S., Brown, D.M., Chong, V., Korobelnik, J.F., Kaiser, P.K., Nguyen, Q.D., Kirchhof, B., Ho, A., Ogura, Y., Yancopoulos, G.D., Stahl, N., Vitti, R., Berliner, A.J., Soo, Y., Anderson, M., Groetzsch, G., Sommerrauer, B., Sandbrink, R., Simader, C., Schmidt-Erfurth, U.M., 2012. Intravitreal aflibercept (VEGF trap-eye) in wet age-related macular degeneration. *Ophthalmology* 119, 2537–2548. <https://doi.org/10.1016/j.ophtha.2012.09.006>.
- Heiferman, M.J., Fawzi, A.A., 2019. Progression of subclinical choroidal neovascularization in age-related macular degeneration. *PloS One* 14, 1–9. <https://doi.org/10.1371/journal.pone.0217805>.
- Hiley, A., Au, A., Freund, K.B., Loewenstein, A., Souied, E.H., Zur, D., Sacconi, R., Borrelli, E., Peiretti, E., Iovino, C., Sugiura, Y., Ellabban, A.A., Monés, J., Waheed, N., K., Ozdek, S., Yalinbas, D., Thiele, S., de Moura Mendonça, L.S., Lee, M.Y., Lee, W.K., Turcotte, P., Capuano, V., Filali Ansary, M., Chakravarthy, U., Lommatsch, A., Gunnemann, F., Pauleikhoff, D., Ip, M.S., Querques, G., Holz, F.G., Spaide, R.F., Sadda, S., Sarraf, D., 2020. Non-neovascular age-related macular degeneration with subretinal fluid. *Br. J. Ophthalmol.* <https://doi.org/10.1136/bjophthalmol-2020-317326>.
- Hiley, A., Au, A., Sadda, S.R., Sarraf, D., 2021. Mechanisms of Fluid Development in AMD Consider the Multiple Pathways when Creating Treatment Plans. *Retin. Physician*.
- Holz, F.G., Figueira, M.S., Bandello, F., Yang, Y., Ohji, M., Dai, H., Wykrota, H., Sharma, S., Dunger-Baldauf, C., Lacey, S., Macfadden, W., Mitchell, P., 2020. Ranibizumab treatment IN treatment-naïve neovascular age-related macular degeneration: results from LUMINOUS, a global real-world study. *Retina* 40, 1673–1685. <https://doi.org/10.1097/IAE.0000000000002670>.
- Holz, F.G., Roider, J., Ogura, Y., Korobelnik, J.-F., Simader, C., Groetzsch, G., Vitti, R., Berliner, A.J., Hiemeyer, F., Beckmann, K., Zeitz, O., Sandbrink, R., 2013. VEGF Trap-Eye for macular oedema secondary to central retinal vein occlusion: 6-month results of the phase III GALILEO study. *Br. J. Ophthalmol.* 97, 278–284. <https://doi.org/10.1136/bjophthalmol-2012-301504>.
- Hopkins, J.J., Keane, P.A., Balaskas, K., 2020. Delivering personalized medicine in retinal care: from artificial intelligence algorithms to clinical application. *Curr. Opin. Ophthalmol.* 31, 329–336.
- Hou, K.K., Au, A., Kashani, A.H., Freund, K.B., Sadda, S.R., Sarraf, D., 2019. Pseudoflow with OCT angiography in eyes with hard exudates and macular drusen. *Transl. Vis. Sci. Technol.* 8, 50. <https://doi.org/10.1167/tvst.8.3.50>.

- Hsieh, Y.T., Alam, M.N., Le, D., Hsiao, C.C., Yang, C.H., Chao, D.L., Yao, X., 2019. OCT angiography biomarkers for predicting visual outcomes after ranibizumab treatment for diabetic macular edema. *Ophthalmol. Retin.* 3, 826–834. <https://doi.org/10.1016/j.joret.2019.04.027>.
- Hsu, J., Regillo, C.D., 2020. Poorer outcomes in real-world studies of anti-vascular endothelial growth factor therapy for neovascular age-related macular degeneration. *Ophthalmol. Eye Health* 127 (9), 1189–1190. <https://doi.org/10.1016/j.ophtha.2020.03.034>.
- Hu, X., Waldstein, S.M., Klimscha, S., Sadeghipour, A., Bogunovic, H., Gerendas, B.S., Osborne, A., Schmidt-Erfurth, U., 2020. Morphological and functional characteristics at the onset OF exudative conversion IN age-related macular degeneration. *Retina* 40, 1070–1078. <https://doi.org/10.1097/IAE.00000000000002531>.
- Hwang, T.S., Gao, S.S., Liu, L., Lauer, A.K., Bailey, S.T., Flaxel, C.J., Wilson, D.J., Huang, D., Jia, Y., 2016a. Automated quantification of capillary nonperfusion using optical coherence tomography angiography in diabetic retinopathy. *JAMA Ophthalmol.* 134, 367–373. <https://doi.org/10.1001/jamaophthalmol.2015.5658>.
- Hwang, T.S., Hagag, A.M., Wang, J., Zhang, M., Smith, A., Wilson, D.J., Huang, D., Jia, Y., 2018. Automated quantification of nonperfusion areas in 3 vascular plexuses with optical coherence tomography angiography in eyes of patients with diabetes. *JAMA Ophthalmol.* 137, 929–936. <https://doi.org/10.1001/jamaophthalmol.2018.2257>.
- Hwang, T.S., Miao, Z., Bhavasar, K., Xinbo, Z., Campbell, J.P., Lin, P., Bailey, S.T., Flaxel, C.J., Lauer, A.K., Wilson, D.J., Huang, D., Jia, Y., 2016b. Visualization of 3 distinct retinal plexuses by projection-resolved optical coherence tomography angiography in diabetic retinopathy. *JAMA Ophthalmol.* 134, 1411–1419. <https://doi.org/10.1001/jamaophthalmol.2016.4272>.
- Ip, M.S., Domalpally, A., Sun, J.K., Ehrlich, J.S., 2015. Long-term effects of therapy with ranibizumab on diabetic retinopathy severity and baseline risk factors for worsening retinopathy. *Ophthalmology* 122, 367–374. <https://doi.org/10.1016/j.ophtha.2014.08.048>.
- Ivanova, E., Alam, N.M., Prusky, G.T., Sagdullaev, B.T., 2019. Blood-retina barrier failure and vision loss in neuron-specific degeneration. *JCI Insight* 4. <https://doi.org/10.1172/jci.insight.126747>.
- Jaffe, G.J., Chakravarthy, U., Freund, K.B., Guymer, R.H., Holz, F.G., Liakopoulos, S., Monés, J.M., Rosenfeld, P.J., Sadda, S.R., Sarraf, D., Schmitz-Valckenberg, S., Spaide, R.F., Staurenghi, G., Tufail, A., Curcio, C.A., 2020. Imaging features associated with progression to geographic atrophy in age-related macular degeneration: CAM report 5. *Ophthalmol. Retin.* <https://doi.org/10.1016/j.joret.2020.12.009>. In press.
- Jaffe, G.J., Martin, D.F., Toth, C.A., Daniel, E., Maguire, M.G., Ying, G.-S., Grunwald, J.E., Huang, J., 2013. Macular morphology and visual acuity in the comparison of age-related macular degeneration treatments trials. *Ophthalmology* 120, 1860–1870. <https://doi.org/10.1016/j.ophtha.2013.01.073>.
- Jaffe, G.J., Ying, G.-S., Toth, C.A., Daniel, E., Grunwald, J.E., Martin, D.F., Maguire, M.G., 2019. Macular morphology and visual acuity in year five of the comparison of age-related macular degeneration treatments trials. *Ophthalmology* 126, 252–260. <https://doi.org/10.1016/j.ophtha.2018.08.035>.
- Jia, Y., Bailey, S.T., Hwang, T.S., Mc Clintic, S.M., Gao, S.S., Pennesi, M.E., Flaxel, C.J., Lauer, A.K., Wilson, D.J., Hornegger, J., Fujimoto, J.G., Huang, D., 2015. Quantitative optical coherence tomography angiography of vascular abnormalities in the living human eye. *Proc. Natl. Acad. Sci. Unit. States Am.* 112, E2395–E2402. <https://doi.org/10.1073/pnas.1500185112>.
- Jia, Y., Bailey, S.T., Wilson, D.J., Tan, O., Klein, M.L., Flaxel, C.J., Potsaid, B., Liu, J.J., Lu, C.D., Kraus, M.F., Fujimoto, J.G., Huang, D., 2014. Quantitative optical coherence tomography angiography of choroidal neovascularization in age-related macular degeneration. *Ophthalmology* 121, 1435–1444. <https://doi.org/10.1016/j.ophtha.2014.01.034>.
- Jia, Y., Tan, O., Tokayer, J., Potsaid, B., Wang, Y., Liu, J.J., Kraus, M.F., Subhash, H., Fujimoto, J.G., Hornegger, J., Huang, D., 2012. Split-spectrum amplitude-decorrelation angiography with optical coherence tomography. *Opt Express* 20, 4710–4725. <https://doi.org/10.1364/OE.20.004710>.
- Johnson, C., 2004. Top scientific visualization research problems. *IEEE Comput. Graph. Appl.* 24, 13–17.
- Keane, P.A., Heussen, F.M., Ouyang, Y., Mokwa, N., Walsh, A.C., Tufail, A., Sadda, S.R., Patel, P.J., 2012. Assessment of differential pharmacodynamic effects using optical coherence tomography in neovascular age-related macular degeneration. *Invest. Ophthalmol. Vis. Sci.* 53, 1152. <https://doi.org/10.1167/iosv.11-8130>.
- Keane, P.A., Liakopoulos, S., Ongchin, S.C., Heussen, F.M., Msutta, S., Chang, K.T., Walsh, A.C., Sadda, S.R., 2008. Quantitative subanalysis of optical coherence tomography after treatment with ranibizumab for neovascular age-related macular degeneration. *Invest. Ophthalmol. Vis. Sci.* 49, 3115. <https://doi.org/10.1167/iosv.08-1689>.
- Keenan, T.D.L., Chakravarthy, U., Loewenstein, A., Chew, E.Y., Schmidt-Erfurth, U.M., 2020a. Automated quantitative assessment of retinal fluid volumes as important biomarkers in neovascular age-related macular degeneration. *Am. J. Ophthalmol.* <https://doi.org/10.1016/j.ajo.2020.12.012>.
- Keenan, T.D.L., Clemons, T.E., Domalpally, A., Elman, M.J., Havilio, M., Agrón, E., Benyamin, G., Chew, E.Y., 2020b. Retinal specialist versus artificial intelligence detection of retinal fluid from OCT: age-related eye disease study 2: 10-year follow-on study. *Ophthalmology* 128, 100–109. <https://doi.org/10.1016/j.ophtha.2020.06.038>.
- Kelly, C.J., Karthikesalingam, A., Suleyman, M., Corrado, G., King, D., 2019. Key challenges for delivering clinical impact with artificial intelligence. *BMC Med.* 17, 195.
- Kendall, A., Gal, Y., 2017. What uncertainties do we need in bayesian deep learning for computer vision?. In: *Advances in Neural Information Processing Systems*, pp. 5574–5584.
- Kermany, D.S., Goldbaum, M., Cai, W., Valentim, C.C.S., Liang, H., Baxter, S.L., McKeown, A., Yang, G., Wu, X., Yan, F., Dong, Justin, Prasadha, M.K., Pei, J., Ting, M.Y.L., Zhu, J., Li, C., Hewett, S., Dong, Jason, Ziyar, I., Shi, A., Zhang, R., Zheng, L., Hou, R., Shi, W., Fu, X., Duan, Y., Huu, V.A.N., Wen, C., Zhang, E.D., Zhang, C.L., Li, O., Wang, X., Singer, M.A., Sun, X., Xu, J., Tafreshi, A., Lewis, M.A., Xia, H., Zhang, K., 2018. Identifying medical diagnoses and treatable diseases by image-based deep learning. *Cell* 172, 1122–1131 e9.
- Khanani, A.M., Skelly, A., Bezlyak, V., Griner, R., Torres, L.R., Sagkriotis, A., 2020. SIERRA-AMD: a retrospective, real-world evidence study of patients with neovascular age-related macular degeneration in the United States. *Ophthalmol. Retin.* 4, 122–133. <https://doi.org/10.1016/j.joret.2019.09.009>.
- Khansari, M.M., O'Neill, W., Lim, J., Shahidi, M., 2017. Method for quantitative assessment of retinal vessel tortuosity in optical coherence tomography angiography applied to sickle cell retinopathy. *Biomed. Opt Express* 8, 3796. <https://doi.org/10.1364/boe.8.003796>.
- Kim, J.M., Cho, H.J., Kim, Y., Jung, S.H., Lee, D.W., Kim, J.W., 2019. Responses of types 1 and 2 neovascularization in age-related macular degeneration to anti-vascular endothelial growth factor treatment: optical coherence tomography angiography analysis. *Semin. Ophthalmol.* 34, 168–176. <https://doi.org/10.1080/08820538.2019.1620791>.
- Kirkby, G.R., Chignell, A.H., 1985. Shifting subretinal fluid in rhegmatogenous retinal detachment. *Br. J. Ophthalmol.* 69, 654–655. <https://doi.org/10.1136/bjo.69.9.654>.
- Kiss, S., Campbell, J., Alimony, A., Shih, V., Serbin, M., LaPrise, A., Wykoff, C.C., 2020. Management and outcomes for neovascular age-related macular degeneration: analysis of United States electronic health records. *Ophthalmology* 127, 1179–1188. <https://doi.org/10.1016/j.jophtha.2020.02.027>.
- Klaassen, I., Van Noorden, C.J.F., Schlingemann, R.O., 2013. Molecular basis of the inner blood-retinal barrier and its breakdown in diabetic macular edema and other pathological conditions. *Prog. Retin. Eye Res.* 34, 19–48. <https://doi.org/10.1016/j.preteyes.2013.02.001>.
- Klinscha, S., Waldstein, S.M., Schlegl, T., Bogunovic, H., Sadeghipour, A., Philip, A.-M., Podkowinski, D., Pablik, E., Zhang, L., Abramoff, M.D., Sonka, M., Gerendas, B.S., Schmidt-Erfurth, U.M., 2017. Spatial correspondence between intraretinal fluid, subretinal fluid, and pigment epithelial detachment in neovascular age-related macular degeneration. *Invest. Ophthalmol. Vis. Sci.* 58, 4039–4048. <https://doi.org/10.1167/iosv.16-20201>.
- Kortüm, K.U., Müller, M., Kern, C., Babenko, A., Mayer, W.J., Kampik, A., Kreutzer, T.C., Priglinger, S., Hirneiss, C., 2017. Using electronic health records to build an ophthalmologic data warehouse and visualize patients' data. *Am. J. Ophthalmol.* 178, 84–93.
- Kraus, M.F., Potsaid, B., Mayer, M.A., Bock, R., Baumann, B., Liu, J.J., Hornegger, J., Fujimoto, J.G., 2012. Motion correction in optical coherence tomography volumes on a per-A-scan basis using orthogonal scan patterns. *Biomed. Opt Express* 3, 1182–1199. <https://doi.org/10.1364/BOE.3.001182>.
- Krizhevsky, A., Sutskever, I., Hinton, G.E., 2012. *ImageNet Classification with Deep Convolutional Neural Networks*, pp. 1097–1105.
- Kuehlewein, L., Bansal, M., Lenis, T.L., Iafe, N.A., Sadda, S.R., Bonini Filho, M.A., De Carlo, T.E., Waheed, N.K., Duker, J.S., Sarraf, D., 2015a. Optical coherence tomography angiography of type 1 neovascularization in age-related macular degeneration. *Am. J. Ophthalmol.* 160, 739–748. <https://doi.org/10.1016/j.ajo.2015.06.030> e2.
- Kuehlewein, L., Dansinghani, K.K., De Carlo, T.E., Filho, M.A.B., Iafe, N.A., Lenis, T.L., Freund, K.B., Waheed, N.K., Duker, J.S., Sadda, S.R., Sarraf, D., 2015b. Optical coherence tomography angiography of type 3 neovascularization secondary to age-related macular degeneration. *Retina* 35, 2229–2235. <https://doi.org/10.1097/IAE.0000000000000835>.
- Kurmann, T., Yu, S., Márquez-Neila, P., Ebneter, A., Zinkernagel, M., Munk, M.R., Wolf, S., Sznitman, R., 2019. Expert-level automated biomarker identification in optical coherence tomography scans. *Sci. Rep.* 9, 1–9.
- Lad, E.M., Hammill, B.G., Qualls, L.G., Wang, F., Cousins, S.W., Curtis, L.H., 2014. Anti-VEGF treatment patterns for neovascular age-related macular degeneration among medicare beneficiaries. *Am. J. Ophthalmol.* 158, 537–543.
- Laird, N., Ware, J., 1982. Random-Effects Models for Longitudinal Data. *Biometrics* 38 (4), 963–974. <https://doi.org/10.2307/2529876>.
- Lalwani, G.A., Rosenfeld, P.J., Fung, A.E., Dubovy, S.R., Michels, S., Feuer, W., Davis, J. L., Flynn, H.W.J., Esquibro, M., 2009. A variable-dosing regimen with intravitreal ranibizumab for neovascular age-related macular degeneration: year 2 of the PrONTO Study. *Am. J. Ophthalmol.* 148, 43–58. <https://doi.org/10.1016/j.ajo.2009.01.024> e1.
- Lanzetta, P., Loewenstein, A., 2017. Fundamental principles of an anti-VEGF treatment regimen: optimal application of intravitreal anti-vascular endothelial growth factor therapy of macular diseases. *Graefes Arch. Clin. Exp. Ophthalmol.* 255, 1259–1273. <https://doi.org/10.1007/s00417-017-3647-4>.
- Lanzetta, P., Mitchell, P., Wolf, S., Veritti, D., 2013. Different antivascular endothelial growth factor treatments and regimens and their outcomes in neovascular age-related macular degeneration: a literature review. *Br. J. Ophthalmol.* 97 (12), 1497–1507. <https://doi.org/10.1136/bjophthalmol-2013-303394>.
- Lee, C.S., Baughman, D.M., Lee, A.Y., 2017a. Deep learning is effective for classifying normal versus age-related macular degeneration OCT images. *Ophthalmol. Retin.* 1, 322–327. <https://doi.org/10.1016/j.joret.2016.12.009>.
- Lee, C.S., Tyring, A.J., Deruyter, N.P., Wu, Y., Rokem, A., Lee, A.Y., 2017b. Deep-learning based, automated segmentation of macular edema in optical coherence tomography. <https://doi.org/10.1364/BOE.8.003440>, 8, 3440–3448.

- Lee, H., Kang, K.E., Chung, H., Kim, H.C., 2019. Three-dimensional analysis of morphologic changes and visual outcomes in diabetic macular edema. *Jpn. J. Ophthalmol.* 63, 234–242. <https://doi.org/10.1007/s10384-019-00657-8>.
- Lee, H., Kang, K.E., Chung, H., Kim, H.C., 2018. Automated segmentation of lesions including subretinal hyperreflective material in neovascular age-related macular degeneration. *Am. J. Ophthalmol.* 191, 64–75. <https://doi.org/10.1016/j.ajo.2018.04.007>.
- Lee, R., Wong, T.Y., Sabanayagam, C., 2015. Epidemiology of diabetic retinopathy, diabetic macular edema and related vision loss. *Eye Vis. (London, England)* 2, 17. <https://doi.org/10.1186/s40662-015-0026-2>.
- Lenis, T.L., Au, A., Hou, K., Govetto, A., Sarraf, D., 2020. Alterations of the foveal central bouquet associated with cystoid macular edema. *Can. J. Ophthalmol.* 55, 301–309. <https://doi.org/10.1016/j.jcjo.2020.01.013>.
- Liao, D.S., Grossi, F.V., El Mehdi, D., Gerber, M.R., Brown, D.M., Heier, J.S., Wykoff, C. C., Singerman, L.J., Abraham, P., Grassmann, F., Nuernberg, P., Weber, B.H.F., Deschatelets, P., Kim, R.Y., Chung, C.Y., Ribeiro, R.M., Hamdani, M., Rosenfeld, P.J., Boyer, D.S., Slakter, J.S., Francois, C.G., 2020. Complement C3 Inhibitor Pegcetacoplan for Geographic Atrophy Secondary to Age-Related Macular Degeneration: A Randomized Phase 2 Trial. *Ophthalmology* 127 (2), 186–195. <https://doi.org/10.1016/j.ophtha.2019.07.011>.
- Lim, Z.W., Lee, M.L., Hsu, W., Wong, T.Y., 2019. Building trust in deep learning system towards automated disease detection. In: Proceedings of the AAAI Conference on Artificial Intelligence, pp. 9516–9521.
- Liú, L., Gao, S.S., Bailey, S.T., Huang, D., Li, D., Jia, Y., 2015. Automated choroidal neovascularization detection algorithm for optical coherence tomography angiography. *Biomed. Opt Express* 6, 3564–3575. <https://doi.org/10.1364/BOE.6.003564>.
- Long, J., Shelhamer, E., Darrell, T., 2015. Fully Convolutional Networks for Semantic Segmentation, pp. 3431–3440. <https://doi.org/10.1109/CVPR.2015.7298965>.
- Lorenzi, M., Filippone, M., Alexander, D.C., Ourselin, S., 2017. Disease Progression Modeling and Prediction through Random Effect Gaussian Processes and Time Transformation arXiv Prepr. [arXiv1701.01668 1–13](https://arxiv.org/abs/1701.01668).
- Lu, D., Heisler, M., Lee, S., Ding, G.W., Navajas, E., Sarunic, M.V., Beg, M.F., 2019. Deep-learning based multiclass retinal fluid segmentation and detection in optical coherence tomography images using a fully convolutional neural network. *Med. Image Anal.* 54, 100–110. <https://doi.org/10.1016/j.media.2019.02.011>.
- Lujan, B.J., Roorda, A., Knighton, R.W., Carroll, J., 2011. Revealing Henle's fiber layer using spectral domain optical coherence tomography. *Invest. Ophthalmol. Vis. Sci.* 52, 1486–1492. <https://doi.org/10.1167/iovs.10-5946>.
- Lumbroso, B., Rispoli, M., Savastano, M.C., 2015. Longitudinal optical coherence tomography-angiography study of type 2 naïve choroidal neovascularization early response after treatment. *Retina* 35, 2242–2251. <https://doi.org/10.1097/IAE.0000000000000879>.
- Maguire, M.G., Martin, D.F., Ying, G.-S., Jaffe, G.J., Daniel, E., Grunwald, J.E., Toth, C. A., Ferris 3rd, F.L., Fine, S.L., 2016. Five-year outcomes with anti-vascular endothelial growth factor treatment of neovascular age-related macular degeneration: the comparison of age-related macular degeneration treatments trials. *Ophthalmology* 123, 1751–1761. <https://doi.org/10.1016/j.ophtha.2016.03.045>.
- Makita, S., Hong, Y., Yamanari, M., Yatagai, T., Yasuno, Y., 2006. Optical coherence angiography. *Opt Express* 14, 7821–7840. <https://doi.org/10.1364/OE.14.007821>.
- Malihi, M., Jia, Y., Gao, S.S., Flaxel, C., Lauer, A.K., Hwang, T., Wilson, D.J., Huang, D., Bailey, S.T., 2017. Optical coherence tomographic angiography of choroidal neovascularization ill-defined with fluorescein angiography. *Br. J. Ophthalmol.* 101, 45–50. <https://doi.org/10.1136/bjophthalmol-2016-309094>.
- Marmor, M.F., 1999. Mechanisms of fluid accumulation in retinal edema. *Doc. Ophthalmol.* 97, 239–249. [https://doi.org/10.1007/978-94-011-4152-9\\_4](https://doi.org/10.1007/978-94-011-4152-9_4).
- Martin, D.F., Maguire, M.G., Fine, S.L., Ying, G., Jaffe, G.J., Grunwald, J.E., Toth, C., Redford, M., Ferris 3rd, F.L., 2012. Ranibizumab and bevacizumab for treatment of neovascular age-related macular degeneration: two-year results. *Ophthalmology* 119, 1388–1398. <https://doi.org/10.1016/j.ophtha.2012.03.053>.
- Martin, D.F., Maguire, M.G., Ying, G., Grunwald, J.E., Fine, S.L., Jaffe, G.J., 2011. Ranibizumab and bevacizumab for neovascular age-related macular degeneration. *N. Engl. J. Med.* 364, 1897–1908. <https://doi.org/10.1056/NEJMoa1102673>.
- McClintic, S.M., Gao, S., Wang, J., Hagag, A., Lauer, A.K., Flaxel, C.J., Bhavasar, K., Hwang, T.S., Huang, D., Jia, Y., Bailey, S.T., 2018. Quantitative evaluation of choroidal neovascularization under pro Re nata anti-vascular endothelial growth factor therapy with OCT angiography. *Ophthalmol. Retin.* 2, 931–941. <https://doi.org/10.1016/j.oret.2018.01.014>.
- Mehta, H., Kim, L.N., Mathis, T., Zalmay, P., Ghanchi, F., Amoaku, W.M., Kodjikian, L., 2020a. Trends in real-world neovascular AMD treatment outcomes in the UK. *Clin. Ophthalmol.* 14, 3331–3342. <https://doi.org/10.2147/OPTH.S275977>.
- Mehta, N., Lee, C.S., Mendonça, L.S.M., Raza, K., Braun, P.X., Duke, J.S., Waheed, N.K., Lee, A.Y., 2020b. Model-to-Data approach for deep learning in optical coherence tomography intraretinal fluid segmentation. *JAMA Ophthalmol.* 138, 1017–1024. <https://doi.org/10.1001/jamaophthalmol.2020.2769>.
- Mehta, H., Tufail, A., Daien, V., Lee, A.Y., Nguyen, V., Ozturk, M., Barthelmes, D., Gillies, M.C., 2018. Real-world outcomes in patients with neovascular age-related macular degeneration treated with intravitreal vascular endothelial growth factor inhibitors. *Prog. Retin. Eye Res.* 65, 127–146. <https://doi.org/10.1016/j.preteyeres.2017.12.002>.
- Mettu, P.S., Allingham, M.J., Cousins, S.W., 2020. Incomplete response to Anti-VEGF therapy in neovascular AMD: exploring disease mechanisms and therapeutic opportunities. *Prog. Retin. Eye Res.* 100906 <https://doi.org/10.1016/j.preteyeres.2020.100906>.
- Michl, M., Fabianska, M., Seeböck, P., Sadeghipour, A., Haj Najeeb, B., Bogunovic, H., Schmidt-Erfurth, U.M., Gerendas, B.S., 2020a. Automated quantification of macular fluid in retinal diseases and their response to anti-VEGF therapy. *Br. J. Ophthalmol.* [bjophthalmol. https://doi.org/10.1136/bjophthalmol-2020-317416](https://doi.org/10.1136/bjophthalmol-2020-317416), 2020-317416.
- Michl, M., Liu, X., Kaider, A., Sadeghipour, A., Gerendas, B.S., Schmidt-Erfurth, U.M., 2020b. The impact of structural optical coherence tomography changes on visual function in retinal vein occlusion. *Acta Ophthalmol.* n/a. <https://doi.org/10.1111/aos.14621>.
- Miere, A., Butori, P., Cohen, S.Y., Semoun, O., Capuano, V., Jung, C., Souied, E.H., 2019. Vascular remodeling of choroidal neovascularization after anti-vascular endothelial growth factor therapy visualized on optical coherence tomography angiography. *Retina* 39, 548–557. <https://doi.org/10.1097/iae.0000000000001964>.
- Mitchell, P., Bandello, F., Schmidt-Erfurth, U.M., Lang, G.E., Massin, P., Schlingensieck, R.O., Sutter, F., Simader, C., Burian, G., Gerstner, O., Weichselberger, A., 2011. The RESTORE study: ranibizumab monotherapy or combined with laser versus laser monotherapy for diabetic macular edema. *Ophthalmology* 118, 615–625. <https://doi.org/10.1016/j.ophtha.2011.01.031>.
- Miyamoto, K., Khosrof, S., Bursell, S.E., Moromizato, Y., Aiello, L.P., Ogura, Y., Adamis, A.P., 2000. Vascular endothelial growth factor (VEGF)-induced retinal vascular permeability is mediated by intercellular adhesion molecule-1 (ICAM-1). *Am. J. Pathol.* 156, 1733–1739. [https://doi.org/10.1016/S0002-9440\(10\)65044-4](https://doi.org/10.1016/S0002-9440(10)65044-4).
- Moraes, G., Fu, D.J., Wilson, M., Khalid, H., Wagner, S.K., Korot, E., Ferraz, D., Faes, L., Kelly, C.J., Spitz, T., Patel, P.J., Balaskas, K., Keenan, T.D.L., Keane, P.A., Chopra, R., 2020. Quantitative analysis of OCT for neovascular age-related macular degeneration using deep learning. *Ophthalmology* 128 (5), 693–705. <https://doi.org/10.1016/j.ophtha.2020.09.025>.
- Moult, E.M., Alibhai, A.Y., Rebhun, C., Lee, B., Ploner, S., Schottenhamml, J., Husvogt, L., Baumal, C.R., Witkin, A.J., Maier, A., Duker, J.S., Rosenfeld, P.J., Waheed, N.K., Fujimoto, J.G., 2020. Spatial Distribution of Choriocapillaris Impairment in Eyes with Choroidal Neovascularization Secondary to Age-Related Macular Degeneration: A Quantitative OCT Angiography Study. *Retina* 40 (3), 428–445. <https://doi.org/10.1097/IAE.0000000000002556>.
- Moult, E., Choi, W., Waheed, N.K., Adhi, M., Lee, B., Lu, C.D., Jayaraman, V., Potsaid, B., Rosenfeld, P.J., Duker, J.S., Fujimoto, J.G., 2014. Ultrahigh-speed swept-source OCT angiography in exudative AMD. *Ophthalmic Surgery. Lasers Imag. Retin.* 45, 496–505. <https://doi.org/10.3928/23258160-20141118-03>.
- Mundt, M., Hong, Y.W., Pliushch, I., Ramesh, V., 2020. A Wholistic View of Continual Learning with Deep Neural Networks: Forgotten Lessons and the Bridge to Active and Open World Learning arXiv Prepr. [arXiv2009.01797](https://arxiv.org/abs/2009.01797).
- Mylonas, G., Ahlers, C., Malamos, P., Golbaz, I., Deak, G., Schuetze, C., Sacu, S., Schmidt-Erfurth, U., 2009. Comparison of retinal thickness measurements and segmentation performance of four different spectral and time domain OCT devices in neovascular age-related macular degeneration. *Br. J. Ophthalmol.* 93, 1453–1460. <https://doi.org/10.1136/bjo.2008.153643>.
- Nagendran, M., Chen, Y., Lovejoy, C.A., Gordon, A.C., Komorowski, M., Harvey, H., Topol, E.J., Ioannidis, J.P.A., Collins, G.S., Maruthappu, M., 2020. Artificial intelligence versus clinicians: systematic review of design, reporting standards, and claims of deep learning studies. *BMJ* 368, m689. <https://doi.org/10.1136/bmj.m689>.
- Nesper, P.L., Soetikno, B.T., Treister, A.D., Fawzi, A.A., 2018. Volume-rendered projection-resolved OCT angiography: 3D lesion complexity is associated with therapy response in wet age-related macular degeneration. *Investig. Ophthalmol. Vis. Sci.* 59, 1944–1952. <https://doi.org/10.1167/ios.17-23361>.
- Nguyen, Q.D., Brown, D.M., Marcus, D.M., Boyer, D.S., Patel, S., Feiner, L., Gibson, A., Sy, J., Rundle, A.C., Hopkins, J.J., Rubio, R.G., Ehrlich, J.S., 2012. Ranibizumab for diabetic macular edema: results from 2 phase III randomized trials: RISE and RIDE. *Ophthalmology* 119, 789–801. <https://doi.org/10.1016/j.ophtha.2011.12.039>.
- Nguyen, H.V., Tan, G.S.W., Tapp, R.J., Mital, S., Ting, D.S.W., Wong, H.T., Tan, C.S., Laude, A., Tai, E.S., Tan, N.C., others, 2016. Cost-effectiveness of a national telemedicine diabetic retinopathy screening program in Singapore. *Ophthalmology* 123, 2571–2580.
- Novosel, J., Vermeer, K.A., de Jong, J.H., Wang, Z., van Vliet, L.J., 2017. Joint segmentation of retinal layers and focal lesions in 3-D OCT data of topologically disrupted. *Retina* 36, 1276–1286. <https://doi.org/10.1109/TMI.2017.2666045>.
- Obermeyer, Z., Emanuel, E.J., 2016. Predicting the future - big data, machine learning, and clinical medicine. *N. Engl. J. Med.* 375, 1216–1219. <https://doi.org/10.1056/NEJMp1606181>.
- Ogura, S., Kurata, K., Hattori, Y., Takase, H., Ishiguro-Oonuma, T., Hwang, Y., Ahn, S., Park, I., Ikeda, W., Kusuhasha, S., Fukushima, Y., Nara, H., Sakai, H., Fujiwara, T., Matsushita, J., Ema, M., Hirashima, M., Minami, T., Shibuya, M., Takakura, N., Kim, P., Miyata, T., Ogura, Y., Uemura, A., 2017. Sustained inflammation after pericyte depletion induces irreversible blood-retina barrier breakdown. *JCI Insight* 2. <https://doi.org/10.1172/jci.insight.90905>.
- Orlando, J.I., Gerendas, B.S., Riedl, S., Grechenig, C., Breger, A., Ehler, M., Waldstein, S. M., Bogunović, H., Schmidt-Erfurth, U.M., 2020. Automated quantification of photoreceptor alteration in macular disease using optical coherence tomography and deep learning. *Sci. Rep.* 10, 5619. <https://doi.org/10.1038/s41598-020-62329-9>.
- Orlando, J.I., Seeböck, P., Bogunović, H., Klimscha, S., Grechenig, C., Waldstein, S.M., Gerendas, B.S., Schmidt-Erfurth, U.M., 2019. U2-net: a Bayesian u-net model with epistemic uncertainty feedback for photoreceptor layer segmentation in pathological oct scans. In: International Symposium on Biomedical Imaging (ISBI), pp. 1441–1445. <https://doi.org/10.1109/ISBI.2019.8759581>.
- Olátor, S., Perdomo, O., González, F., Müller, H., 2017. Training deep convolutional neural networks with active learning for exudate classification in eye fundus images. In: *Intravascular Imaging and Computer Assisted Stenting, and Large-Scale Annotation of Biomedical Data and Expert Label Synthesis*. Springer, pp. 146–154.
- Ouyang, Y., Li, F., Shao, Q., Heussen, F.M., Keane, P.A., Stübiger, N., Sadda, S.R., Pleyer, U., 2015. Subretinal fluid in eyes with active ocular toxoplasmosis observed

- using spectral domain optical coherence tomography. *PLoS One* 10, e0127683. <https://doi.org/10.1371/journal.pone.0127683>.
- Pang, C.E., Freund, K.B., 2014. Ghost maculopathy: an artifact on near-infrared reflectance and MultiColor imaging masquerading as chorioretinal pathology. *Am. J. Ophthalmol.* 158, 171–178. <https://doi.org/10.1016/j.ajo.2014.03.003> e2.
- Paramothayan, N.S., Barron, J., 2002. New criteria for the differentiation between transudates and exudates. *J. Clin. Pathol.* 55, 69–71. <https://doi.org/10.1136/jcp.55.1.69>.
- Parisi, G.I., Kemker, R., Part, J.L., Kanan, C., Wermter, S., 2019. Continual lifelong learning with neural networks: a review. *Neural Network*. 113, 54–71.
- Park, D.Y., Lee, J., Kim, J., Kim, K., Hong, S., Han, S., Kubota, Y., Augustin, H.G., Ding, L., Kim, J.W., Kim, H., He, Y., Adams, R.H., Koh, G.Y., 2017. Plastic roles of pericytes in the blood–retinal barrier. *Nat. Commun.* 8, 15296. <https://doi.org/10.1038/ncomms15296>.
- Patel, J.I., Hykin, P.G., Gregor, Z.J., Boulton, M., Cree, I.A., 2005. Angiopoietin concentrations in diabetic retinopathy. *Br. J. Ophthalmol.* 89, 480–483. <https://doi.org/10.1136/bjo.2004.049940>.
- Patel, R.C., Wang, J., Hwang, T.S., Zhang, M., Gao, S.S., Pennesi, M.E., Bailey, S.T., Lujan, B.J., Wang, X., Wilson, D.J., Huang, D., Jia, Y., 2018. Plexus-specific detection of retinal vascular pathologic conditions with projection-resolved OCT angiography. *Ophthalmol. Retin.* 2, 816–826. <https://doi.org/10.1016/j.joret.2017.11.010>.
- Zur, D., Iglicki, M., Busch, C., Invernizzi, A., Mariussi, M., Loewenstein, A., 2018. OCT Biomarkers as Functional Outcome Predictors in Diabetic Macular Edema Treated with Dexamethasone Implant. *Ophthalmology* 125 (2), 267–275. <https://doi.org/10.1016/j.jophtha.2017.08.031>.
- Pawlloff, M., Bogunović, H., Gruber, A., Michl, M., Riedl, S., Schmidt-Erfurth, U.M., 2021. A systematic correlation of central subfield thickness (CSFT) with retinal fluid volumes quantified by deep learning in the major exudative macular diseases. *Retina*. Submitted for publication.
- Pearce, I., Clemens, A., Brent, M.H., Lu, L., Gallego-Pinazo, R., Minnella, A.M., Creuzot-Garcher, C., Spital, G., Sakamoto, T., Dunger-Baldauf, C., McAllister, I.L., 2020. Real-world outcomes with ranibizumab in branch retinal vein occlusion: the prospective, global, LUMINOUS study. *PLoS One* 15, e0234739. <https://doi.org/10.1371/journal.pone.0234739>.
- Pfister, F., Wang, Y., Schreiter, K., vom Hagen, F., Altvater, K., Hoffmann, S., Deutsch, U., Hammes, H.-P., Feng, Y., 2010. Retinal overexpression of angiopoietin-2 mimics diabetic retinopathy and enhances vascular damages in hyperglycemia. *Acta Diabetol.* 47, 59–64. <https://doi.org/10.1007/s00592-009-0099-2>.
- Plate, K.H., Breier, G., Weich, H.A., Risau, W., 1992. Vascular endothelial growth factor is a potential tumour angiogenesis factor in human gliomas in vivo. *Nature* 359, 845–848. <https://doi.org/10.1038/359845a0>.
- Porcel, J.M., 2010. Pleural effusions from congestive heart failure. *Semin. Respir. Crit. Care Med.* 31, 689–697. <https://doi.org/10.1055/s-0030-1269828>.
- Proust-Lima, C., Séne, M., Taylor, J.M.G., Jacqmin-Gadda, H., 2014. Joint latent class models for longitudinal and time-to-event data: a review. *Stat. Methods Med. Res.* 23, 74–90. <https://doi.org/10.1177/096228021245839>.
- Qayyum, A., Qadir, J., Bilal, M., Al-Fuqaha, A., 2020. Secure and Robust Machine Learning for Healthcare: A Survey arXiv Prepr. arXiv2001.08103.
- Rasti, R., Allingham, M.J., Mettu, P.S., Kavusi, S., Govind, K., Cousins, S.W., Farsiu, S., 2020. Deep learning-based single-shot prediction of differential effects of anti-VEGF treatment in patients with diabetic macular edema. *Biomed. Opt Express* 11, 1139. <https://doi.org/10.1364/BOE.379150>.
- Reichenbach, A., Bringmann, A., 2020. Glia of the human retina. *Glia* 68, 768–796. <https://doi.org/10.1002/glia.23727>.
- Reiter, G.S., Grechenig, C., Vogl, W.-D., Guymer, R.H., Arnold, J.J., Bogunovic, H., Schmidt-Erfurth, U.M., 2020a. Analysis of Fluid Volume and its Impact on Visual Acuity in the FLUID Study as Quantified with Deep Learning. *Retina Publish Ah.* <https://doi.org/10.1097/IAE.0000000000000323>, 2011.
- Reiter, G.S., Told, R., Schranz, M., Baumann, L., Mylonas, G., Sacu, S., Pollreisz, A., Schmidt-Erfurth, U.M., 2020b. Subretinal drusenoid deposits and photoreceptor loss detecting global and local progression of geographic atrophy by SD-OCT imaging. *Investig. Ophthalmol. Vis. Sci.* 61, 11. <https://doi.org/10.1167/iovs.61.6.11>.
- Reumuelle, A., Wassermann, L., Salas, M., Karantonis, M.G., Sacu, S., Georgopoulos, M., Drexler, W., Pircher, M., Pollreisz, A., Schmidt-Erfurth, U.M., 2020. Morphologic and functional assessment of photoreceptors after macula-off retinal detachment with adaptive-optics OCT and micropolarimetry. *Am. J. Ophthalmol.* 214, 72–85. <https://doi.org/10.1016/j.ajo.2019.12.015>.
- Riedl, S., Cooney, L., Grechenig, C., Sadeghipour, A., Pablik, E., Seaman 3rd, J.W., Waldstein, S.M., Schmidt-Erfurth, U.M., 2020. Topographic analysis of photoreceptor loss correlated with disease morphology in neovascular age-related macular degeneration. *Retina* 40, 2148–2157. <https://doi.org/10.1097/IAE.0000000000000271>.
- Riedl, S., Vogl, W.-D., Waldstein, S.M., Schmidt-Erfurth, U.M., Bogunović, H., 2021. Correlation of functional loss and recovery with fluid volumes quantified by deep learning during therapy of neovascular AMD. *Retina*. In press.
- Rivail, A., Reiter, G.S., Riedl, S., Mai, J., Vogl, W.-D., Grechenig, C., Wu, Z., Guymer, R.H., Schmidt-Erfurth, U.M., Bogunović, H., 2021. Topographic Conversion Model of Outer Retinal Atrophy Progression in Intermediate Age-Related Macular Degeneration Using Deep Learning. To Appear ARVO 2021.
- Rizopoulos, D., Taylor, J.M.G., Van Rosmalen, J., Steyerberg, E.W., Takkenberg, J.J.M., 2016. Personalized screening intervals for biomarkers using joint models for longitudinal and survival data. *Biostatistics* 17, 149–164. <https://doi.org/10.1093/biostatistics/kxv031>.
- Rizzolo, L., 2007. Development and role of tight junctions in the retinal pigment epithelium. *Int. Rev. Cytol.* 258, 195–234. [https://doi.org/10.1016/S0074-7696\(07\)58004-6](https://doi.org/10.1016/S0074-7696(07)58004-6).
- Roberts, P.K., Schranz, M., Motschi, A., Desissaire, S., Hacker, V., Pircher, M., Sacu, S., Buehl, W., Hitzenberger, C.K., Schmidt-Erfurth, U.M., 2021. Morphologic and microvascular differences between macular neovascularization with and without subretinal fibrosis. *Transnational vision science & technology*. Submitted for publication.
- Roberts, P.K., Vogl, W.-D., Gerendas, B.S., Glassman, A.R., Bogunovic, H., Jampol, L.M., Schmidt-Erfurth, U.M., 2020. Quantification of fluid resolution and visual acuity gain in patients with diabetic macular edema using deep learning: a post hoc analysis of a randomized clinical trial. *JAMA Ophthalmol.* 138, 945–953. <https://doi.org/10.1001/jamaophthalmol.2020.2457>.
- Roberts, P.K., Zotter, S., Montuoro, A., Pircher, M., Baumann, B., Ritter, M., Hitzenberger, C.K., Schmidt-Erfurth, U.M., 2019. Identification and quantification of the angiofibrotic switch in neovascular AMD. *Invest. Ophthalmol. Vis. Sci.* 60, 304. <https://doi.org/10.1167/iovs.18-25189>.
- Roberts, W.G., Palade, G.E., 1995. Increased microvascular permeability and endothelial fenestration induced by vascular endothelial growth factor. *J. Cell Sci.* 108, 2369–2379.
- Röhlig, M., Prakasam, R.K., Stüwe, J., Schmidt, C., Stachs, O., Schumann, H., 2019. Enhanced grid-based visual analysis of retinal layer thickness with optical coherence tomography. *Information* 10, 266.
- Romo-Bucheli, D., Erfurth, U.S., Bogunovic, H., 2020a. End-to-End deep learning model for predicting treatment requirements in neovascular AMD from longitudinal retinal OCT imaging. *IEEE J. Biomed. Heal. Inform.* 24, 3456–3465. <https://doi.org/10.1109/JBHI.2020.3000136>.
- Romo-Bucheli, D., Seeböck, P., Orlando, J.I., Gerendas, B.S., Waldstein, S.M., Schmidt-Erfurth, U.M., Bogunovic, H., 2020b. Reducing image variability across OCT devices with unsupervised unpaired learning for improved segmentation of retina. *Biomed. Opt Express* 11, 346. <https://doi.org/10.1364/boe.379978>.
- Ronneberger, O., Fischer, P., Brox, T., 2015. U-net: Convolutional Networks for Biomedical Image Segmentation, pp. 234–241.
- Rosenfeld, P.J., 2016. Optical coherence tomography and the development of antiangiogenic therapies in neovascular age-related macular degeneration. *Investig. Ophthalmol. Vis. Sci.* 57, OCT14. <https://doi.org/10.1167/iovs.16-19969>.
- Rosenfeld, P.J., Brown, D.M., Heier, J.S., Boyer, D.S., Kaiser, P.K., Chung, C.Y., Kim, R.Y., 2006. Ranibizumab for neovascular age-related macular degeneration. *N. Engl. J. Med.* 355, 1419–1431. <https://doi.org/10.1056/nejmoa054481>.
- Russakoff, D.B., Lamin, A., Oakley, J.D., Dubis, A.M., Sivaprasad, S., 2019. Deep learning for prediction of AMD progression: a pilot study. *Invest. Ophthalmol. Vis. Sci.* 60, 712–722. <https://doi.org/10.1167/iovs.18-25325>.
- Russakovskiy, O., Deng, J., Su, H., Krause, J., Sathesh, S., Ma, S., Huang, Z., Karpathy, A., Khosla, A., Bernstein, M., Berg, A.C., Fei-Fei, L., 2015. ImageNet large scale visual recognition challenge. *Int. J. Comput. Vis.* 115, 211–252. <https://doi.org/10.1007/s11263-015-0816-y>.
- Sahni, J., Dugel, P.U., Patel, S.S., Chittum, M.E., Berger, B., del Valle Rubido, M., Sadikhov, S., Szczesny, P., Schwab, D., Nogoseki, E., Weikert, R., Fauser, S., 2020. Safety and Efficacy of Different Doses and Regimens of Faricimab vs Ranibizumab in Neovascular Age-Related Macular Degeneration. *JAMA Ophthalmology* 138 (9), 1–10. <https://doi.org/10.1001/jamaophthalmol.2020.2685>.
- Sahni, J., Patel, S.S., Dugel, P.U., Khanani, A.M., Jhaveri, C.D., Wykoff, C.C., Hersherberger, V.S., Pauly-Evers, M., Sadikhov, S., Szczesny, P., Schwab, D., Nogoseki, E., Osborne, A., Weikert, R., Fauser, S., 2019. Simultaneous inhibition of angiopoietin-2 and vascular endothelial growth factor-A with faricimab in diabetic macular edema: BOULEVARD phase 2 randomized trial. *Ophthalmology* 126, 1155–1170. <https://doi.org/10.1016/j.ophtha.2019.03.023>.
- Schiratti, J., 2017. Methods and Algorithms to Learn Spatio-Temporal Changes from Longitudinal Manifold-Valued Observations to Cite This Version : HAL Id : Tel-01512319 Jean-Baptiste SCHIRATTI.
- Schlegl, T., Seeböck, P., Waldstein, S.M., Langs, G., Schmidt-Erfurth, U.M., 2019. f-AnoGAN: fast unsupervised anomaly detection with generative adversarial networks. *Med. Image Anal.* 54, 30–44. <https://doi.org/10.1016/j.media.2019.01.010>.
- Schlegl, T., Seeböck, P., Waldstein, S.M., Schmidt-Erfurth, U.M., Langs, G., 2017. Unsupervised anomaly detection with generative adversarial networks to guide marker discovery. In: International Conference on Information Processing in Medical Imaging (IPMI). Springer, Cham, pp. 146–147.
- Schlegl, T., Waldstein, S.M., Bogunovic, H., Endstraer, F., Sadeghipour, A., Philip, A.M., Podkowinski, D., Gerendas, B.S., Langs, G., Schmidt-Erfurth, U.M., 2018. Fully automated detection and quantification of macular fluid in OCT using deep learning. *Ophthalmology* 125, 549–558. <https://doi.org/10.1016/j.ophtha.2017.10.031>.
- Schlegl, T., Waldstein, S.M., Vogl, W.D., Schmidt-Erfurth, U.M., Langs, G., 2015. Predicting semantic descriptions from medical images with convolutional neural networks. In: Information Processing in Medical Imaging (IPMI), pp. 437–448. [https://doi.org/10.1007/978-3-319-19992-4\\_34](https://doi.org/10.1007/978-3-319-19992-4_34).
- Schmidt-Erfurth, U.M., Bogunovic, H., Sadeghipour, A., Schlegl, T., Langs, G., Gerendas, B.S., Osborne, A., Waldstein, S.M., 2018a. Machine learning to analyze the prognostic value of current imaging biomarkers in neovascular age-related macular degeneration. *Ophthalmol. Retin.* 2, 24–30. <https://doi.org/10.1016/j.oret.2017.03.015>.
- Schmidt-Erfurth, U.M., Chong, V., Loewenstein, A., Larsen, M., Souied, E., Schlingemann, R., Eldem, B., Monés, J., Richard, G., Bandello, F., 2014a. Guidelines for the management of neovascular age-related macular degeneration by the European Society of Retina Specialists (EURETINA). *Br. J. Ophthalmol.* 98, 1144–1167. <https://doi.org/10.1136/bjophthalmol-2014-305702>.
- Schmidt-Erfurth, U.M., Eldem, B., Guymar, R., Korobelnik, J.F., Schlingemann, R.O., Axer-Siegel, R., Wiedemann, P., Simader, C., Gekkieva, M., Weichselberger, A., 2011. Efficacy and safety of monthly versus quarterly ranibizumab treatment in

- neovascular age-related macular degeneration: the EXCITE study. *Ophthalmology* 118, 831–839. <https://doi.org/10.1016/j.ophtha.2010.09.004>.
- Schmidt-Erfurth, U.M., Garcia-Arumí, J., Bandello, F., Berg, K., Chakravarthy, U., Gerendas, B.S., Jonas, J., Larsen, M., Tadayoni, R., Loewenstein, A., 2017a. Guidelines for the management of diabetic macular edema by the European society of retina specialists (EURETINA). *Ophthalmol. J. Int. d'ophtalmologie. Int. J. Ophthalmol. Zeitschrift für Augenheilkd.* 237, 185–222. <https://doi.org/10.1159/000458539>.
- Schmidt-Erfurth, U.M., Kaiser, P.K., Korobelnik, J.-F., Brown, D.M., Chong, V., Nguyen, Q.D., Ho, A.C., Ogura, Y., Simader, C., Jaffe, G.J., Slakter, J.S., Yancopoulos, G.D., Stahl, N., Vitti, R., Berliner, A.J., Soo, Y., Andereis, M., Sowade, O., Zeitz, O., Norenberg, C., Sandbrink, R., Heier, J.S., 2014b. Intravitreal afiblispercept injection for neovascular age-related macular degeneration: ninety-six-week results of the VIEW studies. *Ophthalmology* 121, 193–201. <https://doi.org/10.1016/j.ophtha.2013.08.011>.
- Schmidt-Erfurth, U.M., Klimscha, S., Waldstein, S.M., Bogunović, H., 2017b. A view of the current and future role of optical coherence tomography in the management of age-related macular degeneration. *Eye* 31, 26–44. <https://doi.org/10.1038/eye.2016.227>.
- Schmidt-Erfurth, U.M., Michl, M., 2019. Disorganization of retinal inner layers and the importance of setting boundaries. *JAMA Ophthalmol.* 137, 46–47. <https://doi.org/10.1001/jamaophthalmol.2018.4516>.
- Schmidt-Erfurth, U.M., Mulyukov, Z., Gerendas, B.S.S., Margaron, P., Lorand, D., Bogunovic, H., Weissgerber, G., 2020a. A comparison of the therapeutic response between brolucizumab and afiblispercept in the HAWK & HARRIER trials using deep learning-based OCT analysis. *Invest. Ophthalmol. Vis. Sci.* 61, 1159.
- Schmidt-Erfurth, U.M., Sadeghipour, A., Gerendas, B.S., Waldstein, S.M., Bogunović, H., 2018b. Artificial intelligence in retina. *Prog. Retin. Eye Res.* 67, 1–29. <https://doi.org/10.1016/j.preteyeres.2018.07.004>.
- Schmidt-Erfurth, U.M., Vogl, W.-D., Jampol, L.M., Bogunović, H., 2020b. Application of automated quantification of fluid volumes to anti-VEGF therapy of neovascular age-related macular degeneration. *Ophthalmology* 127, 1211–1219. <https://doi.org/10.1016/j.ophtha.2020.03.010>.
- Schmidt-Erfurth, U.M., Waldstein, S.M., 2016. A paradigm shift in imaging biomarkers in neovascular age-related macular degeneration. *Prog. Retin. Eye Res.* 50, 1–24. <https://doi.org/10.1016/j.preteyeres.2015.07.007>.
- Schmidt-Erfurth, U.M., Waldstein, S.M., Deak, G.-G., Kundi, M., Simader, C., 2015. Pigment epithelial detachment followed by retinal cystoid degeneration leads to vision loss in treatment of neovascular age-related macular degeneration. *Ophthalmology* 122, 822–832. <https://doi.org/10.1016/j.ophtha.2014.11.017>.
- Schmidt-Erfurth, U.M., Waldstein, S.M., Klimscha, S., Sadeghipour, A., Hu, X., Gerendas, B.S., Osborne, A., Bogunović, H., 2018c. Prediction of individual disease conversion in early AMD using artificial intelligence. *Investig. Ophthalmol. Vis. Sci.* 59, 3199–3208. <https://doi.org/10.1167/iovs.18-24106>.
- Schreur, V., de Breuk, A., Venhuizen, F.G., Sánchez, C.I., Tack, C.J., Klevering, B.J., de Jong, E.K., Hoyng, C.B., 2020. Retinal hyperreflective FOCI in type 1 diabetes mellitus. *Retina* 40, 1565–1573. <https://doi.org/10.1097/IAE.0000000000002626>.
- Seeböck, P., Orlando, J.I., Schlegl, T., Waldstein, S.M., Bogunovic, H., Klimscha, S., Langs, G., Schmidt-Erfurth, U.M., 2020. Exploiting epistemic uncertainty of anatomy segmentation for anomaly detection in retinal OCT. *IEEE Trans. Med. Imag.* 39, 87–98. <https://doi.org/10.1109/TMI.2019.2919951>.
- Seeböck, P., Vogl, W.-D., Waldstein, S.M., Baratsits, M., Orlando, J.I., Alten, T., Bogunovic, H., Arikan, M., Mylonas, G., Schmidt-Erfurth, U.M., 2019a. Linking function and structure: prediction of retinal sensitivity in AMD from OCT using deep learning. *Invest. Ophthalmol. Vis. Sci.* 60, 1534–1534.
- Seeböck, P., Waldstein, S.M., Klimscha, S., Bogunovic, H., Schlegl, T., Gerendas, B.S., Donner, R., Schmidt-Erfurth, U.M., Langs, G., 2019b. Unsupervised identification of disease marker candidates in retinal OCT imaging data. *IEEE Trans. Med. Imag.* 38, 1037–1047. <https://doi.org/10.1109/TMI.2018.2877080>.
- Sethian, J.A., 1999. Level Set Methods and Fast Marching Methods: Evolving Interfaces in Computational Geometry, Fluid Mechanics, Computer Vision, and Materials Science. Cambridge University Press.
- Sharma, A., Kumar, N., Singh, S., Regillo, C.D., Freund, K.B., 2020. Management of fluid in neovascular age-related macular degeneration: to mop it, to dab it, or to leave it? *Retina* 40, 1451–1455. <https://doi.org/10.1097/IAE.0000000000002870>.
- Sharma, S., Toth, C.A., Daniel, E., Grunwald, J.E., Maguire, M.G., Ying, G.-S., Huang, J., Martin, D.F., Jaffe, G.J., 2016. Macular morphology and visual acuity in the second year of the comparison of age-related macular degeneration treatments trials. *Ophthalmology* 123, 865–875. <https://doi.org/10.1016/j.ophtha.2015.12.002>.
- Sikorav, A., Semoun, O., Zweifel, S., Jung, C., Srour, M., Querques, G., Souied, E.H., 2017. Prevalence and quantification of geographic atrophy associated with newly diagnosed and treatment-naïve exudative age-related macular degeneration. *Br. J. Ophthalmol.* 101 <https://doi.org/10.1136/bjophthalmol-2015-308065>, 438 LP – 444.
- Silva, R., Berta, A., Larsen, M., Macfadden, W., Feller, C., Monés, J., 2018. Treat-and-Extend versus monthly regimen in neovascular age-related macular degeneration: results with ranibizumab from the TREND study. *Ophthalmology* 125, 57–65. <https://doi.org/10.1016/j.ophtha.2017.07.014>.
- Simader, C., Ritter, M., Bolz, M., Deák, G.G., Mayr-Sponer, U., Golbaz, I., Kundi, M., Schmidt-Erfurth, U.M., 2014. Morphologic parameters relevant for visual outcome during anti-angiogenic therapy of neovascular age-related macular degeneration. *Ophthalmology* 121, 1237–1245. <https://doi.org/10.1016/j.ophtha.2013.12.029>.
- Simonyan, K., Zisserman, A., 2014. Very Deep Convolutional Networks for Large-Scale Image Recognition arXiv.
- Sophie, R., Lu, N., Campochiaro, P.A., 2015. Predictors of functional and anatomic outcomes in patients with diabetic macular edema treated with ranibizumab. *Ophthalmology* 122, 1395–1401. <https://doi.org/10.1016/j.ophtha.2015.02.036>.
- Spaide, R.F., 2018. Improving the age-related macular degeneration construct. *Retina* 38, 891–899. <https://doi.org/10.1097/IAE.0000000000001732>.
- Spaide, R.F., 2016. RETINAL VASCULAR CYSTOID MACULAR EDEMA: Review and New Theory, vol. 36. RETINA.
- Spaide, R.F., 2008. Autofluorescence from the outer retina and subretinal space: hypothesis and review. *Retina* 28, 5–35. <https://doi.org/10.1097/IAE.0b013e318158eca4>.
- Spaide, R.F., Jaffe, G.J., Sarraf, D., Freund, K.B., Sadda, S.R., Staurenghi, G., Waheed, N. K., Chakravarthy, U., Rosenfeld, P.J., Holz, F.G., Souied, E.H., Cohen, S.Y., Querques, G., Ohno-Matsui, K., Boyer, D., Gaudric, A., Blodi, B., Baumal, C.R., Li, X., Coscas, G.J., Brucker, A., Singerman, L., Luthert, P., Schmitz-Valckenberg, S., Schmidt-Erfurth, U., Grossniklaus, H.E., Wilson, D.J., Guymer, R., Yannuzzi, L.A., Chew, E.Y., Csaky, K., Monés, J.M., Pauleikhoff, D., Tadayoni, R., Fujimoto, J., 2020a. Consensus nomenclature for reporting neovascular age-related macular degeneration data: consensus on neovascular age-related macular degeneration nomenclature study group. *Ophthalmology* 127, 616–636. <https://doi.org/10.1016/j.ophtha.2019.11.004>.
- Spaide, R.F., Jaffe, G.J., Sarraf, D., Freund, K.B., Sadda, S.R., Staurenghi, G., Waheed, N. K., Chakravarthy, U., Rosenfeld, P.J., Holz, F.G., Souied, E.H., Cohen, S.Y., Querques, G., Ohno-Matsui, K., Boyer, D., Gaudric, A., Blodi, B., Baumal, C.R., Li, X., Coscas, G.J., Brucker, A., Singerman, L., Luthert, P., Schmitz-Valckenberg, S., Schmidt-Erfurth, U., Grossniklaus, H.E., Wilson, D.J., Guymer, R., Yannuzzi, L.A., Chew, E.Y., Csaky, K., Monés, J.M., Pauleikhoff, D., Tadayoni, R., Fujimoto, J., 2020b. Consensus nomenclature for reporting neovascular age-related macular degeneration data: consensus on neovascular age-related macular degeneration nomenclature study group. *Ophthalmology* 127, 616–636. <https://doi.org/10.1016/j.ophtha.2019.11.004>.
- Sun, J.K., Lin, M.M., Lammer, J., Prager, S., Sarangi, R., Silva, P.S., Aiello, L.P., 2014. Disorganization of the retinal inner layers as a predictor of visual acuity in eyes with center-involved diabetic macular edema. *JAMA Ophthalmol.* 132, 1309–1316. <https://doi.org/10.1001/jamaophthalmol.2014.2350>.
- Taylor, D.J., Hobby, A.E., Binns, A.M., Crabb, D.P., 2016. How does age-related macular degeneration affect real-world visual ability and quality of life? A systematic review. *BMJ Open* 6, e011504. <https://doi.org/10.1136/bmjopen-2016-011504>.
- Terry, L., Cassels, N., Liu, K., Acton, J.H., Margrain, T.H., North, R.V., Ferguson, J., White, N., Wood, A., 2016. Automated retinal layer segmentation using spectral domain optical coherence tomography: evaluation of inter-session repeatability and agreement between devices. *PLoS One* 11, e0162001.
- Ting, D.S.W., Peng, L., Varadarajan, A.V., Keane, P.A., Burlina, P.M., Chiang, M.F., Schmetterer, L., Pasquale, L.R., Bressler, N.M., Webster, D.R., others, 2019. Deep learning in ophthalmology: the technical and clinical considerations. *Prog. Retin. Eye Res.* 72, 100759.
- Tolentino, M., 2009. Current molecular understanding and future treatment strategies for pathologic ocular neovascularization. *Curr. Mol. Med.* 9, 973–981. <https://doi.org/10.2174/156652409789712783>.
- Tolentino, M.J., Miller, J.W., Gragoudas, E.S., Jakobiec, F.A., Flynn, E., Chatzistefanou, K., Ferrara, N., Adamis, A.P., 1996. Intravitreous injections of vascular endothelial growth factor produce retinal ischemia and microangiopathy in an adult primate. *Ophthalmology* 103, 1820–1828. [https://doi.org/10.1016/s0161-6420\(96\)30420-x](https://doi.org/10.1016/s0161-6420(96)30420-x).
- Tonade, D., Kern, T.S., 2020. Photoreceptor cells and RPE contribute to the development of diabetic retinopathy. *Prog. Retin. Eye Res.* <https://doi.org/10.1016/j.preteyeres.2020.100919>. In press.
- Tonade, D., Liu, H., Palczewski, K., Kern, T.S., 2017. Photoreceptor cells produce inflammatory products that contribute to retinal vascular permeability in a mouse model of diabetes. *Diabetologia* 60, 2111–2120. <https://doi.org/10.1007/s00125-017-4381-5>.
- Toth, C.A., Decroos, F.C., Ying, G.-S., Stinnert, S.S., Heydary, C.S., Burns, R., Maguire, M. G., Martin, D., Jaffe, G.J., 2015. Identification of fluid on optical coherence tomography by treating ophthalmologists versus a reading center in the comparison of age-related macular degeneration treatments trials (CATT). *Retina* 35, 1303–1314. <https://doi.org/10.1097/IAE.0000000000000483>.
- Toth, C.A., Tai, V., Pistilli, M., Chi, S., Winter, K.P., Daniel, E., Grunwald, J.E., Jaffe, G.J., Martin, D.F., Ying, G.-S., Farsiu, S., Maguire, M.G., 2019. Distribution of OCT features within areas of macular atrophy or scar after 2 Years of anti-VEGF treatment for neovascular AMD in CATT. *Ophthalmol. Retin.* 3, 316–325. <https://doi.org/10.1016/j.joret.2018.11.011>.
- Treder, M., Lauermann, J.L., Eter, N., 2018. Automated detection of exudative age-related macular degeneration in spectral domain optical coherence tomography using deep learning. *Graefe's Arch. Clin. Exp. Ophthalmol.* 256, 259–265. <https://doi.org/10.1007/s00417-017-3850-3>.
- Trivizki, O., Karp, M.R., Chawla, A., Yamanuha, J., Gregori, G., Rosenfeld, P.J., 2020. Eliminating visual acuity and dilated fundus examinations improves cost efficiency of performing optical coherence tomography-guided intravitreal injections. *Am. J. Ophthalmol.* 219, 222–230. <https://doi.org/10.1016/j.ajo.2020.06.028>.
- Van Der Heijden, A.A., Abramoff, M.D., Verbraak, F., van Hecke, M.V., Liem, A., Nijhuis, G., 2018. Validation of automated screening for referable diabetic retinopathy with the IDx-DR device in the Hoorn Diabetes Care System. *Acta Ophthalmol.* 96, 63–68.
- Venhuizen, F.G., van Ginneken, B., Liefers, B., van Asten, F., Schreur, V., Fauser, S., Hoyng, C., Theelen, T., Sánchez, C.I., 2018. Deep Learning Approach for the Detection and Quantification of Intraretinal Cystoid Fluid in Multivendor Optical Coherence Tomography, vol. 9, p. 1545.

- Venhuizen, F.G., van Ginneken, B., Liefers, B., van Grinsven, M.J.P., Fauser, S., Hoyng, C., Theelen, T., Sánchez, C.I., 2017. Robust total retina thickness segmentation in optical coherence tomography images using convolutional neural networks. <https://doi.org/10.1364/BOE.8.003292>, 8, 3292–3316.
- Verbeke, G., Molenberghs, G., 2009. *Linear Mixed Models for Longitudinal Data*. Springer Science & Business Media, Leuven.
- Vidal, P.L., de Moura, J., Novo, J., Penedo, M.G., Ortega, M., 2018. Intraretinal fluid identification via enhanced maps using optical coherence tomography images. <https://doi.org/10.1364/BOE.9.004730>, 9, 4730–4754.
- Vogl, W.D., Bogunović, H., Waldstein, S.M., Riedl, S., Schmidt-Erfurth, U.M., 2021. Spatio-temporal alterations in retinal and choroidal layers in the progression of age-related macular degeneration (AMD) in optical coherence tomography. *Sci. Rep.* 11 (1), 5743 <https://doi.org/10.1038/s41598-021-85110-y>.
- Vogl, W.-D., Waldstein, S.M., Gerendas, B.S., Schlegl, T., Langs, G., Schmidt-Erfurth, U.M., 2017. Analyzing and predicting visual acuity outcomes of anti-VEGF therapy by a longitudinal mixed effects model of imaging and clinical data. *Invest. Ophthalmol. Vis. Sci.* 58, 4173–4181. <https://doi.org/10.1167/iovs.17-21878>.
- von der Emde, L., Pfau, M., Dysli, C., Thiele, S., Möller, P.T., Lindner, M., Schmid, M., Fleckenstein, M., Holtz, F.G., Schmitz-Valckenberg, S., 2019. Artificial intelligence for morphology-based function prediction in neovascular age-related macular degeneration. *Sci. Rep.* 9, 11132. <https://doi.org/10.1038/s41598-019-47565-y>.
- Vos, T., Allen, C., Arora, M., Barber, R.M., Bhutta, Z.A., Brown, A., Carter, A., Casey, D.C., Charlson, F.J., Chen, A.Z., Coggeshall, M., Cornaby, L., Dandona, L., Dicker, D.J., Dilegge, T., Erskine, H.E., Ferrari, A.J., Fitzmaurice, C., Fleming, T., Forouzanfar, M.H., Fullman, N., Getting, P.W., Goldberg, E.M., Graetz, N., Haagsma, J.A., Hay, S.I., Johnson, C.O., Kassebaum, N.J., Kawashima, T., Kemmer, L., Khalil, I.A., Kinfu, Y., Kyu, H.H., Leung, J., Liang, X., Lim, S.S., Lopez, A.D., Lozano, R., Marcak, L., Mensah, G.A., Mokdad, H.A., Naghavi, M., Nguyen, G., Nsoesie, E., Olsen, H., Pigott, D.M., Pinho, C., Rankin, Z., Reining, N., Salomon, J.A., Sandar, L., Smith, A., Stanaway, J., Steiner, C., Teeple, S., Thomas, B.A., Troeger, C., Wagner, J.A., Wang, H., Wanga, V., Whiteford, H.A., Zoekler, L., Abajobir, A.A., Abate, K.H., Abbafati, C., Abbas, K.M., Abd-Allah, F., Abraham, B., Abubakar, I., Abu-Raddad, L.J., Abu-Rmeileh, N.M.E., Ackerman, I.N., AdEBIYI, A.O., Ademi, Z., Adou, A.K., Afanvi, K.A., Agardh, E.E., Agarwal, A., Kiadaliri, A.A., Ahmadih, H., Ajala, O.N., Akinyemi, R.O., Akseer, N., Al-Aly, Z., Alam, K., Alam, N.K.M., Aldhahri, S.F., Alegretti, M.A., Alemu, Z.A., Alexander, L.T., Alhabib, S., Ali, R., Alkerwi, A., Alla, F., Allebeck, P., Al-Raddadi, R., Alsharif, U., Altirkawi, K.A., Alvis-Guzman, N., Amare, A.T., Amberbir, A., Amini, H., Ammar, W., Amrock, S.M., Andersen, H.H., Anderson, G.M., Anderson, B.O., Antonio, C.A.T., Aregay, A.F., Ärnlöv, J., Artaman, A., Asayesh, H., Assadi, R., Atique, S., Avokpaho, E.F.G.A., Awasthi, A., Quintanilla, B.P.A., Azzopardi, P., Bacha, U., Badawi, A., Balakrishnan, K., Banerjee, A., Barac, A., Barker-Collo, S.L., Bärnighausen, T., Barregard, L., Barrero, L.H., Basu, A., Bazargan-Hejazi, S., Beghi, E., Bell, B., Bell, M.L., Bennett, D.A., Bensenor, I.M., Benzian, H., Berhane, A., Bernabé, E., Betsu, B.D., Beyene, A.S., Bhala, N., Bhatt, S., Biadgilign, S., Bienhoff, K., Bikbov, B., Birukov, S., Bisanzio, D., Bjertness, E., Bløre, J., Borschmann, R., Boufous, S., Brainin, M., Brazinova, A., Breitborde, N.J.K., Brown, J., Buchbinder, R., Buckle, G.C., Butt, Z.A., Calabria, B., Campos-Nonato, I.R., Campuzano, J.C., Carabin, H., Cárdenas, R., Carpenter, D.O., Carrero, J.J., Castañeda-Orjuela, C.A., Rivás, J.C., Catalán-López, F., Chang, J.-C., Chiang, P.-C., Chibueze, C.E., Chisumpa, V.H., Choi, J.-Y.J., Chowdhury, R., Christensen, H., Christopher, D.J., Ciobanu, L.G., Cirillo, M., Coates, M.M., Colquhoun, S.M., Cooper, C., Cortinovis, M., Crump, J.A., Damtew, S.A., Dandona, R., Daoud, F., Dargan, P.I., das Neves, J., Davey, G., Davis, A.C., Leo, D., De, Degenhart, L., Gobbo, L.C., Del, Dellavalle, R.P., Deribe, K., Deribew, A., Derrett, S., Jarlaas, D.C., Des, Dharmaratne, S.D., Dhillon, P.K., Diaz-Torné, C., Ding, E.L., Driscoll, T.R., Duan, L., Dubey, M., Duncan, B.B., Ebrahimi, H., Ellenbogen, R.G., Elyazar, I., Endres, M., Endries, A.Y., Ermakov, S.P., Eshrai, B., Estep, K., Farid, T.A., Farinha, C.S. e S., Faro, A., Farvid, M.S., Farzadfar, F., Feigin, V.L., Felson, D.T., Fereshtehnejad, S.-M., Fernandes, J.G., Fernandes, J.C., Fischer, F., Fitchett, J.R.A., Foreman, K., Fowkes, F.G.R., Fox, J., Franklin, R.C., Friedman, J., Frostad, J., Fürst, T., Futran, N.D., Gabbe, B., Ganguly, P., Gankpé, F.G., Gebre, T., Gebrehiwot, T.T., Gebremedhin, A.T., Geleijnse, J.M., Gessner, B.D., Gibney, K.B., Ginawi, I.A.M., Giref, A.Z., Giroud, M., Gishu, M.D., Giussani, G., Glaser, E., Godwin, W.W., Gomez-Dantes, H., Gona, P., Goodridge, A., Gopalani, S.V., Gotay, C.C., Goto, A., Gouda, H.N., Grainger, R., Greaves, F., Guillemin, F., Guo, Y., Gupta, Rahul, Gupta, Rajeev, Gupta, V., Gutiérrez, R.A., Haile, D., Hailu, A.D., Hailu, G.B., Halasa, Y.A., Hamadeh, R.H., Hamidi, S., Hammami, M., Hancock, J., Handal, A.J., Hankey, G.J., Hao, Y., Harb, H.L., Harikrishnan, S., Haro, J.M., Havmoeller, R., Hay, R.J., Heredia-Pi, I.B., Heydarpour, P., Hoek, H.W., Horino, M., Horita, N., Hosgood, H.D., Hoy, D.G., Htet, A.S., Huang, H., Huang, J.J., Huynh, C., Iannarone, M., Ibarg, K.M., Innos, K., Inoue, M., Iyer, V.J., Jacobsen, K.H., Jahanmehr, N., Jakovljevic, M.B., Javanbakht, M., Jayaraman, S.P., Jayatilleke, A.U., Jee, S.H., Jeemon, P., Jensen, P.N., Jiang, Y., Jibat, T., Jimenez-Corona, A., Jin, Y., Jonas, J.B., Kabir, Z., Kalkonde, Y., Kamal, R., Kan, H., Karch, A., Karem, C.K., Karimkhani, C., Kasaeian, A., Kaul, A., Kawakami, N., Keiyoro, P.N., Kemp, A.H., Keren, A., Kesavachandran, C.N., Khader, Y.S., Khan, A.R., Khan, E.A., Khang, Y.-H., Khera, S., Khoja, T.A.M., Khubchandani, J., Kieling, C., Kim, P., Kim, C., Kim, D., Kim, Y.J., Kissoun, N., Knibbs, L.D., Knudsen, A.K., Kokubo, Y., Kolte, D., Kopec, J.A., Kosen, S., Kotsakis, G.A., Koul, P.A., Koyanagi, A., Kravchenko, M., Defo, B.K., Bicer, B.K., Kudom, A.A., Kuipers, E.J., Kumar, G.A., Kutz, M., Kwan, G.F., Lal, A., Lalloo, R., Lallukka, T., Lam, H., Lam, J.O., Langan, S.M., Larsson, A., Lavados, P.M., Leasher, J.L., Leigh, J., Leung, R., Levi, M., Li, Yichong, Li, Yongmei, Liang, J., Liu, S., Liu, Y., Lloyd, B.K., Lo, W.D., Logrosino, G., Looker, K.J., Lotufo, P.A., Lunevicius, R., Lyons, R.A., Mackay, M.T., Magdy, M., Razek, A., El, Mahdavi, M., Majdan, M., Majeed, A., Malekzadeh, R., Marques, W., Margolis, D.J., Martinez-Raga, J., Masiye, F., Massano, J., McGarvey, S.T., McGrath, J.J., McKee, M., McMahon, B.J., Meaney, P.A., Mehari, A., Mejia-Rodriguez, F., Mekonnen, A.B., Melaku, Y.A., Memiah, P., Memish, Z.A., Mendoza, W., Meretoja, A., Meretoja, T.J., Mhimbira, F.A., Millear, A., Miller, T.R., Mills, E.J., Mirarefin, M., Mitchell, P.B., Mock, C.N., Mohammadi, A., Mohammed, S., Monasta, L., Hernandez, J.C.M., Montico, M., Mooney, M.D., Moradi-Lakeh, M., Morawska, L., Mueller, U.O., Mullany, E., Mumford, J.E., Murdoch, M.E., Nachege, J.B., Nagel, G., Naheed, A., Naldi, L., Nangia, V., Newton, J.N., Ng, M., Ngalesoni, F.N., Nguyen, Q., Le Nisar, M.I., Pete, P.M.N., Nolla, J.M., Norheim, O.F., Norman, R.E., Norrvig, B., Nunes, B.P., Ogbo, F.A., Oh, I.-H., Ohkubo, T., Olivares, P.R., Olusanya, B.O., Olusanya, J.O., Ortiz, A., Osman, M., Ota, E., Pa, M., Park, E.-K., Parsaeian, M., de Azeredo Passos, V.M., Caicedo, A.J.P., Patten, S.B., Patton, G.C., Pereira, D.M., Perez-Padilla, R., Perico, N., Pesudos, K., Petzold, M., Phillips, M.R., Piel, F.B., Pillay, J.D., Pishgar, F., Plass, D., Platts-Mills, J.A., Polinder, S., Pond, C.D., Popova, S., Poulton, R.G., Pourmalek, F., Prabhakaran, D., Prasad, N.M., Qorbani, M., Rabiee, R.H.S., Radfar, A., Rafay, A., Rahimi, K., Rahimi-Movaghhar, V., Rahman, M., Rahman, M.H.U., Rahman, S.U., Rai, R.K., Rajic, S., Ram, U., Rao, P., Refaat, A.H., Reitsma, M.B., Remuzzi, G., Resnikoff, S., Reynolds, A., Ribeiro, A.L., Blancas, M.J.R., Roba, H.S., Rojas-Rueda, D., Ronfan, L., Rosenthal, G., Roth, G.A., Rothenbacher, D., Roy, A., Sagar, R., Sahathevan, R., Sanabria, J.R., Sanchez-Niño, M.D., Santos, I.S., Santos, J.V., Sarmiento-Suarez, R., Sartorius, B., Satpathy, M., Savic, M., Sawhney, M., Schaub, M.P., Schmidt, M.I., Schneider, I.J.C., Schöttker, B., Schwebel, D.C., Scott, J.G., Seedat, S., Sepanlou, S.G., Servan-Mori, E.E., Shackelford, K.A., Shaheen, A., Shaikh, M.A., Sharma, R., Sharma, U., Shen, J., Shepard, D.S., Sheth, K.N., Shibuya, K., Shin, M.-J., Shiri, R., Shiu, I., Shrike, M.G., Sigfusdottir, I.D., Silva, D.A.S., Silveira, D.G.A., Singh, A., Singh, J.A., Singh, O.P., Singh, P.K., Sivonda, A., Skirbekk, V., Skogen, J.C., Sligar, A., Sliwa, K., Soljak, M., Soreide, K., Sorenson, R.J.D., Soriano, J.B., Spodosi, L.A., Sreeramareddy, C.T., Stathopoulou, V., Steel, N., Stein, D.J., Steiner, T.J., Steinke, S., Stover, L., Stroumpoulis, K., Sunguya, B.F., Sur, P., Swaminathan, S., Sykes, B.L., Szoere, C.E.I., Tabarés-Seisdedos, R., Takala, J.S., Tandon, N., Tanne, D., Tavakkoli, M., Taye, B., Taylor, H.R., Ao, B.J., Te, Tedla, B.A., Terkawi, A.S., Thomson, A.J., Thorne-Lyman, A.L., Thrift, A.G., Thurston, G.D., Tobe-Gai, R., Tonelli, M., Topor-Madry, R., Topouzis, F., Tran, B.X., Truelsen, T., Dimbuene, Z.T., Tsilimbaris, M., Tura, A.K., Tuzcu, E.M., Tyrovolas, S., Ukwaja, K.N., Undurraga, E.A., Unke, C.J., Uthman, O.A., van Gool, C.H., Varakin, Y.Y., Vasankari, T., Venketasubramanian, N., Verma, R.K., Violante, F.S., Vladimirov, S.K., Vlassov, V.V., Vollset, S.E., Wagner, G.R., Waller, S.G., Wang, L., Watkins, D.A., Weichenthal, S., Weiderpass, E., Weintraub, R.G., Werdecker, A., Westerman, R., White, R.A., Williams, H.C., Wiysonge, C.S., Wolfe, C.D.A., Won, S., Woodbrook, R., Wubshet, M., Xavier, D., Xu, G., Yadav, A.K., Yan, L.L., Yano, Y., Yaseri, M., Ye, P., Yebyo, H.G., Yip, P., Yonemoto, N., Yoon, S.-J., Younis, M.Z., Yu, C., Zaidi, Z., Zaki, M.E.S., Zeeb, H., Zhou, M., Zodpey, S., Zuhlik, L.J., Murray, C.J.L., 2016. Global, regional, and national incidence, prevalence, and years lived with disability for 310 diseases and injuries, 1990–2015: a systematic analysis for the Global Burden of Disease Study 2015. *Lancet* 388, 1545–1602. [https://doi.org/10.1016/S0140-6736\(16\)31678-6](https://doi.org/10.1016/S0140-6736(16)31678-6).
- Waldstein, S.M., Philip, A.-M., Leitner, R., Simader, C., Langs, G., Gerendas, B.S., Schmidt-Erfurth, U.M., 2016a. Correlation of 3-dimensionally quantified intraretinal and subretinal fluid with visual acuity in neovascular age-related macular degeneration. *JAMA Ophthalmol.* 134, 182. <https://doi.org/10.1001/jamaophthalmol.2015.4948>.
- Waldstein, S.M., Simader, C., Staurenghi, G., Chong, N.V., Mitchell, P., Jaffe, G.J., Lu, C., Katz, T.A., Schmidt-Erfurth, U.M., 2016b. Morphology and visual acuity in afibrelcept and ranibizumab therapy for neovascular age-related macular degeneration in the VIEW trials. *Ophthalmology* 123, 1521–1529. <https://doi.org/10.1016/j.ophtha.2016.03.037>.
- Waldstein, S.M., Wright, J., Warburton, J., Margaron, P., Simader, C., Schmidt-Erfurth, U.M., 2016c. Predictive value of retinal morphology for visual acuity outcomes of different ranibizumab treatment regimens for neovascular AMD. *Ophthalmology* 123, 60–69. <https://doi.org/10.1016/j.ophtha.2015.09.013>.
- Wang, B., Camino, A., Pi, S., Guo, Y., Wang, J., Huang, D., Hwang, T.S., Jia, Y., 2019a. Three-dimensional structural and angiographic evaluation of foveal ischemia in diabetic retinopathy: method and validation. *Biomed. Opt Express* 10, 3522–3532. <https://doi.org/10.1364/bioe.10.003522>.
- Wang, J., Camino, A., Hua, X., Lku, L., Huang, D., Hwang, T.S., Jia, Y., 2019b. Invariant features-based automated registration and montage for wide-field OCT angiography. *Biomed. Opt Express* 10, 120–136. <https://doi.org/10.1364/bioe.10.000120>.
- Wang, J., Hormel, T.T., Gao, L., Zang, P., Guo, Y., Wang, X., Bailey, S.T., Jia, Y., 2020a. Automated diagnosis and segmentation of choroidal neovascularization in OCT angiography using deep learning. *Biomed. Opt Express* 11, 927. <https://doi.org/10.1364/bioe.379977>.
- Wang, J., Hormel, T.T., You, Q., Guo, Y., Wang, X., Chen, L., Hwang, T.S., Jia, Y., 2020b. Robust non-perfusion area detection in three retinal plexuses using convolutional neural network in OCT angiography. *Biomed. Opt Express* 11, 330–345.
- Wang, J., Zhang, M., Hwang, T.S., Bailey, S.T., Huang, D., Wilson, D.J., Jia, Y., 2017. Reflectance-based projection-resolved optical coherence tomography angiography [Invited]. *Biomed. Opt Express* 8, 1536–1548.
- Wang, J., Zhang, M., Pechauer, A.D., Liu, L., Hwang, T.S., Wilson, D.J., Li, D., Jia, Y., 2016. Automated volumetric segmentation of retinal fluid on optical coherence tomography. <https://doi.org/10.1364/BOE.7.001577>, 7, 1577–1589.
- Wang, R.K., Jacques, S.L., Ma, Z., Hurst, S., Hanson, S.R., Gruber, A., 2007. Three dimensional optical angiography. *Opt Express* 15, 4083–4097. <https://doi.org/10.1364/OE.15.004083>.
- Wei, X., Camino, A., Pi, S., Cepurna, W., Huang, D., Morrison, J.C., Jia, Y., 2018. Fast and robust standard-deviation-based method for bulk motion compensation in phase-based functional OCT. *Opt. Lett.* 43, 2204–2207. <https://doi.org/10.1364/OL.43.002204>.

- Wells, J.A., Glassman, A.R., Ayala, A.R., Jampol, L.M., Aiello, L.P., Antoszyk, A.N., Arnold-Bush, B., Baker, C.W., Bressler, N.M., Browning, D.J., Elman, M.J., Ferris, F.L., Friedman, S.M., Melia, M., Pieramici, D.J., Sun, J.K., Beck, R.W., 2015. Afibercept, bevacizumab, or ranibizumab for diabetic macular edema. *N. Engl. J. Med.* 372, 1193–1203. <https://doi.org/10.1056/NEJMoa1414264>.
- Willoughby, A.S., Ying, G.-S., Toth, C.A., Maguire, M.G., Burns, R.E., Grunwald, J.E., Daniel, E., Jaffe, G.J., 2015. Subretinal hyperreflective material in the comparison of age-related macular degeneration treatments trials. *Ophthalmology* 122, 1846–1853. [https://doi.org/10.1016/j.ophtha.2015.05.042 e5](https://doi.org/10.1016/j.ophtha.2015.05.042).
- Wimmers, S., Karl, M.O., Strauss, O., 2007. Ion channels in the RPE. *Prog. Retin. Eye Res.* 26 (3), 263–301. <https://doi.org/10.1016/j.preteyeres.2006.12.002>.
- World Health Organization, 2016. *Global Report on Diabetes*.
- Wykoff, C.C., Croft, D.E., Brown, D.M., Wang, R., Payne, J.F., Clark, L., Abdelfattah, N.S., Sadda, S.R., 2015. Prospective trial of treat-and-extend versus monthly dosing for neovascular age-related macular degeneration: TREX-AMD 1-year results. *Ophthalmology* 122, 2514–2522. <https://doi.org/10.1016/j.ophtha.2015.08.009>.
- Xu, D., Dávila, J.P., Rahimi, M., Rebhun, C.B., Alibhai, A.Y., Waheed, N.K., Sarraf, D., 2018. Long-term progression of type 1 neovascularization in age-related macular degeneration using optical coherence tomography angiography. *Am. J. Ophthalmol.* 187, 10–20. <https://doi.org/10.1016/j.ajo.2017.12.005>.
- Xu, X., Lee, K., Zhang, L., Sonka, M., Abramoff, M.D., 2015. Stratified Sampling Voxel Classification for Segmentation of Intraretinal and Subretinal Fluid in Longitudinal Clinical {OCT} Data, vol. 34, pp. 1616–1623.
- Yanagihara, R.T., Lee, C.S., Ting, D.S.W., Lee, A.Y., 2020. Methodological challenges of deep learning in optical coherence tomography for retinal diseases: a review. *Transl. Vis. Sci. Technol.* 9, 11. <https://doi.org/10.1167/tvst.9.2.11>.
- Yang, J., Zhang, Q., Motulsky, E.H., Thulliez, M., Shi, Y., Lyu, C., de Sisternes, L., Durbin, M.K., Feuer, W., Wang, R.K., Gregori, G., Rosenfeld, P.J., 2019. Two-year risk of exudation in eyes with nonexudative age-related macular degeneration and subclinical neovascularization detected with swept source optical coherence tomography angiography. *Am. J. Ophthalmol.* 208, 1–11. <https://doi.org/10.1016/j.ajo.2019.06.017>.
- Yim, J., Chopra, R., Spitz, T., Winkens, J., Obika, A., Kelly, C., Askham, H., Lukic, M., Huemer, J., Fasler, K., Moraes, G., Meyer, C., Wilson, M., Dixon, J., Hughes, C., Rees, G., Khaw, P.T., Karthikesalingam, A., King, D., Hassabis, D., Suleyman, M., Back, T., Ledsam, J.R., Keane, P.A., De Fauw, J., 2020. Predicting conversion to wet age-related macular degeneration using deep learning. *Nat. Med.* 26, 892–899. <https://doi.org/10.1038/s41591-020-0867-7>.
- Yiu, G., Welch, R.J., Wang, Y., Wang, Z., Wang, P.-W., Haskova, Z., 2020. Spectral-domain OCT predictors of visual outcomes after ranibizumab treatment for macular edema resulting from retinal vein occlusion. *Ophthalmol. Retin.* 4, 67–76. <https://doi.org/10.1016/j.joret.2019.08.009>.
- You, Q.S., Wang, J., Guo, Y., Pi, S., Flaxel, C.J., Bailey, S.T., Huang, D., Jia, Y., Hwang, T.S., 2020. Optical coherence tomography angiography avascular area association with 1-year treatment requirement and disease progression in diabetic retinopathy. *Am. J. Ophthalmol.* 217, 268–277. <https://doi.org/10.1016/j.ajo.2020.04.024>.
- Zang, P., Liu, G., Zhang, M., Dongye, C., Wang, J., Pechauer, A.D., Hwang, T.S., Wilson, D.J., Huang, D., Li, D., Jia, Y., 2016. Automated motion correction using parallel-strip registration for wide-field en face OCT angiogram. *Biomed. Opt. Express* 7, 2823–2836. <https://doi.org/10.1364/BOE.7.002823>.
- Zhang, A., Zhang, Q., Wang, R.K., 2015. Minimizing projection artifacts for accurate presentation of choroidal neovascularization in OCT micro-angiography. *Biomed. Opt Express* 6, 4130–4143. <https://doi.org/10.1364/BOE.6.004130>.
- Zhang, M., Hwang, T.S., Campbell, J.P., Bailey, S.T., Wilson, D.J., Huang, D., Jia, Y., 2016. Projection-resolved optical coherence tomographic angiography. *Biomed. Opt Express* 7, 816–828. <https://doi.org/10.1364/BOE.7.000816>.
- Zhu, J.-Y., Park, T., Isola, P., Efros, A.A., 2017. Unpaired Image-To-Image Translation Using Cycle-Consistent Adversarial Networks arXiv.